MSc Program "Building Science & Technology"

Calibrated Sky Luminance Maps for Daylight Simulation

A master's thesis submitted for the degree of
“Master of Science”

Supervisor: Univ. Prof. Dr. Ardeshir Mahdavi
Department of Building Physics and Building Ecology

Tsiopoulou Chamaidi

Vienna – June 2006

student id nr.: 0426892

Affidavit

I, **Chamaidi Tsiopoulou**, hereby declare

1. That I am the sole author of the present Master Thesis, "Calibrated Sky Luminance Maps for Daylight Simulation ", 110 pages, bound, and that I have not used any source or tool other than those referenced or any other illicit aid or tool, and
2. That I have not prior to this date submitted this Master Thesis as an examination paper in any form in Austria or abroad.

Vienna, 27.06.06

Date Signature

Table of Contents

List of Figures

List of Tables

Acknowledgement

This master thesis has been carried out in the framework of the master course "Building Science and Technology". It is a subject I have worked on during the last semester and its completion has been a great challenge for me.

First of all, I would like to thank my supervisor Univ. Prof. Dr. A. Mahdavi for his guidance and support during the period of my work. Of course, it was important that the department provided the necessary equipment for the execution of the measurements and the acquisition of all the data.

Last but not least, I would like to thank Bojana Spasojevic for her help. This master thesis has been based on a part of her PhD and a similar procedure has been followed. So her advices have been very valuable for every step of the work.

Abstract

Building design and control applications can benefit from daylight simulation. Sky models help to model the sky conditions and predict the availability of daylight in indoor environments. Sky luminance is changing according to the weather, the season of the year and the time of the day, therefore it is difficult to create an accurate sky model. The simplified models that are currently used for computational simulation do not take into account these constant changes.

It is important to test if there is the possibility of creating a sky model that approaches the characteristics of real sky and provides the architects with more precise daylight predictions. As past research has demonstrated, relatively low-cost sky luminance mapping via digital imaging can provide an alternative to highly sophisticated sky scanners and support the provision of information on sky luminance distribution patterns on a more pervasive basis.

The aim of this research is first to explore the potential of deriving sky luminance distribution maps based on digital imaging and then to test their efficiency for the prediction of indoor daylight. A comparison is made between the predictions based on existing sky models (CIE Standard Skies and Perez All-weather sky) and the camera-based sky model. Thus, the effects of the selection of the sky model on indoor daylighting prediction are explored.

A set of measurements were performed at the roof of the TU Vienna in order to obtain the necessary data. The horizontal illuminance levels due to 12 sky sectors were measured with the help of a sky monitoring device.

A scale (1:5) model of an architectural space was used to measure the indoor illuminance values with the help of three sensors. At the same time, images of the sky were obtained with the help of a digital camera with a fish-eye converter.

Luminance values were derived from the images and four calibration methods were used to generate accurate sky luminance distribution maps. These variously calibrated luminance values were then compared with the corresponding photometric measurements. Finally, the application of a digitally derived sky model based on the best calibration method was compared with the other two sky models toward the prediction of indoor illuminance levels using the case of the scale model. The results demonstrated that the camera-based sky model was more reliable than the other two sky models.

It was concluded that digital imaging combined with parallel photometric calibration can provide a valuable means for a real-time generation of sky luminance maps. Detailed sky luminance models can be generated and their application can increase the predictive accuracy of the computational daylight prediction tools. Moreover, the reliability of daylight simulation can be increased toward supporting the design process and the operation of daylighting systems in buildings.

Keywords: daylight simulation; sky luminance mapping; digital imaging; sky models.

1 Introduction

1.1 Motivation

Natural light has always played a dominant role in human life. It is important for health and comfort. Also, the way in which daylight is provided in the buildings determines - in most cases at least - the quality of the indoor environment as well as the necessary auxiliary energy consumption for the building environmental control systems. So, the availability and quality of daylight of the interior in buildings is among the primary concerns of architects. Daylight simulation applications can contribute to the improvement of the architectural design as long as they can help in the prediction of daylight distribution in spaces.

In order to accomplish energy simulations correctly, it is necessary to know daylight conditions during the whole year. Currently, most of the applications work with simplified sky luminance models. CIE Standard Clear Sky and Overcast Sky show the two extreme sky conditions. Most of the real skies though lie between the two CIE Standard Skies (Igawa et al. 1999). As a result, the actual state of daylight availability is not represented accurately. The models used are not sensitive to every change of luminance in different areas of the sky (Spasojevic and Mahdavi 2005).

Since the characteristics of real skies are not represented accurately by standard skies, many attempts have been made towards the monitoring of the sky to get data about the sky luminance distribution. Nowadays, highly sophisticated sky scanners can be used to acquire these data and capture the real image of the sky. But these are quite expensive. So a low cost method for sky luminance mapping is necessary.

The goal of this research is to create a sky model by deriving sky luminance distribution maps from digital images and test its potential to be used for indoor daylight simulation. The objective is to demonstrate that this method gives the possibility to create detailed and accurate sky distribution models. In order to achieve this, other sky models are used to repeat the simulations for daylight predictions. The models chosen are the CIE Standard Skies (Sky types 2006) and the Perez All-weather sky model (Perez et al. 1993), which is considered the more reliable at the moment. The values obtained are compared to the results with the use of the model based on digital imaging.

This approach can be used for better and more reliable indoor daylight simulations. The sky luminance distribution maps derived from images can describe the sky conditions as past research has demonstrated (Roy et al. 1998). The collection and process of such images over a representative period of time can assist the creation of permanent records for various locations. Architects can use this data for design support purposes.

Daylight is also very important in terms of visual comfort. It provides a more pleasant atmosphere inside a building and is a superior quality of light to artificial lighting. It is often necessary for specialized tasks such as colour matching. So sky luminance data can be used for better visualizations of spaces too.

In addition, this method can effectively apply to the building operation phase. Recently, building control systems have become more sophisticated and the idea of sentient buildings is a wide field of research (Mahdavi 2005). A self-actualizing model is necessary for the operation of those buildings. Sky luminance mapping can supply with the essential information about the real-time sky conditions. These data can then be used for the operation of lighting systems in architectural spaces or the control of indoor climates.

Most buildings use natural daylight in some way, though some more than others. The levels of available light from the sky and how it varies throughout the day and year can be a key element in meeting several concerns. Some of those concerns are: adequate lighting levels to allow the required activities to take place, control of temperature and glare, the costs associated with modifying the indoor climate to meet required standards and the energy consumption in achieving these standards.

With the availability of high resolution digital cameras it is possible nowadays to capture information about the sky. This opportunity opens up a range of ways of analyzing and documenting sky conditions.

1.2 Background

1.2.1 Sky models

One of the most desirable sources of light is daylight. Architects have to place a high priority on daylight design. The difficulty though is that accurate sky conditions are required. A lot of research has been done in order to create a sky model that can be used for indoor daylight simulation.

Moon and Spencer (1942) surveyed and arranged the previous research works and proposed luminance distribution of the overcast sky as the standard (Igawa et al. 1999). This model has been recommended as the CIE Standard Overcast Sky after some simplifications (1955). It resembles a considerably dark sky covered with thick clouds and it is the first CIE standard sky with non-uniform luminance distribution.

The luminance distribution on the clear sky was derived by Kittler (1967). This clear sky model has been adapted as the CIE Standard Clear Sky in 1973 (Darula and Kittler 2002). The Clear Sky is a sunny sky with non-uniform luminance distribution with variance over both, altitude and azimuth. It is brighter around the sun and dimmer opposite it.

Both CIE Standard Skies describe the two extreme sky conditions; the completely cloudy sky on one hand and the clear sky with no coverage on the other. The frequency in which those two situations occur is very small. The real skies usually lie in between. This is the reason why there was still the need for a better sky model for the representation of the real skies.

Nakamura (1985) proposed the Intermediate Sky. This is a kind of the average sky models of each solar altitude of all the skies except for the ones similar to the two CIE Standard Skies (Igawa et al. 1999).

Apart from the CIE Standard Skies several other sky models have been proposed:

a. ASRC-CIE model: This is a linear combination of four skies –the CIE Clear Sky, the Gusev turbid clear sky, the intermediate sky and the CIE Overcast Sky. At any occasion, two of the skies are selected depending on the prevailing value of sky clearness. These skies are then combined according to sky clearness and the sky brightness (Littlefair 1994).

b. Brunger's model: this model describes the sky luminance distribution by parameterising insolation conditions as functions of the ratio of global to extraterrestrial irradiance (Lam et al. 1997).
c. Kittler's model: the Kittler Homogeneous Sky requires an assessment of the illuminance turbidity coefficient which can be derived from direct illuminance data. It simulates the diffusion characteristics of a real sky by an equivalent homogeneous sky (Roy et al. 1995).
d. Perraudeau's model: this model uses a single basic equation for sky luminance but with adjustable coefficients. In practice this luminance model consists of a choice between five sky luminance distributions –overcast, intermediate overcast, intermediate mean, intermediate blue and blue. The cloud ratio determines which sky is chosen each time (Littlefair 1994).
e. All-weather sky model: the model was developed by Perez based on a large, high-quality experimental set of sky-scan data. It combines a simple framework that can assume most prevailing sky luminance patterns with a set of coefficients. These coefficients are treated as a function of sky clearness and brightness and solar elevation (Perez et al. 1993).

The above models (with the exception of the CIE Standard Overcast Sky) base their computation for sky luminance distribution on the basic parameters of solar altitude, solar azimuth, diffuse horizontal irradiance, global or direct normal irradiance and extraterrestrial solar irradiance. Kittler's model needs the ground reflectance as well (Lam et al. 1997).

1.2.2 Sky modeling from digital images

Commonly, the CIE standard models - overcast, intermediate or clear - are used for simulation of daylighting performance. Data analysis of measurements recorded at the Research class measurement station located at the Sydney International Airport, Mascot, and other data from the International Daylight Measurement Program (IDMP) showed that CIE models do not provide accurate indications of the sky conditions in some countries. Nor do combinations of the standard models provide a realistic estimate of the intermediate sky conditions (Ruck et al. 1993).

Skies change continuously and this makes their analysis and representation a challenging problem. The study and measurement of sky properties has been the subject of on-going research for some time. One of the most developed works for terrestrial based imagery has been done in the marine Physical Laboratory at the University of California (Shields 1998). This group has developed the Whole Sky Imager (WSI). It is a complete package consisting of a camera, a computer and related software that can record sky images. The instrument yields cloud fraction and the distribution of clouds over the sky dome, as well as the associated distribution of the radiance. This WSI is designed to operate both in daylight and night-time conditions.

Figure 1 Day/night whole sky imager fielded at site

(Shields 1998)

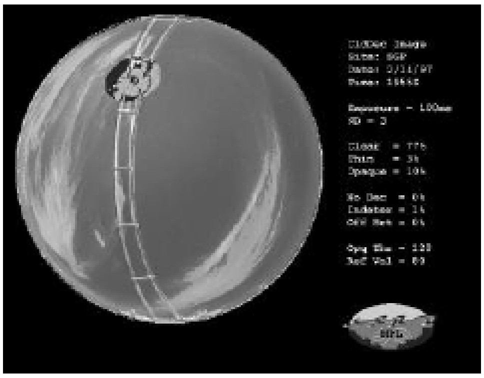

Figure 2 Grey rendition of cloud decision image for a sky with thin clouds
(Shields 1998)

Davis et al. have developed a study to investigate the feasibility of using computer vision to measure one of the weather elements, the cloud amount (Davis et al. 1992). Color-slide images were digitized and viewed through red, green and blue filters and transformed to hue, saturation and value. Various diagnostic parameters were derived and were successfully applied to a number of images, with the usual problems of dealing with colour distortions inherent to film processing. This study was mostly aiming to help the needs of the meteorological community. But still it is a survey in the area of cloud edge extraction from coloured photographs.

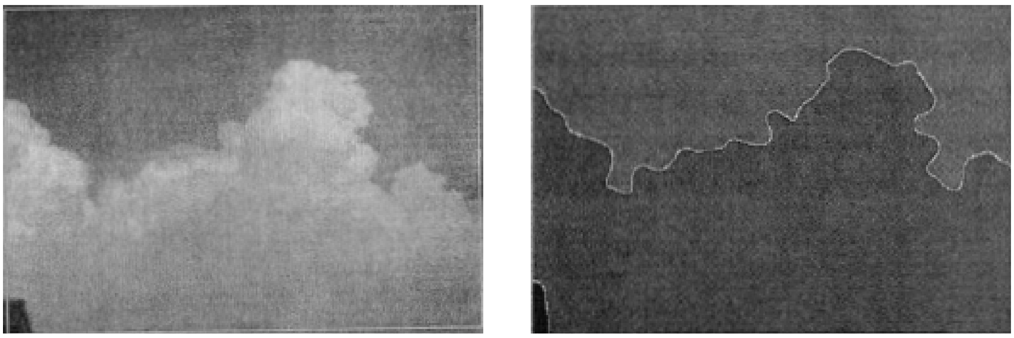

Figure 3 Part of a digitized image on the left and the same part after execution of algorithms developed
(Davis et al. 1992)

An ARC Project carried out in Australia had as an objective to evaluate and demonstrate the viability of using digital images of the sky to extract luminance information (Roy et al. 1998). Images were taken with a standard CCD camera. The camera was calibrated to give quite respectable results for the determination of sky luminance levels. The images of the sky dome were segmented into sky and cloud components. The techniques used for this are based on empirical methods using colour information in an intuitive way and on the use of neural networks to classify the image using a set of sample points which have been pre-classified. Also, the group developed a method for cleaning up the resulting image using a convolution mask to remove odd miss-classified pixels. So the process becomes more reliable. After those steps, the cloud edges can be represented by polylines, suitably smoothed to give a level of accuracy. From this model a Standard Digital Form model can be constructed. This gives information about the luminance distribution and the cloud coverage. The whole process of an image can be completed in less than two minutes and it can be stored for later usage.

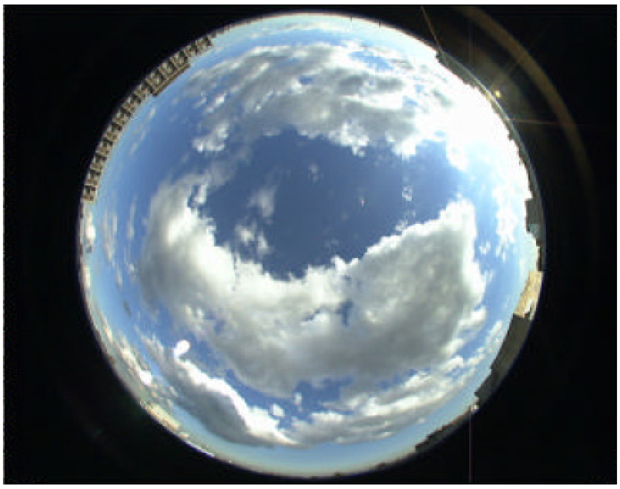

Figure 4 A typical digital image
(Roy et al. 1998)

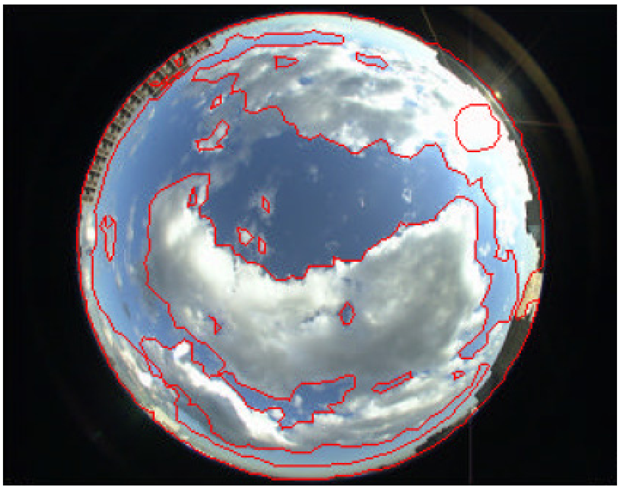

Figure 5 The original image with the cloud edges plotted
(Roy et al. 1998)

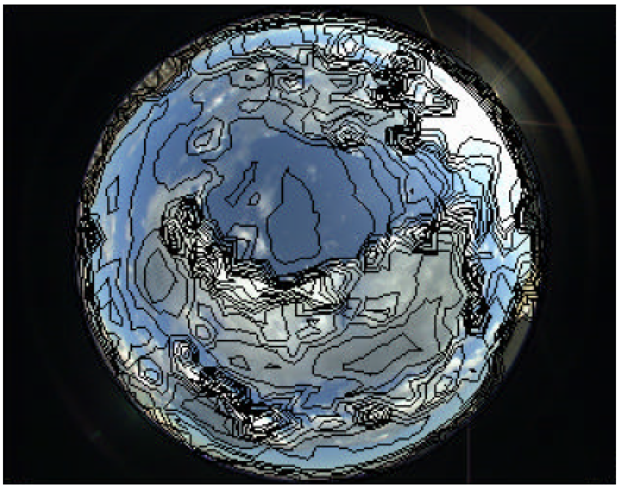

Figure 6 The SDF model with the contours plotted
(Roy et al. 1998)

B. Spasojevic and A. Mahdavi (Vienna University of Technology) carried out a research to explore the potential of using a digital camera with a fish-eye converter toward real-time derivation of sky luminance distribution maps (Spasojevic and Mahdavi 2005). The sky luminance data derived from the digital images were compared to the corresponding photometric measurements from a sky monitoring device. The images were segmented into 256 patches in order to get as accurate sky luminance data as possible. To calibrate the process, a correction factor was applied to the digitally gained luminance values. The comparison of the corrected camera-based values and the photometric measurements showed that such corrected digital images can be used for daylight simulation packages. To illustrate the potential of this approach toward improved indoor light level simulation, a comparison was done between two sets of lighting simulations predicting indoor illuminance levels in a test space under overcast sky conditions. The first set of simulations was conducted using the CIE Standard Overcast Sky and the second using the digital images. The results demonstrated that the values taken with the use of digital images were more reliable.

This master thesis has as a subject a research that is based on the methodology followed in this past survey. The same instruments are used for the acquisition of the necessary sets of data.

2 Approach

This research has as an objective first the derivation of sky luminance maps and the generation of a sky model based on digital images and then the test of its efficiency when it is used for indoor daylight predictions. To achieve this, the results from two commonly used sky models are compared to those of the camera-based model. The research design is structured in such a way that there are four steps followed:

a. Measurements
b. Digital imaging
c. Calibration of camera-based luminance values
d. Indoor illuminance prediction

The first three steps lead to the derivation of sky luminance distribution maps from digital images. During the forth step the comparison of indoor values for daylight calculated by RADIANCE is done.

2.1 Measurements

Two sets of measurements were obtained to examine the reliability of camera-driven sky luminance maps: photometrically measured values from a sky monitoring device and photometrically measured values from a model of an architectural space.

2.1.1 Sky monitoring device

A sky monitoring device was used to measure the horizontal illuminance. This device was an attempt for a low-cost sky scanner that can give reliable measurements. The concept was to divide the sky dome in equal sectors and use sensors to measure the horizontal illuminance reaching from each one of them.

The device consisted of a box that was subdivided into 12 black-colored cells arranged in three levels. All the cells had the same dimensions and at the center of their basis there was an illuminance sensor. In each cell a quadratic aperture was positioned in such a way so that each one of them was facing one part of the sky dome. In that way the sensors were measuring the horizontal illuminance that was reaching them through the aperture. Due to the arrangement of the cells and the apertures, each sensor was exposed to the light coming from one of the equally-sized sky hemisphere sectors. So each sensor was getting light from a solid angle equal to π/6.

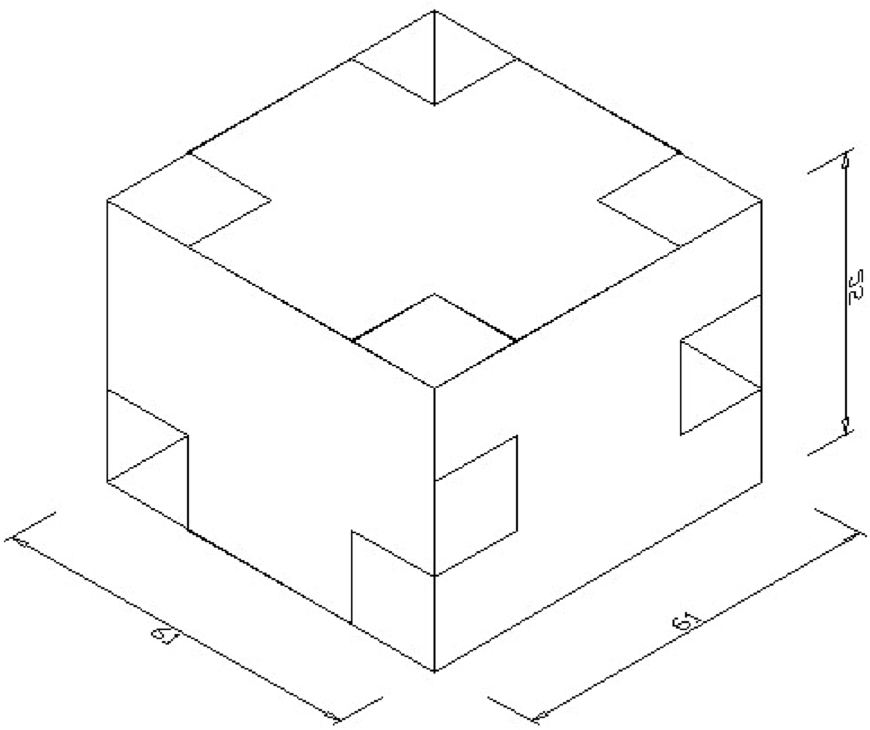

Figure 7 Monitoring device for measuring the illuminance due to 12 sky hemisphere sectors

This sky monitoring device was placed on the roof of a building of the Vienna University of Technology, Vienna, Austria. It was properly oriented so that every cell was facing to the proper part of the sky dome. The measurements were acquired with the help of a program developed in LabVIEW environment and were stored every second.

LabVIEW (short for Laboratory Virtual Instrumentation Engineering Workbench) is a platform and development environment for a visual programming language from National Instruments. It is used for data acquisition, instrument control and industrial automation on a variety of platforms (LabView 2006).

2.1.2 Model of a room

After the generation of the sky model based on the camera-based luminance measurements, there is the need to use it for indoor daylight prediction and compare it to standard values in order to test its efficiency. For this reason, a model of a real room was used. Sensors were placed in it to measure illuminance levels.

The model was a white box. It was a scale model of an architectural space of dimensions 3m×5m×2.85m. The scale was 1:5. The actual dimensions of the model were 0.6m×1m×0.6m. The bottom of the model was double-layered. The distance between the two layers was 3cm where the sensors were placed. The model also had an opening-window. Its height was 0.3m (real dimension: 1.5m) and started at the height of 0.17m (real dimension: 0.85m) while it covered the whole width of the narrow side of the room. Three sensors were used to measure the horizontal illuminance reaching them from the opening. They were placed on an axis parallel to the long side of the room in such a way that they divided it in four equal parts. On the top part of the model a fourth sensor was located to measure the global horizontal illuminance.

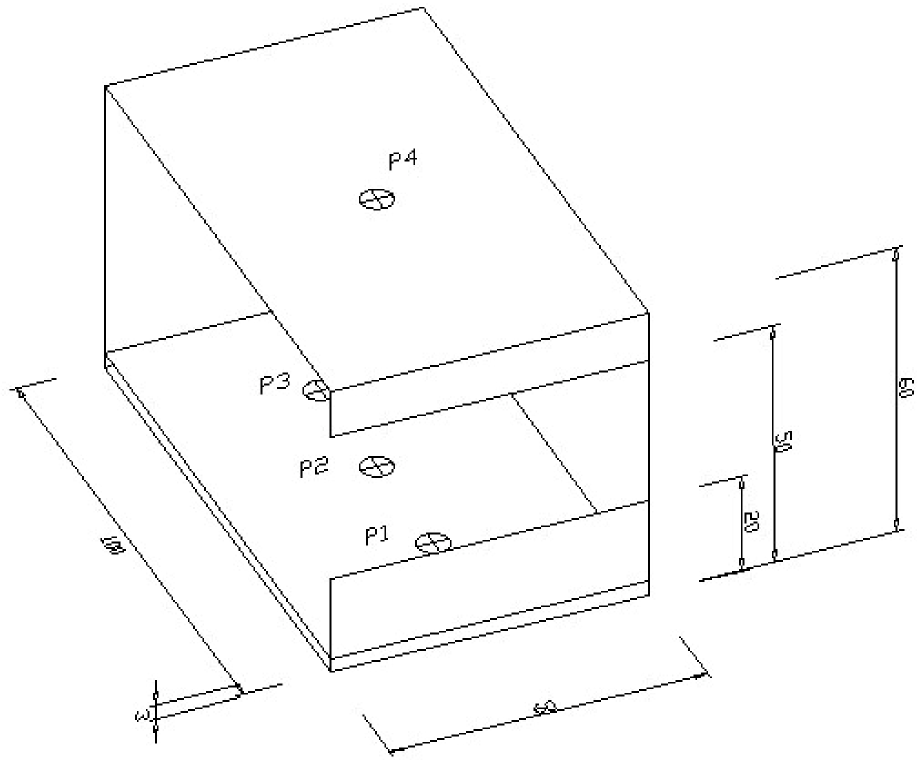

Figure 8 Model of an architectural space and positions of the four sensors

The model was placed on the same roof as the sky monitoring device. It was placed parallel to the walls of the building. So it leaned 21.9^{o} from the axis north-south towards the east. Some days the model was placed with the opening facing towards the north and some facing towards the south. The sensors were connected to a computer and values were stored every 15 seconds. The starting point of the process was synchronized with the acquisition of the images so that every second value was corresponding to the same moment of the capture of a photograph.

2.1.3 Calibration of photometrically measured values

The data were collected during a period of 10 days in November 2005. After the acquisition of the two sets of data, a proper organization of them had to be done. The values were arranged with minute interval. The mean value of 61 values from the sky monitoring device was used (30 seconds before and 30 seconds after the desired moment and the one exactly at this moment) and the mean value of 3 values from the sensors of the model (the one exactly at the desired moment, one before and one after). This was done for better approximation of the real change of the illuminance values within the minute intervals.

The sum of the twelve values taken from the sky monitoring device gives the global horizontal illuminance. This should be the same as the value acquired from the sensor on the top of the model. But the sensors used at the scale model are more accurate and reliable than the ones placed in the sky monitoring device. In addition, those have as a limitation from their manufacturer that they are not accurate when they are measuring more than 20,000 Lux. So there was a need to calibrate these photometrically measured values.

The global horizontal illuminance measured from the sensor on the top of the scale model was considered as the correct one and the 12 values from the sky monitoring device corresponding to the same moment were calibrated according to this. There were two cases of correction of the values: uniform and non-uniform. The condition used was if there was a sensor measuring more than 20,000 Lux. If there was not, uniform correction was followed (case 1). In the contrary situation, a non-uniform correction was made that was completed in two steps (case 2). One part of the energy difference was distributed uniformly to all the values with the use of the average of the correction factors of case 1. The second step is the addition of the rest of the energy difference to the maximum value.

After this correction, the photometrically measured values were ready to be used later on for the comparison to the camera-based values.

2.2 Digital imaging

2.2.1 Collection of the digital images

A digital camera equipped with a fisheye converter was used for the acquisition of the digital images. A fisheye lens is a wide-angle lens that takes in an extremely wide, hemispherical image. Originally such lenses were developed for use in astronomy and are called "whole-sky lenses". So this lens gives us the possibility to capture sky images covering a 180^o angle (Fisheye 2006).

Figure 9 Example of a digital image

The camera, mounted on its back and pointing toward the sky zenith, was placed on the top of the tower of the same building. It was oriented in such a way that the top part of the images is pointing to the north. In the images that have been taken from this point, almost the whole sky dome is unobstructed. The images were taken every 30 seconds and were stored in JPG format.

The amount of the images shot was huge. These were taken under a great variety of sky conditions ranging from overcast to clear sky with sun. Also, they were images taken at different hours during the day from early in the morning to the afternoon. A total of 2,344 images were used with a minute interval. So after the period of acquisition of measurements and images, for every minute the corresponding data were as illustrated in Table 1.

Table 1 Summary of data obtained per minute

Source of data	**Data per minute**
Sky monitoring device	12 illuminance levels due to 12 sky sectors
Model	3 indoor illuminance values 1 global horizontal illuminance
Fish-eye camera	1 image

2.2.2 Extraction of luminance values from images

A digital image is usually a rectangular grid of individual pixels. Each pixel is defined by numerical components that give information about which colour the pixel will display. The combined effect of all the individually coloured pixels creates the image (Digital Imaging 2006). Three components are generally sufficient for image encoding. Also a fourth colour can be used. This is black which can be used as an applied colour - as in printing - or by default in imaging technology as it represents the "off" state of the pixel. Because of the need to develop efficient digital imaging systems with pixels able to detect any of thousands of colours, most imaging technology relies on a simple definition system such as directly using the red, green and blue (RGB) output of the imaging device (Roy et al. 1998). So the RGB values of the pixels in every picture contain all the information that can be extracted and used for the derivation of sky luminance distribution maps.

However, the full range of possible colours and luminances can be specified using a system such as the CIE XYZ color space. CIE created in 1931 a chromaticity diagram (Figure 10) that is based on experimental results and describes the entire range of human colour perception (Chromaticity Diagrams 2006).

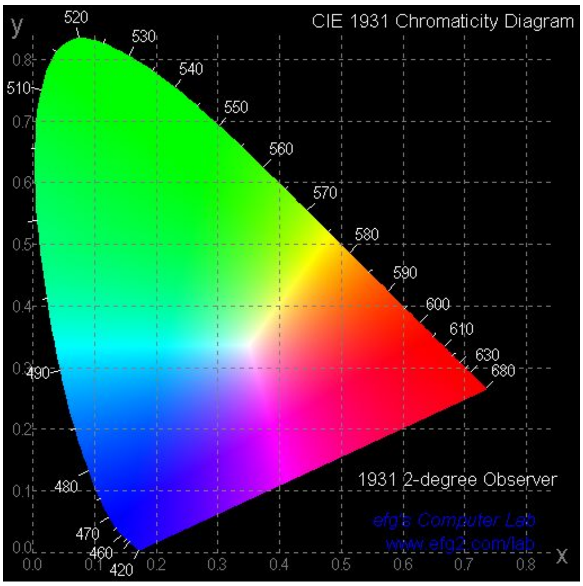

Figure 10 CIE Chromaticity Diagram with typical RGB mixing boundary
(Chromaticity Diagrams 2006)

According to this diagram, each colour is a mixture of three ideal primary colours, each with fixed chromaticity, but with adjustable brightness. The CIE XYZ color space was deliberately designed so that the Y parameter is a measure of the brightness of a color. So if the RGB values are converted into the CIE XYZ ones, the luminance values are obtained (CIE colorspace 2006).

One limitation is that any definition system, as most cameras, that uses real primaries cannot cover the full range of colours. However, the derivation of sky luminance distribution maps requires colour discrimination that is mostly between the range of blue and white or yellow and white which are located close to the centre of the CIE color space, therefore well within a typical RGB system (Figure 10).

Apart from the images themselves and the information that the colour can give, some of the camera's characteristics can also influence the derivation of sky luminance distribution map. They are characteristics that can affect the quality of the image. These are:

- The shutter speed. Shutter speed is the amount of time the shutter remains open during the capture of the image to allow light to reach the imaging sensor. It is measured in seconds or fractions of seconds (Digital Cameras 2006).
- The f-stop number. The f-number expresses the diameter of aperture, which is the part of the camera that controls the amount of light that reaches the imaging sensor and acts like the pupil of an eye. A lower f-stop number opens the aperture and admits more light. Higher f-stop numbers make the camera's aperture smaller (Digital Cameras 2006).

- The ISO number. ISO is the number indicating a digital camera's sensors sensitivity to light. The higher the sensitivity, the less light is needed to make an exposure (Digital Cameras 2006).

Based on the importance of all those characteristics, a Java metadata extractor facilitated the extraction of RGB values out of a JPG image as well as camera values like shutter speed, f-stop number and ISO number. These extracted metadata were then used to derive luminance levels of a particular sky patch (Roy et al. 1998).

Using one color system, the luminance of the sky dome cannot be directly measured, but it is derived from a weighted sum of components. As forementioned, having extracted the RGB values, they were converted into CIE XYZ color space values and the luminance related function V was obtained. The weightings to produce this function from displays conforming to the international standard for linear RGB are (Roy et al. 1998):

$$V = 0.2125 \cdot R + 0.7154 \cdot G + 0.0721 \cdot B \qquad \text{Eq.1}$$

where:
R, G, B RGB values for each pixel [0-255]

A standard function combining ISO, shutter speed and aperture was used to calculate exposure value (Roy et al. 1998):

$$E_v = \frac{179}{200} \pi \cdot S \cdot \frac{T}{f^2} \qquad \text{Eq.2}$$

where:

E_v	exposure value L
S	ISO number
T	shutter speed [s]
f	f-stop number

A user defined curve fitting program, MacCurveFit, was used to evaluate the calibrated luminance function L using the relative image luminance function, V, and the exposure settings for the image, E_v (Roy et al. 1998):

$$L = 344.6 \cdot 10^{-6} \cdot V^{2.4} \cdot E_v^{-1} \qquad \text{Eq.3}$$

where:

L	luminance of the sky patch [cd m^{-2}]
V	luminance related function
E_v	exposure value L

The algorithm consisting of the equations 1 to 3 was used to derive the luminance of particular sky portions from the extracted RGB values for each pixel and camera metadata values. The contribution of the luminance of each portion of the sky hemisphere (Figure 11) to the horizontal illuminance on a point in the center of the hemisphere depends on the altitude of a sky patch and differential solid angle subtended by that sky patch (Spasojevic and Mahdavi 2005):

$$E_i = L_i \cdot \sin\theta_i \cdot \Delta\Omega_i \qquad \text{Eq.4}$$

where:

E_i illuminance on a horizontal plane due to a particular sky patch

L_i luminance of a sky patch

θ_i altitude of the sky patch center

$\Delta\Omega_i$ differential solid angle of a sky patch

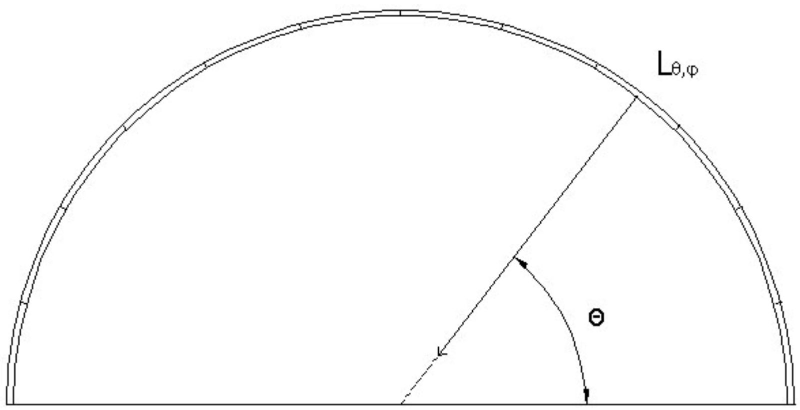

Figure 11 Sky patch luminance contribution to the global horizontal illuminance

The differential solid angle can be expressed in terms of angular size of the sky patch in altitudinal and azimuth direction (Spasojevic and Mahdavi 2005):

$$\Delta\Omega_i = \cos\theta_i \cdot \Delta\phi_i \cdot \Delta\theta_i \qquad \text{Eq.5}$$

where:

$\Delta\Omega_i$ differential solid angle of a sky patch

θ_i altitude of the sky patch center

$\Delta\varphi_i$ angular size of a patch in azimuth direction

$\Delta\theta_i$ angular size of a patch in altitudinal direction

The combination of the equations 4 and 5 leads to the following formula:

$$E_i = L_i \cdot \sin\theta_i \cdot \cos\theta_\iota \cdot \Delta\theta_\iota \cdot \Delta\phi_\iota \qquad \text{Eq.6}$$

The total horizontal illuminance on a point in the center of the hemisphere consisting of the patches with the known luminances can be calculated as follows (Spasojevic and Mahdavi 2005):

$$E = \int_0^{2\pi} \int_0^{\frac{\pi}{2}} L_{\theta,\phi} \cdot \sin\theta \cdot \cos\theta \cdot d\phi \cdot d\theta \qquad \text{Eq.7}$$

In order to be able to compare directly the extracted luminance values from the images to the photometrically measured illuminances, the 12 equally-sized sectors (Figure 12) could be used as sky patches for these equations. For this reason, these 12 sectors should be mapped on the JPG images. However the fisheye images are distorted because of the equidistant transformation within the fisheye lens. Using the basic principle of distortion (Appendix A), the twelve sectors of the sky hemisphere are finally mapped on the images as shown in Figure 13.

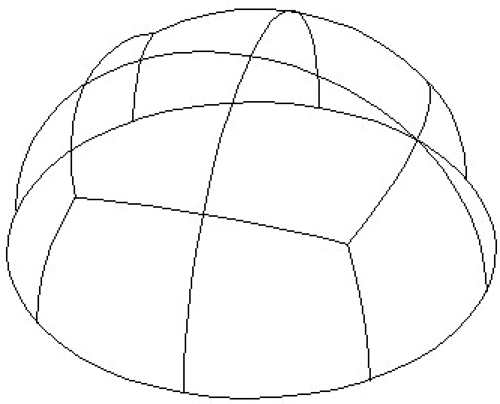

Figure 12 Twelve sectors of the sky dome

Figure 13 Projection of twelve sectors on a fisheye image

The equation (7) shows that smaller patch sizes can increase the precision of the integration. The 12 sectors are very big and information can be lost. So a new division of the sky dome into 256 patches is proposed. There are 32 slices in the azimuthal direction and 8 divisions in the altitudinal direction. So the angles θ,φ are equal to 11.25^{o} (Figure 14). Using this segmentation pattern, luminance values for each patch were derived. These 256 values created the sky luminance distribution map that later were used for daylight simulations.

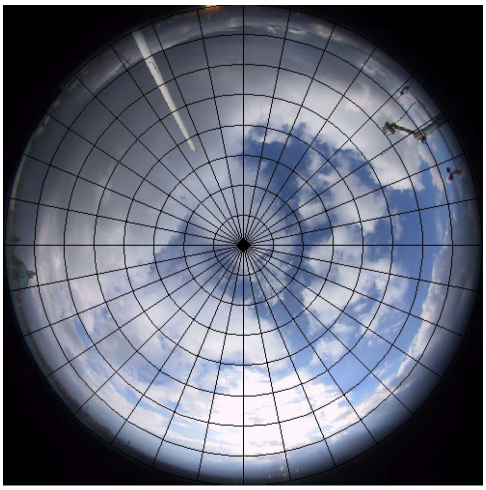

Figure 14 Projection of 256 sky patches on a fisheye image

2.3 Calibration of camera-based luminance measurements

After having extracted the sky luminance distribution maps, their accuracy has to be tested. This can be done with the comparison of the values to the measured values that the sky monitoring device gave. In order to achieve this, the program RADIANCE was used to conduct simulations using the camera-based luminance values and get the horizontal illuminance values.

RADIANCE (Appendix B) is the name of a rendering system developed by G.J. Ward at the Lawrece Berkeley Laboratory (LBL) in California and the Ecole Polytechnique Federale de Lausanne (EPFL) in Switzerland. It is a powerful ray tracing program that enables accurate and physically valid lighting and daylighting simulations (Ward 1994). It is presently well established in the research community and has already been used for many projects.

The sky monitoring device and the real environment where it had been placed during the measurements were modeled in RADIANCE. The tower of the building was modeled too, because it was the basic obstruction and influenced the measurements on the east side of the box (Figure 15). The scene was completed with the use of the sky luminance distribution maps as the sky model. The 12 points that were the sensors' positions were specified and simulations were conducted to calculate the horizontal illuminance reaching them.

It has to be mentioned that the actual values used for the simulations are radiances, as long as RADIANCE works with radiances instead of luminances. These values are luminances divided by the conversion factor of RADIANCE for luminous efficacy which is fixed at K_R = 179 lumens/watt (lm/w) (Larson and Shakespeare 1998).

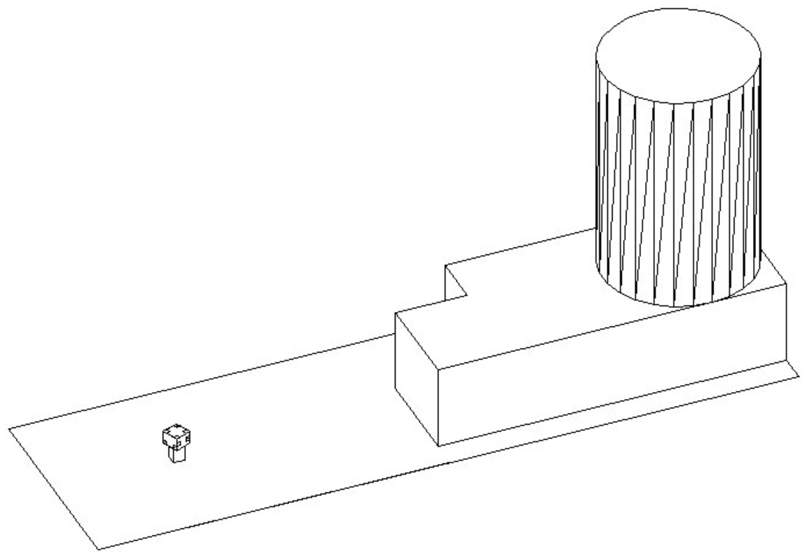

Figure 15 The real scene with the sky monitoring device that was modeled

The calculated values were then compared to the photometrically measured illuminances. Due to various factors, the accuracy of camera-based values is affected. These factors can be the patch size or the number of the patches, the distortion of the fisheye images in the lower areas of the sky dome or even the loss of information because of the compression of the images in JPG format. As past research has demonstrated (Spasojevic and Mahdavi 2005), a correction factor has to be applied to the digitally gained luminance values. Several suggestions were tested in order to find the most accurate sky model for further simulations regarding indoor daylight. These methods of correction that are presented are:

a. uniform correction (100_256)
b. 60%-40% correction (60_1)

c. 100% to one sky patch correction (100_1)
d. 100% to 5 sky patches correction (100_5)

2.3.1 Uniform correction (100_256)

The first method of correction tested was the uniform correction. Here the energy difference was distributed uniformly to all the patches. The luminance of each patch was multiplied by a correction factor so that the sum of the 256 values is the luminance that gives the corresponding measured global horizontal luminance.

$$CF = \frac{E_{total}}{(E_1 + E_2 + ... + E_{256})} \qquad \text{Eq.8}$$

where:

E_{total}	optically measured horizontal illuminance level due to the entire sky dome
E_1 to E_{256}	256 camera based horizontal illuminance levels due to the 256 sky dome sectors

The correction is based on the equation 6. The measured data available are horizontal illuminances. The correction is done so that the global illuminance on the horizontal plane due to the sky dome described is equal to the measured. Then the values are transformed into luminances of the 256 patches.

$$E_i = L_i \cdot \sin\theta_i \cdot \cos\theta_\iota \cdot \Delta\theta_\iota \cdot \Delta\phi_\iota \qquad \text{Eq.6}$$

2.3.2 60% - 40% correction (60_1)

The second correction method tested is an attempt to increase the luminance of the circumsolar region. When the correction factor for uniform correction was less than 1.1, uniform correction was made. When it was greater than 1.1, 60%-40% correction was followed. These were the images where the luminance of the sky patches had to be increased so that the total luminance could be the one that gives the global horizontal illuminance that was measured. The 60% of the energy difference was added to the circumsolar region which consisted of the brightest sky patch and the 40% was distributed to the rest.

In the occasions of non-uniform correction, the correction factor for the sky patch with the maximum luminance is:

$$CF = \frac{0.6(E_{globalmeas} - E_{globalcalc}) + E_{\max calc}}{E_{\max calc}} \quad \text{Eq.9}$$

where:

$E_{globalmeas}$ the measured global illuminance

$E_{globalcalc}$ the global illuminance calculated based on digital images

$E_{maxcalc}$ the calculated illuminance that corresponds to the maximum measured

And the correction factor for the rest of the sky patches is:

$$CF = \frac{0.4(E_{globalmeas} - E_{globalcalc}) + E_{globalcalc} - E_{\max calc}}{E_{globalcalc} - E_{\max calc}} \quad \text{Eq.10}$$

where:

$E_{globalmeas}$ the measured global illuminance

$E_{globalcalc}$ the global illuminance calculated based on digital images

$E_{maxcalc}$ the calculated illuminance that corresponds to the maximum measured

2.3.3 100% to one sky patch correction (100_1)

The third correction method had as an objective to increase even more the luminance of the circumsolar region. The condition whether the correction factor was greater than 1.1 or not was again used here. If it was not, uniform correction was followed. If it was greater than 1.1, the whole difference between the measured global illuminance and the illuminance due to the 256 patches of the image was added to the circumsolar region which consisted again of the brightest sky patch.

In the occasions of non-uniform correction, the correction factor for the sky patch with the maximum luminance is:

$$CF = \frac{E_{globalmeas} - E_{globalcalc} + E_{\max calc}}{E_{\max calc}} \qquad \text{Eq.11}$$

where:

$E_{globalmeas}$ the measured global illuminance

$E_{globalcalc}$ the global illuminance calculated based on digital images

$E_{maxcalc}$ the calculated illuminance that corresponds to the maximum measured

The rest of the sky patches maintained the initial luminance values extracted from the images.

2.3.4 100% to 5 sky patches correction (100_5)

This last correction method was based on the previous one. When the correction factor was greater than 1.1, instead of adding the whole difference to one sky patch, it was distributed to the brightest patch and four adjacent patches. The conditions to choose those 4 patches was their luminance. When there were more patches with the same luminance the ones nearest to the center of the brightest sky patch were chosen.

The correction factor for the 5 patches in the occasions of non-uniform correction was the same as in the correction of one sky patch with the substitution of $E_{maxcalc}$ by the sum of the illuminances due to the 5 patches selected.

$$CF = \frac{E_{globalmeas} - E_{globalcalc} + \sum_{i=1}^{5} E_i}{\sum_{i=1}^{5} E_i} \qquad \text{Eq.12}$$

where:

$E_{globalmeas}$	the measured global illuminance
$E_{globalcalc}$	the global illuminance calculated based on digital images
$\sum_{i=1}^{5} E_i$	the sum of the calculated illuminances due to the 5 sky patches selected

The best method of correction was chosen for calibration of the images and this was used for the last step of the research that has as an objective the validation of the sky model created.

2.4 Indoor illuminance prediction

2.4.1 Digital images

The procedure followed up to now leads to the derivation of sky luminance distribution maps. The best one of those sky models was chosen and it was used for indoor daylight simulations.

The scale model that was used for the measurements was modeled in RADIANCE. Again the real environment was modeled (Figure 16). The camera-based values were used as the sky model and an upside-down sky was used as suggested (Larson and Shakespeare 1998). This mirrored sky is used in order to avoid a gap between the sky dome and the edge of the ground at the horizon. It represents a luminous ground and its brightness is defined by the sky's luminance.

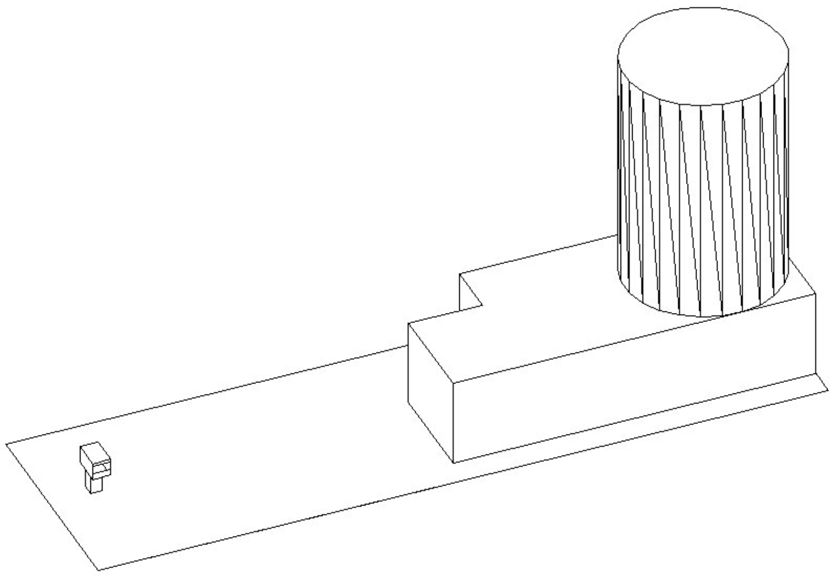

Figure 16 The real scene with the scale model that was modeled

The three points where the sensors were inside the model were determined (points P1, P2, P3 as shown in Figure 8). Simulations were conducted and the horizontal illuminance that reaches them was calculated. Actually, two sets of simulations were conducted. One is when the model faced towards north and one when it faced towards south.

To test the potential of this approach, the calculated results were compared to the measured values, but also simulations were conducted with the use of other sky models too. The models selected are the ones mostly used: the CIE Standard Skies and the Perez All-weather model, which is currently considered as the most reliable.

2.4.2 CIE Standard Skies

The same modeled environment was used and the CIE Standard Skies were used as the sky model for the simulations conducted.

The CIE has made attempts to create model skies that are a valuable tool for everybody dealing with daylight. At the beginning, when the calculations were done by hand or with tables, the standard uniform sky was used. It was characterized by a uniform luminance that does not change with altitude or azimuth. The three standard skies (Figure 17) that are now used for simulations are: overcast, intermediate and clear sky (Sky types 2006).

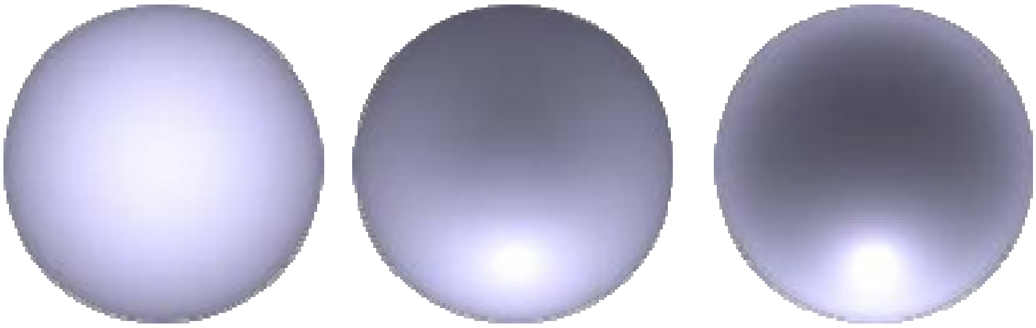

Figure 17 The three CIE Standards Skies: overcast, intermediate, clear
(Sky types 2006)

-*Overcast sky* : the luminance of the standard CIE overcast sky changes with altitude. It is three times as bright in zenith as it is near the horizon and the trigonometric relation that describes this is the following (Darula and Kittler 2002):

$$\frac{L_\gamma}{L_z} = \frac{1+2\sin\gamma}{3} = \frac{1+2\cos Z}{3} \qquad \text{Eq.13}$$

where:

$L\gamma$ luminance of a sky element in cd m^{-2}
Lz zenith luminance in cd m^{-2}
γ elevation angle of a sky element above the horizon
Z angular distance between a sky element and the zenith, $Z=90^{o} - \gamma$

This standard sky was first proposed by Moon and Spencer. The overcast sky is used when measuring daylight factors.

-*Clear sky* : the luminance of the standard CIE clear sky varies over both, altitude and azimuth. It is brightest around the sun and dimmest opposite it. The brightness of the horizon lies between those two extremes.

-*Intermediate sky* : the standard CIE intermediate sky is a somewhat hazy variant of the clear sky. The sun is not as bright as the clear sky and the brightness changes are not as drastic.

Figure 18 shows the sky distributions for the CIE skies (Sky types 2006). These were generated with RADIANCE. The sun was assumed to be at an altitude of 60 B° due South. The sky luminance was then mapped between the Southern (0B°) and the Northern (180B°) horizon passing through the zenith (90B°).

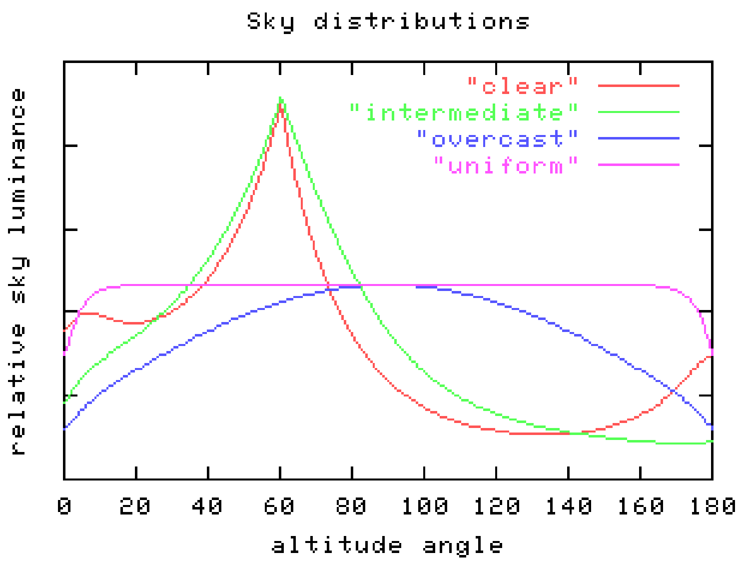

Figure 18 Sky luminance distribution for the CIE skies
(Sky types 2006)

The Radiance sky generator program was used to produce sun descriptions and sky brightness distributions that correspond to the CIE overcast, intermediate or clear skies. The selection of the appropriate sky model was based on visual inspection of the images taken during the days of the collection of measurements. The cloudy skies were characterized as overcast; the ones partially covered with clouds were characterized as intermediate and the skies with no clouds as clear. The sky model was generated based on the longitude and latitude of Vienna and the sky brightness was specified in terms of the horizontal diffuse irradiance (-B). Figure 19 gives examples of images from each one of the sky types.

Figure 19 Example of images characterized as overcast, intermediate, clear

2.4.3 Perez All-Weather sky model

Perez et al. developed a five parameter model to describe the sky luminance distribution. Each parameter has a specific physical effect on the sky distribution. These parameters relate to (Perez et al. 1993):

a darkening or brightening of the horizon

b luminance gradient near the horizon

c relative intensity of the circumsolar region

d width of the circumsolar region

e relative backscattered light

The model is given by:

$$F(\zeta,\gamma) = (1+\alpha \cdot e^{b/\cos\theta})(1+c \cdot e^{d\gamma} + e \cdot \cos^2 \gamma) \qquad \text{Eq.14}$$

where:

ζ	zenith angle of the considered sky element
γ	angle between this sky element and the position of the sun
α,b,c,d,e	adjustable coefficients

The scene generated in RADIANCE is based on an angular distribution of the daylight sources (direct and diffuse) for the given atmospheric conditions (direct and diffuse component of the solar radiation), date and local standard time. The diffuse angular distribution is calculated by the Perez model which describes the mean instantaneous sky luminance angular distribution patterns for all sky conditions from overcast to clear, through partly cloudy, skies. The direct radiation is understood as the radiant flux coming from the sun and an area of approximately 3 degrees around the sun. The sun is represented as a disk.

A third set of simulations were conducted with All-weather sky model. The direct and diffuse solar illuminances are the inputs needed for the calculations. The sensors used gave the global horizontal illuminance. So the necessary data was not directly available. A formula to derive them was suggested:

$$E_{direct} = E_{max} - \frac{E_{global} - E_{max}}{11} \qquad \text{Eq.15}$$

$$E_{diffuse} = E_{global} - E_{direct} \qquad \text{Eq.16}$$

where:

E_{direct} the illuminance due to the direct component of the sky dome

$E_{diffuse}$ the illuminance due to the rest sky dome

E_{max} the maximum illuminance value measured

E_{global} the global horizontal illuminance measured

Actually the average of the 11 measured values - excluding the maximum one - was considered to be the diffuse energy due to each one of the 12 sky sectors. So the direct component of the sky can be calculated from the horizontal illuminance of the maximum value if this energy is subtracted.

This was used only in the occasions when the corresponding image had correction factor for uniform correction greater than 1.1. When this correction factor was less than 1.1, it was considered that the sky had negligible direct component.

Generally the input data necessary for the simulations conducted in RADIANCE (Appendix B) are concentrated in the following table:

Table 2 The input data for RADIANCE

Data	**Type of input**	
Geometry of the scene	Textfile with coordinates for each surface	
Materials	Textfile with the characteristics of each material	
Ambient discription	Parameters that describe the resolution and accuracy of the image generated	
Sky model	CIE Skies	Date and time Longitude and altitude of location Type of Standard Sky Global horizontal illuminance
	Perez All-weather sky	Date and time Longitude and altitude of location Direct normal illuminance and diffuse horizontal illuminance
	Digital imaging	File with the luminance values of the 256 patches

The three sets of calculated values obtained from the simulations with the use of the three sky models were compared to the measured values in order to observe the effects of the selection of a sky model on the indoor daylight predictions.

3. Results

3.1 Derivation of sky luminance distribution maps from digital images

3.1.1 Extraction of luminance data from images

The results from the Java metadata extractor are files - one for each image - with the radiances for the 256 patches. Actually the radiance distribution maps are created, so that these files can be directly used as input for the sky model in RADIANCE. The files are of the following format:

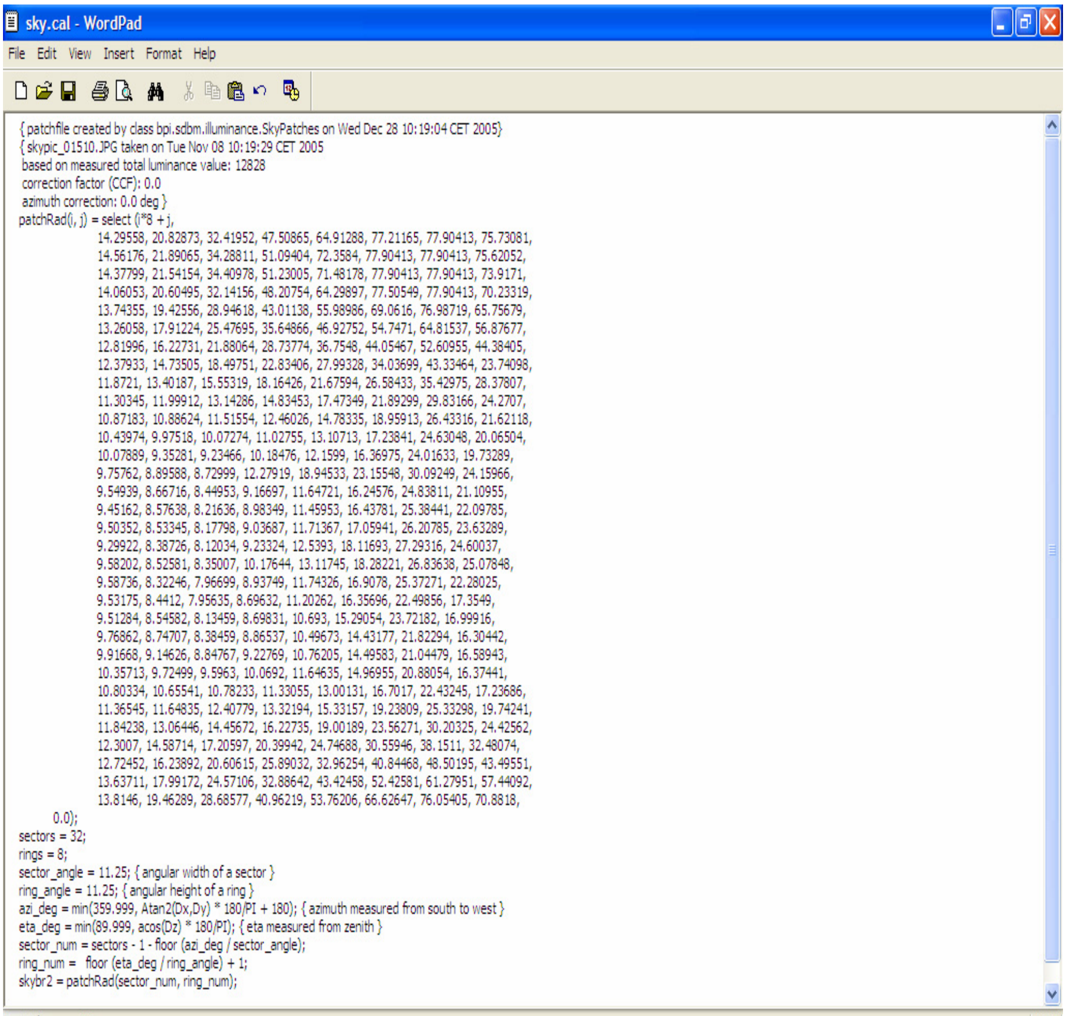


```
{ patchfile created by class bpi.sdbm.illuminance.SkyPatches on Wed Dec 28 10:19:04 CET 2005}
{ skypic_01510.JPG taken on Tue Nov 08 10:19:29 CET 2005
 based on measured total luminance value: 12828
 correction factor (CCF): 0.0
 azimuth correction: 0.0 deg }
patchRad(i, j) = select (i*8 + j,
                14.29558, 20.82873, 32.41952, 47.50865, 64.91288, 77.21165, 77.90413, 75.73081,
                14.56176, 21.89065, 34.28811, 51.09404, 72.3584, 77.90413, 77.90413, 75.62052,
                14.37799, 21.54154, 34.40978, 51.23005, 71.48178, 77.90413, 77.90413, 73.9171,
                14.06053, 20.60495, 32.14156, 48.20754, 64.29897, 77.50549, 77.90413, 70.23319,
                13.74355, 19.42556, 28.94618, 43.01138, 55.98986, 69.0616, 76.98719, 65.75679,
                13.26058, 17.91224, 25.47695, 35.64866, 46.92752, 54.7471, 64.81537, 56.87677,
                12.81996, 16.22731, 21.88064, 28.73774, 36.7548, 44.05467, 52.60955, 44.38405,
                12.37933, 14.73505, 18.49751, 22.83406, 27.99328, 34.03699, 43.33464, 23.74098,
                11.8721, 13.40187, 15.55319, 18.16426, 21.67594, 26.58433, 35.42975, 28.37807,
                11.30345, 11.99912, 13.14286, 14.83453, 17.47349, 21.89299, 29.83166, 24.2707,
                10.87183, 10.88624, 11.51554, 12.46026, 14.78335, 18.95913, 26.43316, 21.62118,
                10.43974, 9.97518, 10.07274, 11.02755, 13.10713, 17.23841, 24.63048, 20.06504,
                10.07889, 9.35281, 9.23466, 10.18476, 12.1599, 16.36975, 24.01633, 19.73289,
                9.75762, 8.89588, 8.72999, 12.27919, 18.94533, 23.15548, 30.09249, 24.15966,
                9.54939, 8.66716, 8.44953, 9.16697, 11.64721, 16.24576, 24.83811, 21.10955,
                9.45162, 8.57638, 8.21636, 8.98349, 11.45953, 16.43781, 25.38441, 22.09785,
                9.50352, 8.53345, 8.17798, 9.03687, 11.71367, 17.05941, 26.20785, 23.63289,
                9.29922, 8.38726, 8.12034, 9.23324, 12.5393, 18.11693, 27.29316, 24.60037,
                9.58202, 8.52581, 8.35007, 10.17644, 13.11745, 18.28221, 26.83638, 25.07848,
                9.58736, 8.32246, 7.96699, 8.93749, 11.74326, 16.9078, 25.37271, 22.28025,
                9.53175, 8.4412, 7.95635, 8.69632, 11.20262, 16.35696, 22.49856, 17.3549,
                9.51284, 8.54582, 8.13459, 8.69831, 10.693, 15.29054, 23.72182, 16.99916,
                9.76862, 8.74707, 8.38459, 8.86537, 10.49673, 14.43177, 21.82294, 16.30442,
                9.91668, 9.14626, 8.84767, 9.22769, 10.76205, 14.49583, 21.04479, 16.58943,
                10.35713, 9.72499, 9.5963, 10.0692, 11.64635, 14.96955, 20.88054, 16.37441,
                10.80334, 10.65541, 10.78233, 11.33055, 13.00131, 16.7017, 22.43245, 17.23686,
                11.36545, 11.64835, 12.40779, 13.32194, 15.33157, 19.23809, 25.33298, 19.74241,
                11.84238, 13.06446, 14.45672, 16.22735, 19.00189, 23.56271, 30.20325, 24.42562,
                12.3007, 14.58714, 17.20597, 20.39942, 24.74688, 30.55946, 38.1511, 32.48074,
                12.72452, 16.23892, 20.60615, 25.89032, 32.96254, 40.84468, 48.50195, 43.49551,
                13.63711, 17.99172, 24.57106, 32.88642, 43.42458, 52.42581, 61.27951, 57.44092,
                13.8146, 19.46289, 28.68577, 40.96219, 53.76206, 66.62647, 76.05405, 70.8818,
        0.0);
sectors = 32;
rings = 8;
sector_angle = 11.25; { angular width of a sector }
ring_angle = 11.25; { angular height of a ring }
azi_deg = min(359.999, Atan2(Dx,Dy) * 180/PI + 180); { azimuth measured from south to west }
eta_deg = min(89.999, acos(Dz) * 180/PI); { eta measured from zenith }
sector_num = sectors - 1 - floor (azi_deg / sector_angle);
ring_num =  floor (eta_deg / ring_angle) + 1;
skybr2 = patchRad(sector_num, ring_num);
```

Figure 20 The file format with the radiances for the 256 patches

3.1.2 Calibration of camera-based luminance measurements

RADIANCE was used for simulations in order to get horizontal illuminance values at the 12 points defined in the model of the sky monitoring device. The sky model created after the extraction of the luminance values from each picture was used. So RADIANCE models the sky according to the pattern of the 256 patches. An example is given in Figure 21.

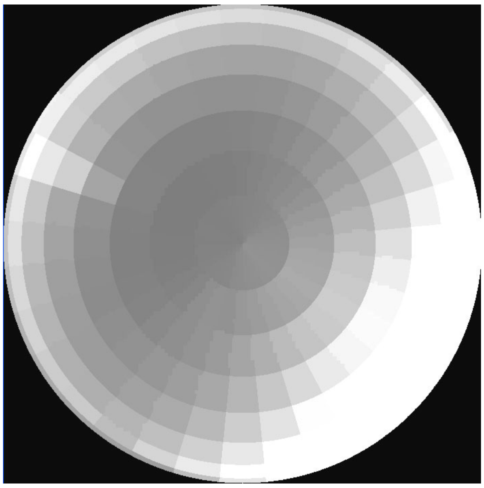

Figure 21 A fisheye view of the sky as generated in RADIANCE based on digital imaging

a. Initial extracted values versus measured values

Figure 22 shows the relationship between the horizontal illuminances that reach the 12 points defined as:

a. calculated in RADIANCE with the use of the camera-based values. Here the 12 points are the positions of the sensors in the sky monitoring device as modeled in the program (horizontal axis)
b. measured from the 12 sensors in the monitoring device (vertical axis)

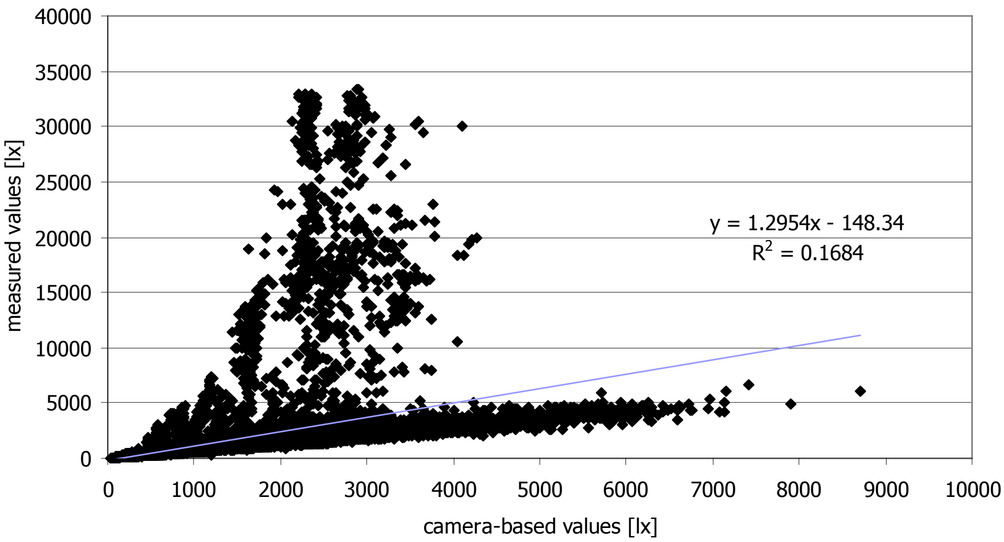

Figure 22 Photometrically measured versus initial camera-based illuminance values

The correlation coefficient (r^2) of the corresponding linear regression amounts to 0.17. As it has been mentioned and as it can be observed by this correlation, the camera based values need a correction so that the sky model created can be more accurate.

Table 3 shows the corresponding coefficients (r^2) that indicate the relationship between the camera-based values and the measured ones for each one of the 12 points (Appendix C.1). The names given to each point is derived from the position of each sensor and the sky sector it looked at (Figures 23, 24).

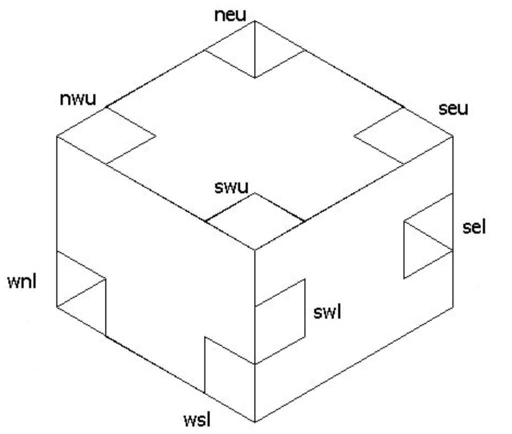

Figure 23 The names corresponding to each point in the sky monitoring device

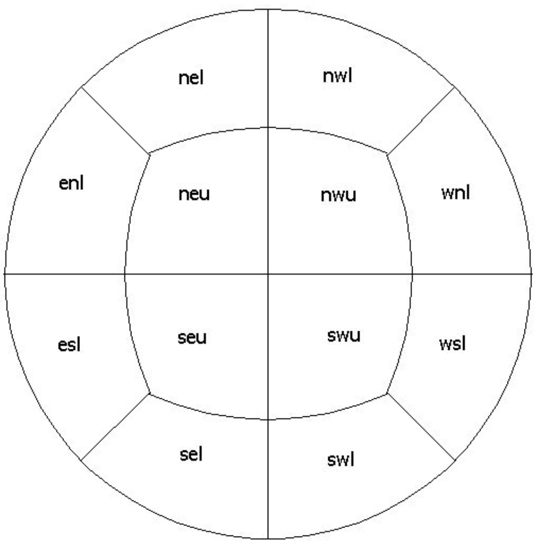

Figure 24 The names corresponding to each one of the sky sectors as mapped on the images

Table 3 The r^2 that show the relationship between the initial camera-based values and the measured ones for each one of the 12 points

Point	Correlation coefficient (r^2)
nwl	0.88
wnl	0.63
wsl	0.30
swl	0.52
sel	0.30
esl	0.82
enl	0.91
nel	0.88
nwu	0.90
swu	0.88
seu	0.95
neu	0.93

b. Uniform correction

The first correction method tested was uniform correction. Figure 25 shows the relationship between the camera-based illuminances after uniform correction and the measured ones. The correlation coefficient of this linear regression amounts to 0.36. Table 4 shows the corresponding coefficients that indicate the relationship between the camera-based values and the measured ones for each one of the 12 points (Appendix C.2).

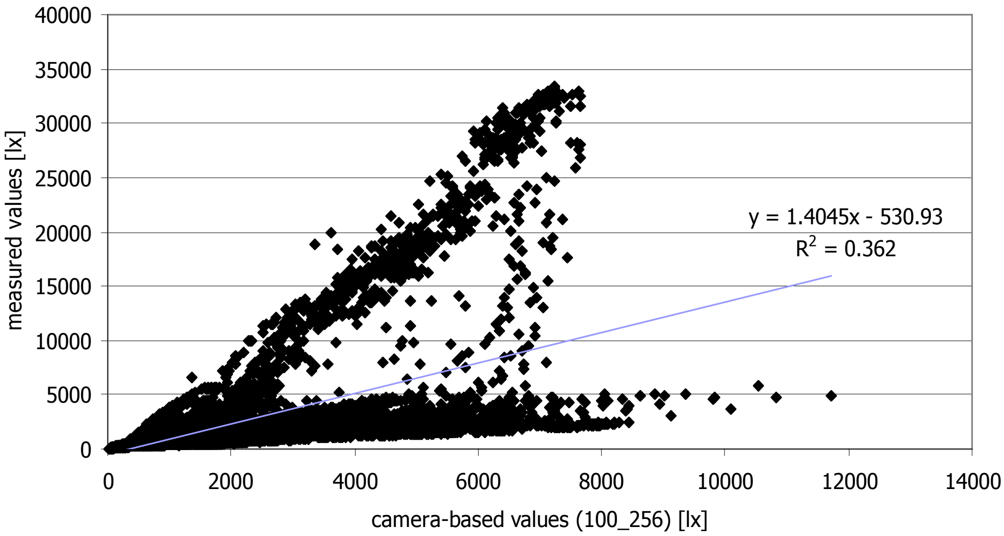

Figure 25 Photometrically measured versus calibrated camera-based illuminance values (100_256)

Table 4 The r^2 that show the relationship between the calibrated camera-based values and the measured ones for each one of the 12 points (100_256)

Point	**Correlation coefficient (r^2)**
nwl	0.40
wnl	0.58
wsl	0.27
swl	0.74
sel	0.60
esl	0.62
enl	0.34
nel	0.27
nwu	0.64
swu	0.47
seu	0.42
neu	0.58

c. 60%-40% correction

The second correction method led to non-uniform correction. When the energy difference is more than 10% of the camera-based value, 60% of it is added to the circumsolar region which consists of the brightest sky patch. Figure 26 shows the relationship between the camera-based illuminances after this correction and the measured values. The correlation coefficient is 0.87.

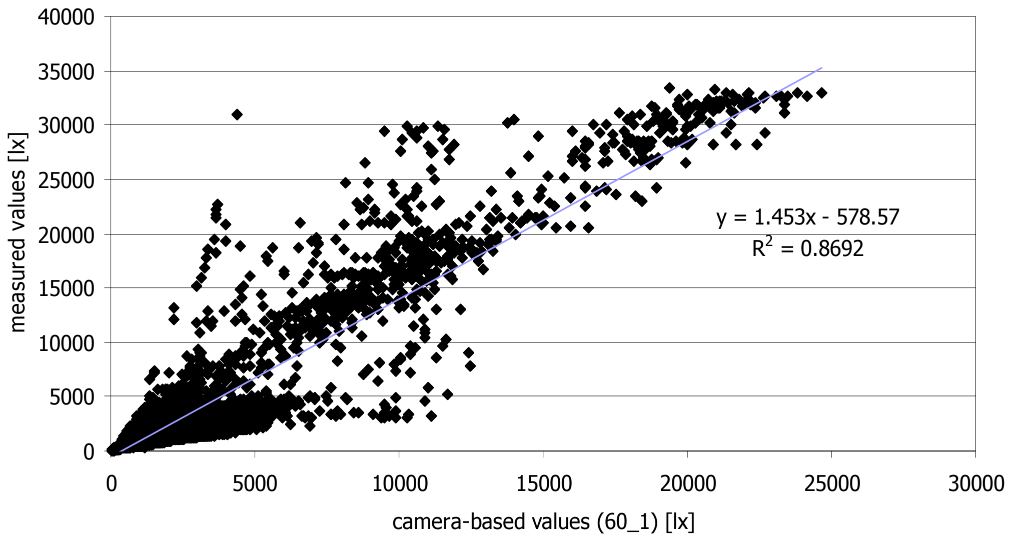

Figure 26 Photometrically measured versus calibrated camera-based illuminance values (60_1)

Table 5 shows the corresponding correlation coefficients that indicate the relationship between the camera-based values and the measured ones for each one of the 12 points (Appendix C.3).

Table 5 The r^2 that show the relationship between the calibrated camera-based values and the measured ones for each one of the 12 points (60_1)

Point	Correlation coefficient (r^2)
nwl	0.67
wnl	0.80
wsl	0.49
swl	0.90
sel	0.93
esl	0.80
enl	0.59
nel	0.48
nwu	0.90
swu	0.76
seu	0.70
neu	0.86

c. *100% to one sky patch correction*

The third correction method increases even more the circumsolar region. When the energy difference is more than 10% of the camera-based value, it is all added to the brightest sky patch. Figure 27 shows the relationship between the camera-based illuminances after this correction and the measured values. The correlation coefficient is 0.91.

Table 6 shows the corresponding correlation coefficients that indicate the relationship between the camera-based values and the measured ones for each one of the 12 points (Appendix C.4)

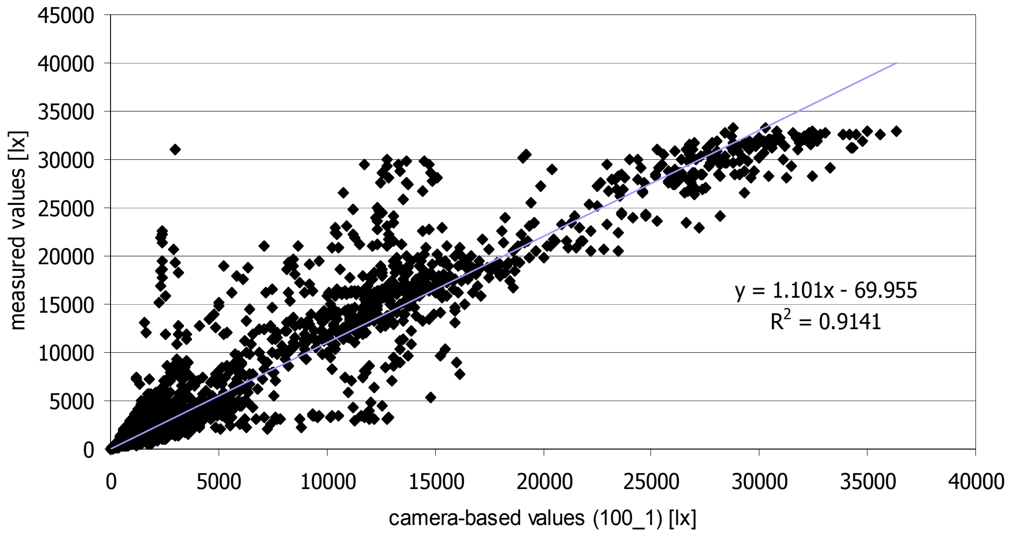

Figure 27 Photometrically measured versus calibrated camera-based illuminance values (100_1)

Table 6 The r^2 that show the relationship between the calibrated camera-based values and the measured ones for each one of the 12 points (100_1)

Point	Correlation coefficient (r^2)
nwl	0.90
wnl	0.85
wsl	0.66
swl	0.88
sel	0.94
esl	0.90
enl	0.83
nel	0.73
nwu	0.96
swu	0.93
seu	0.92
neu	0.95

e. 100% to 5 sky patches correction

The forth correction method is based on the previous one. Here, when the energy difference is more than 10% of the camera-based value, it is distributed to the extended circumsolar region which consists of the 5 brightest sky patches. Figure 28 shows the relationship between the camera-based illuminances after this correction and the measured values. The correlation coefficient is 0.955.

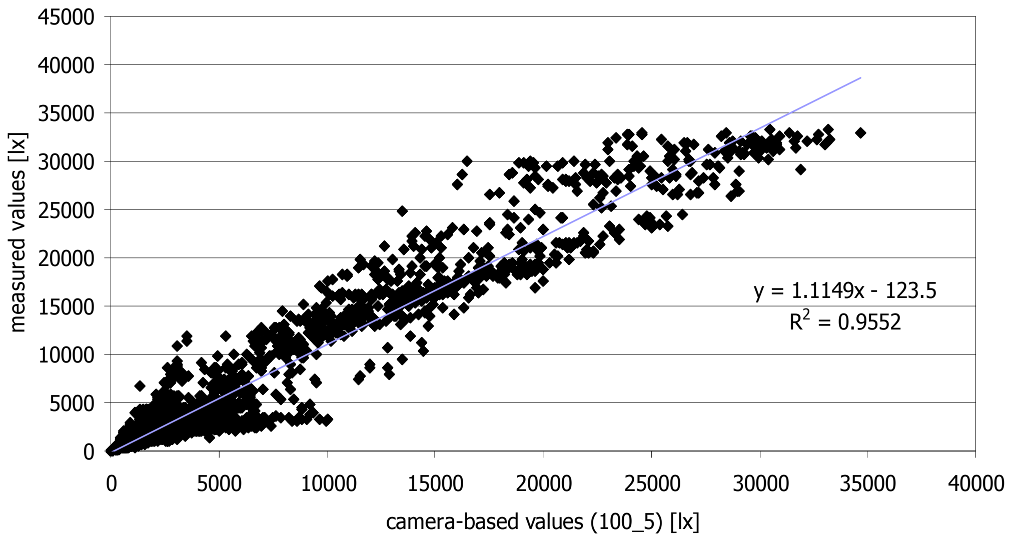

Figure 28 Photometrically measured versus calibrated camera-based illuminance values (100_5)

Table 7 shows the corresponding coefficients that indicate the relationship between the camera-based values and the measured ones for each one of the 12 points (Appendix C.5).

Table 7 The r^2 that show the relationship between the calibrated camera-based values and the measured ones for each one of the 12 points (100_5)

Point	Correlation coefficient (r^2)
nwl	0.90
wnl	0.85
wsl	0.71
swl	0.95
sel	0.97
esl	0.90
enl	0.83
nel	0.73
nwu	0.95
swu	0.93
seu	0.90
neu	0.95

After those four methods of correction are tested, the best sky model is chosen. When the difference between the global illuminance measured and the horizontal illuminance level due to the 256 patches is distributed to the brightest 5 sky patches, the results are better. Such a correction can thus be applied to the data gained through digital photography in order to provide more accurate patch luminance values for daylight simulation applications.

3.2 Indoor illuminance prediction

3.2.1 Digital images

The sky luminance distribution maps derived from the digital images with the correction method selected are now used for indoor simulations. Figure 29 illustrates the relationship between the simulated illuminance values based on the sky model created from digital imaging (horizontal axis) and the measured indoor illuminance values (vertical axis). The correlation coefficient of this linear regression is 0.96.

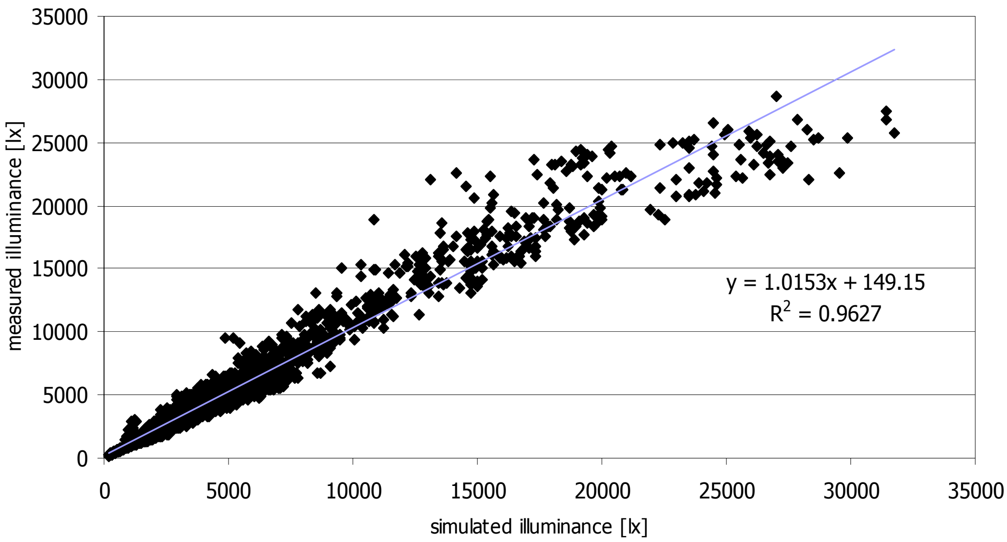

Figure 29 Simulated versus measured indoor illuminance values (sky luminance data based on digital imaging)

Two sets of simulations were conducted: one is when the model faced towards the north and one when it faced towards the south. Figure 30 illustrates the linear regression between simulated illuminance values and measured values when the model faced towards the north and figure 34 when it faces towards south. Figures 31-33 show the corresponding linear regressions for each one of the points in the model when it faced towards north and figures 35-37 when it faced towards south.

a. The model faces north

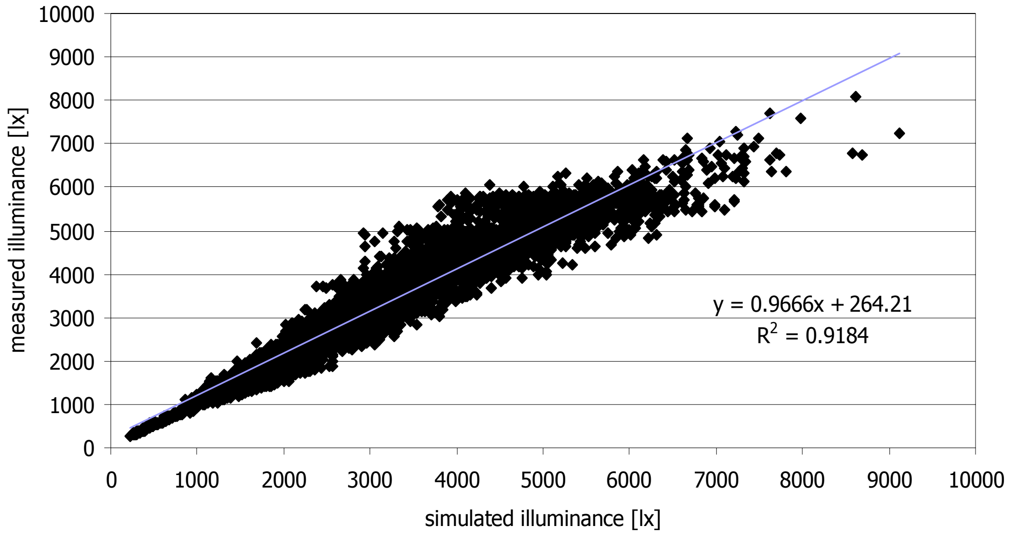

Figure 30 Simulated versus measured indoor illuminance values when the model faces north (sky luminance data based on digital imaging)

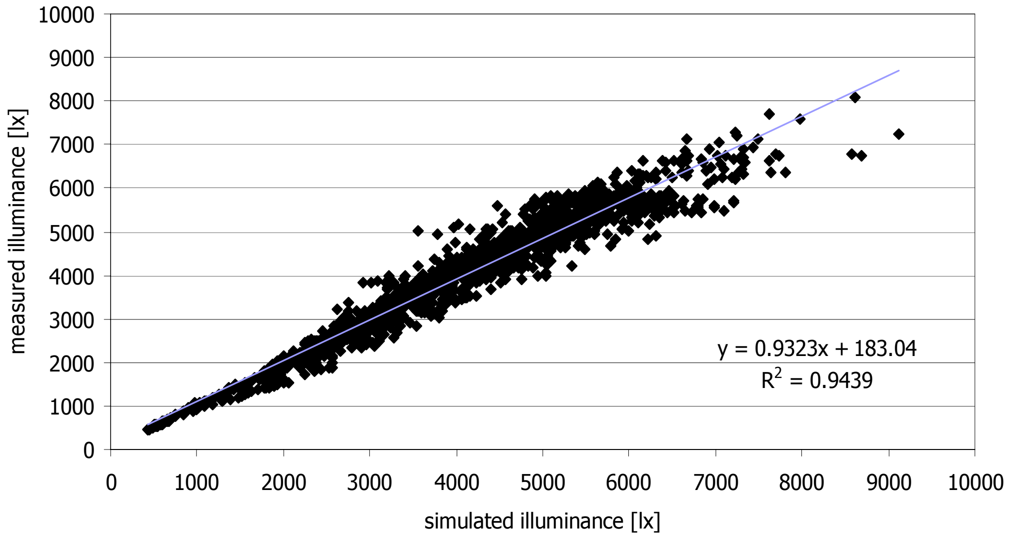

Figure 31 Simulated versus measured indoor illuminance values for P1_north (sky luminance data based on digital imaging)

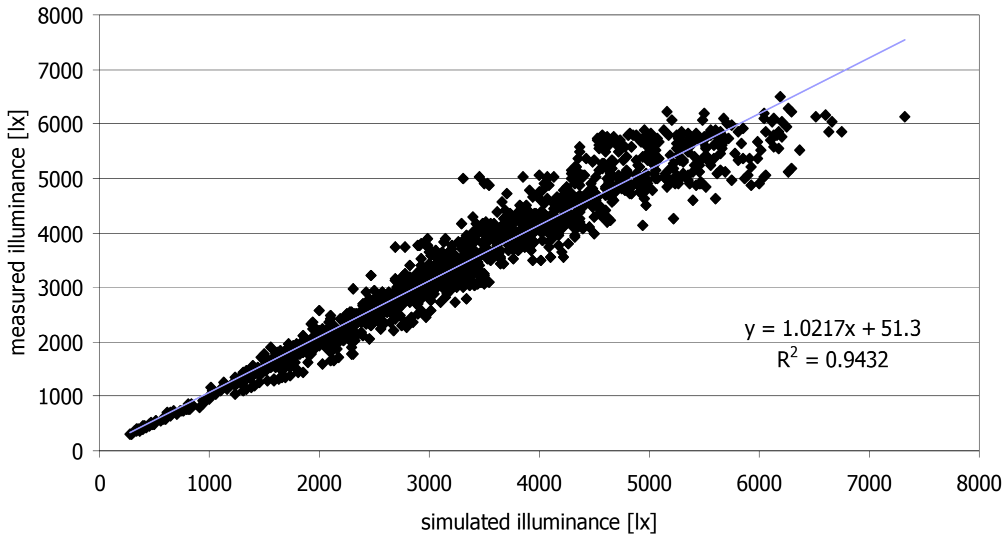

Figure 32 Simulated versus measured indoor illuminance values for P2_north (sky luminance data based on digital imaging)

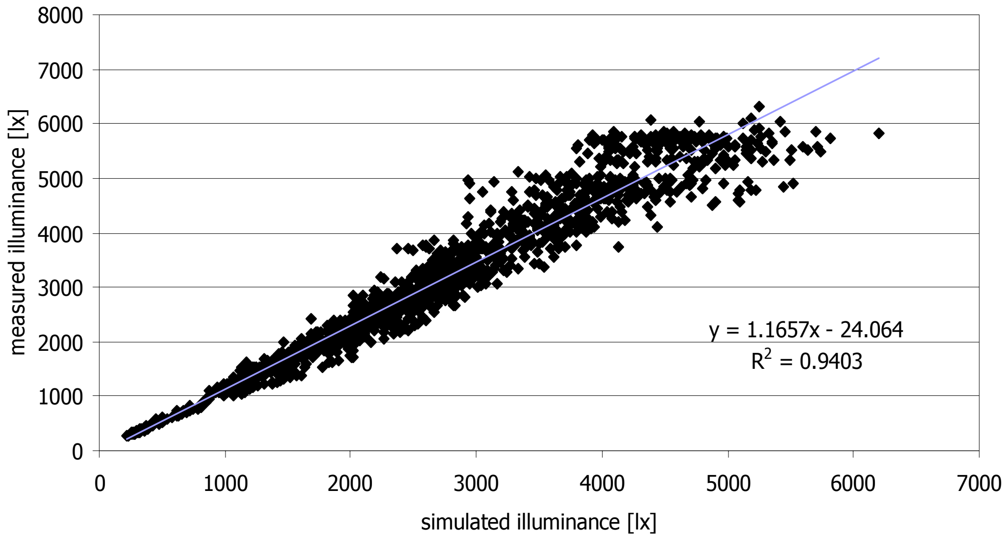

Figure 33 Simulated versus measured indoor illuminance values for P3_north (sky luminance data based on digital imaging)

b. The model faces south

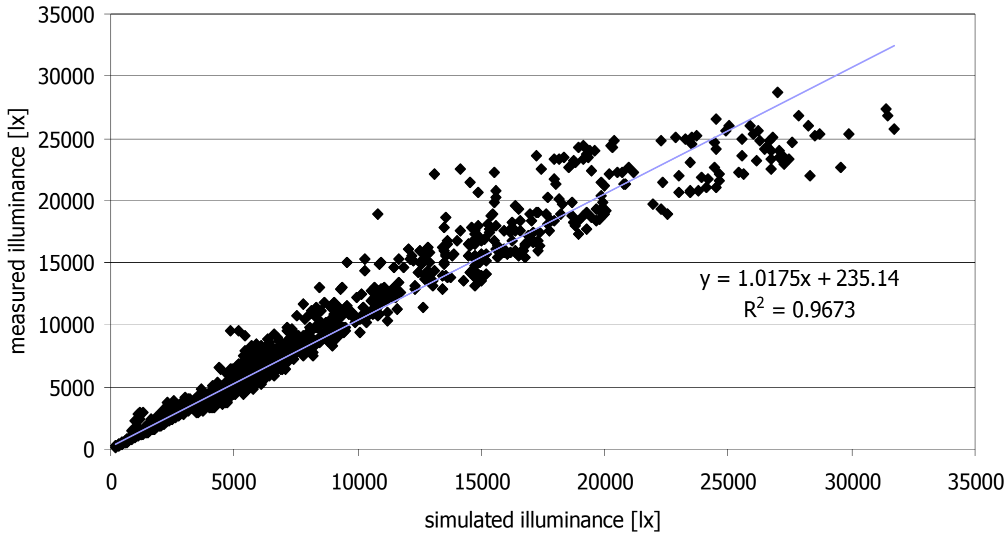

Figure 34 Simulated versus measured indoor illuminance values when the model faces south (sky luminance data based on digital imaging)

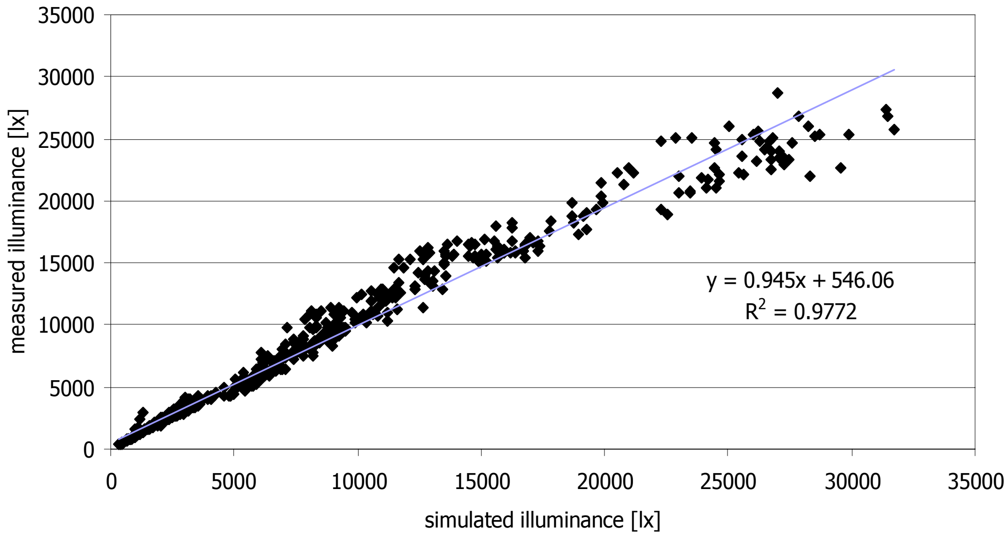

Figure 35 Simulated versus measured indoor illuminance values for P1_south (sky luminance data based on digital imaging)

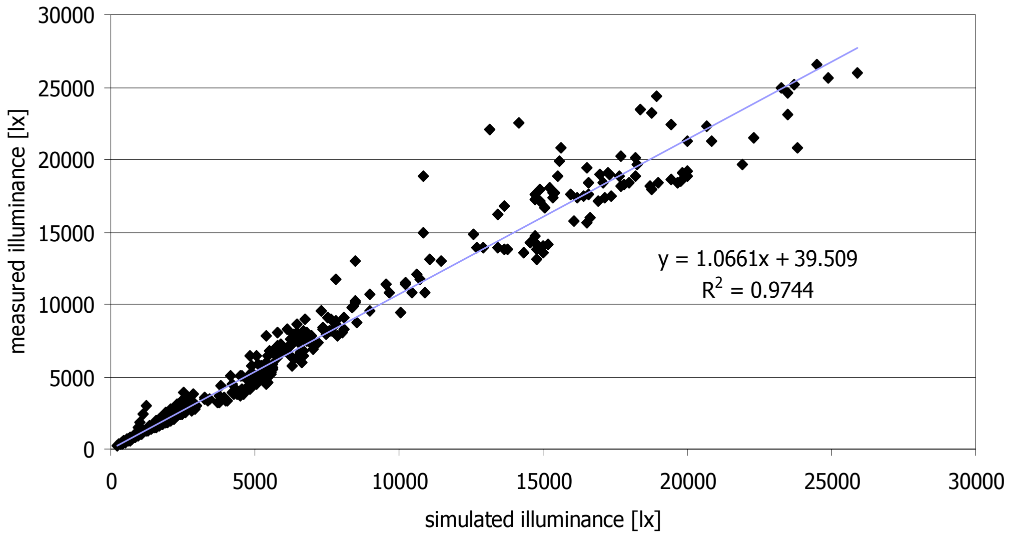

Figure 36 Simulated versus measured indoor illuminance values for P2_south (sky luminance data based on digital imaging)

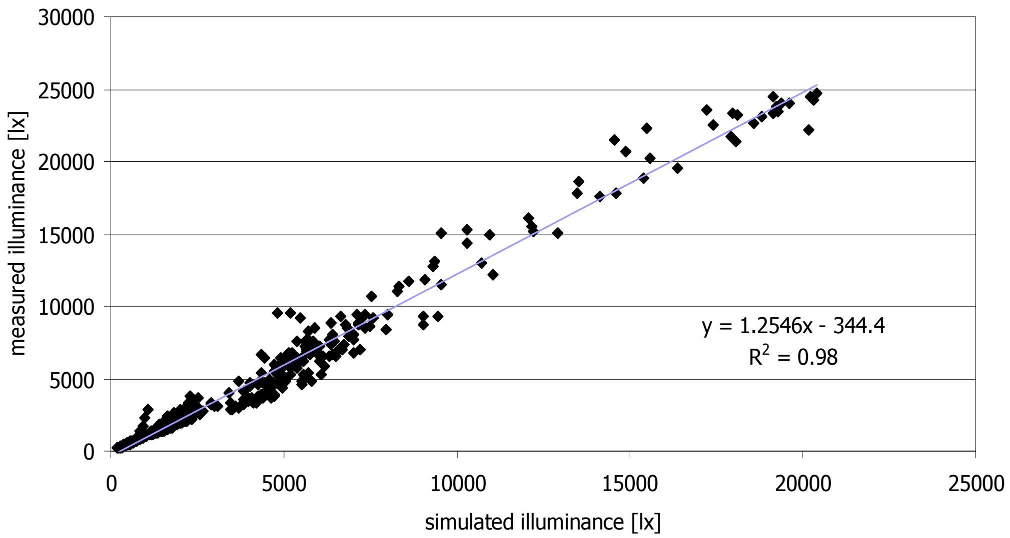

Figure 37 Simulated versus measured indoor illuminance values for P3_south (sky luminance data based on digital imaging)

3.2.2 CIE Standard Skies

Two sets of simulations were conducted with the use of the CIE Standard Sky models. The irradiances needed as input data are the measured global illuminances divided by 179 (Chapter 2.3). Figure 38 illustrates the relationship between the simulated illuminance values based on the CIE Standard sky models (horizontal axis) and the measured indoor illuminance values (vertical axis). The correlation coefficient of this linear regression is 0.74.

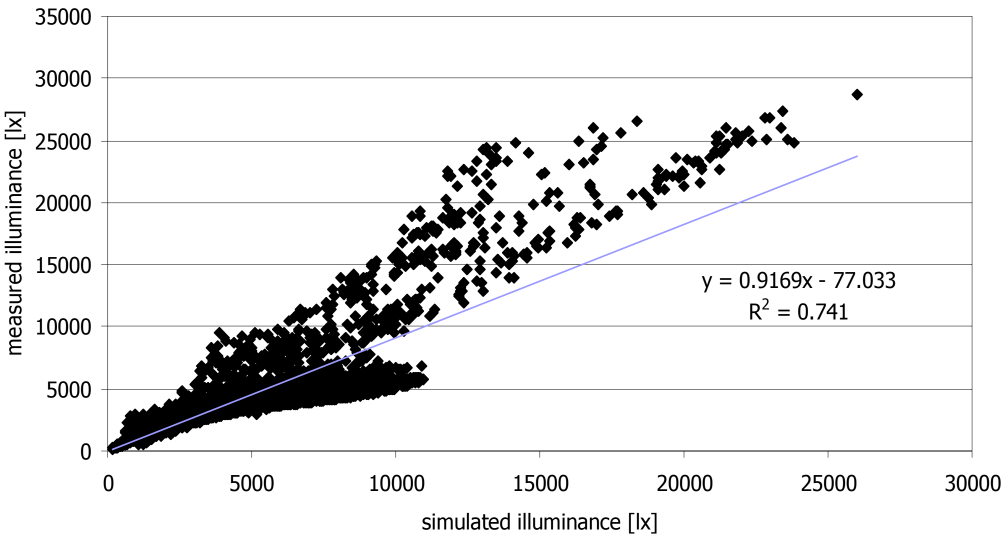

Figure 38 Simulated versus measured indoor illuminance values (sky luminance data based on CIE Standard Skies)

The same procedure with two sets of simulations according to the orientation of the model was followed. The corresponding results are illustrated in the following figures (39-46):

a. The model faces north

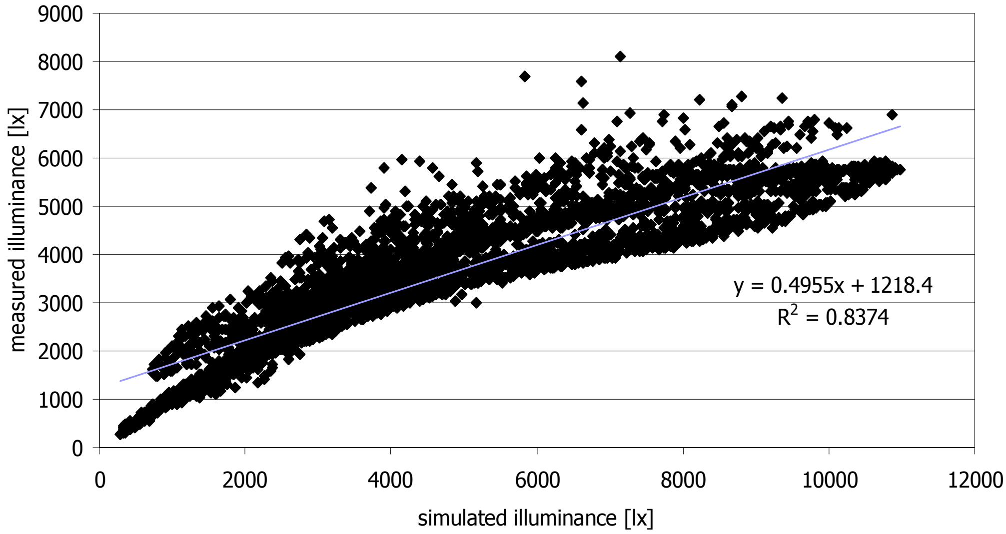

Figure 39 Simulated versus measured indoor illuminance values when the model faces north (sky luminance data based on CIE Standard Skies)

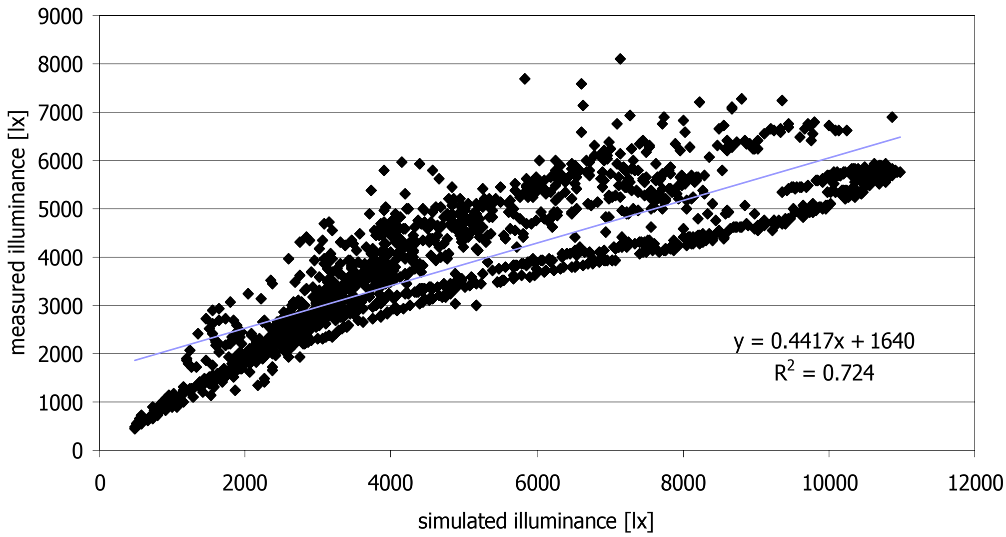

Figure 40 Simulated versus measured indoor illuminance values for P1_north (sky luminance data based on CIE Standard Skies)

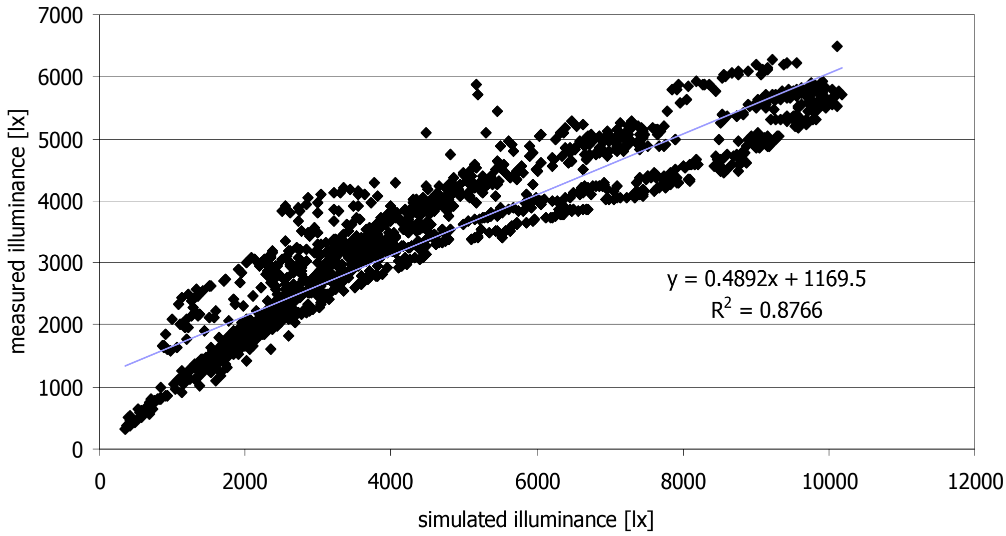

Figure 41 Simulated versus measured indoor illuminance values for P2_north (sky luminance data based on CIE Standard Skies)

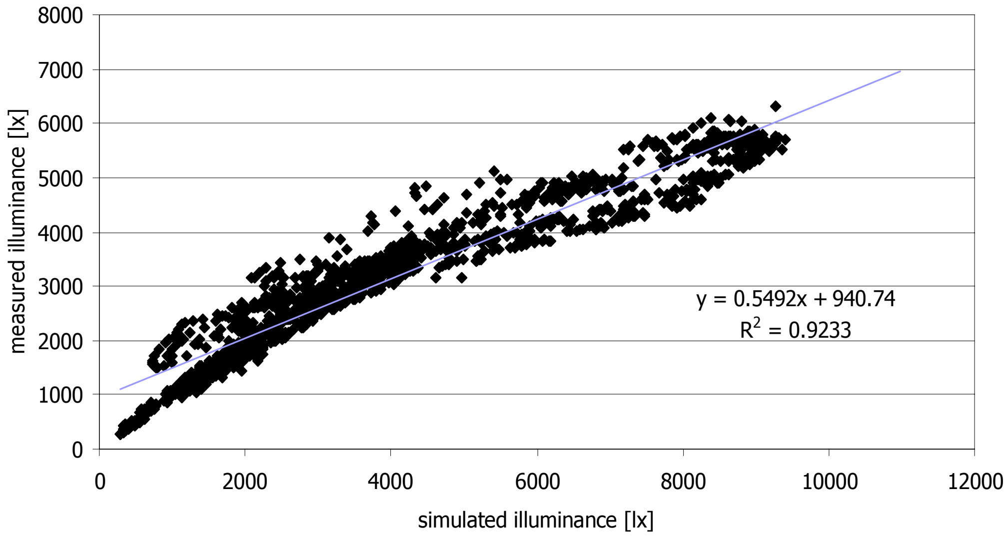

Figure 42 Simulated versus measured indoor illuminance values for P3_north (sky luminance data based on CIE Standard Skies)

b. The model faces south

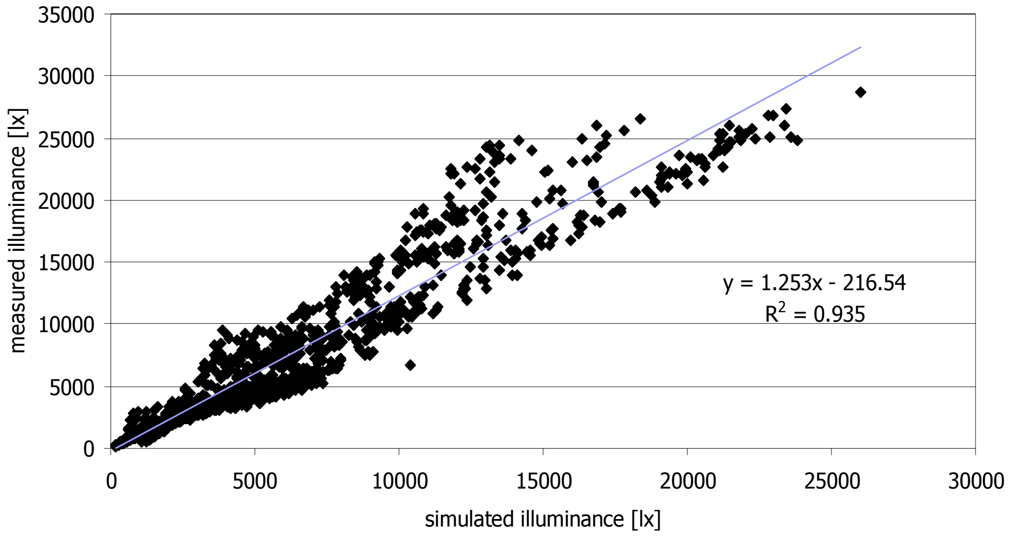

Figure 43 Simulated versus measured indoor illuminance values when the model faces south (sky luminance data based on CIE Standard Skies)

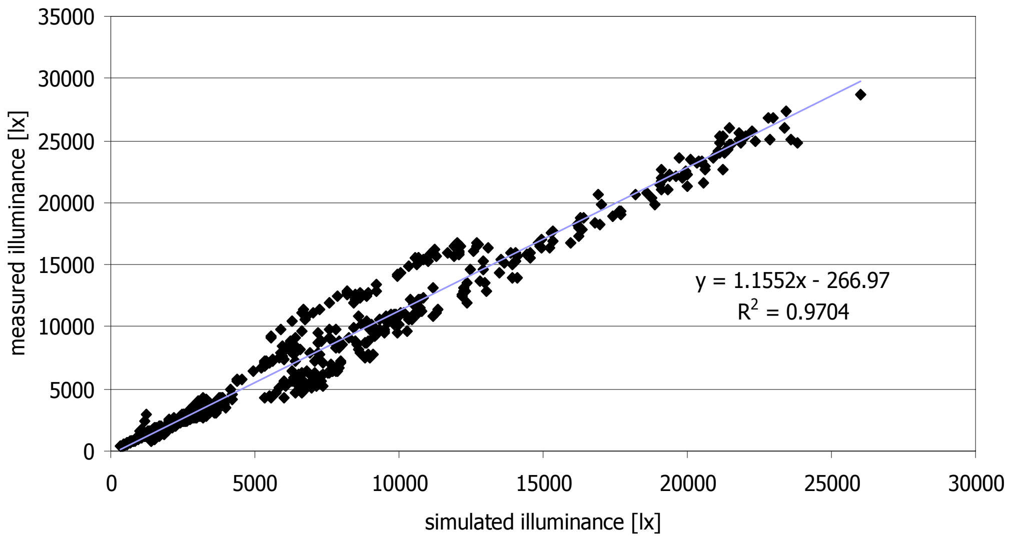

Figure 44 Simulated versus measured indoor illuminance values for P1_south (sky luminance data based on CIE Standard Skies)

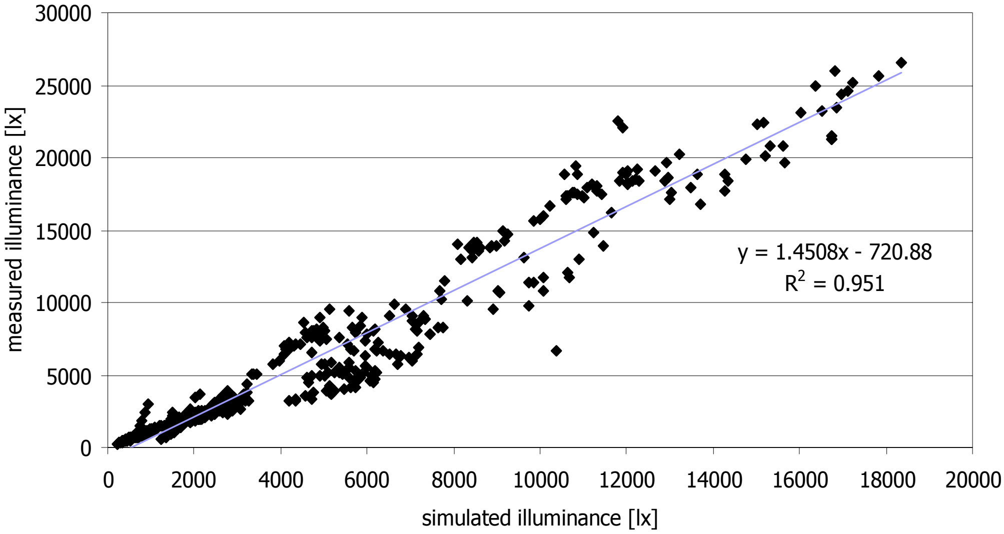

Figure 45 Simulated versus measured indoor illuminance values for P2_south (sky luminance data based on CIE Standard Skies)

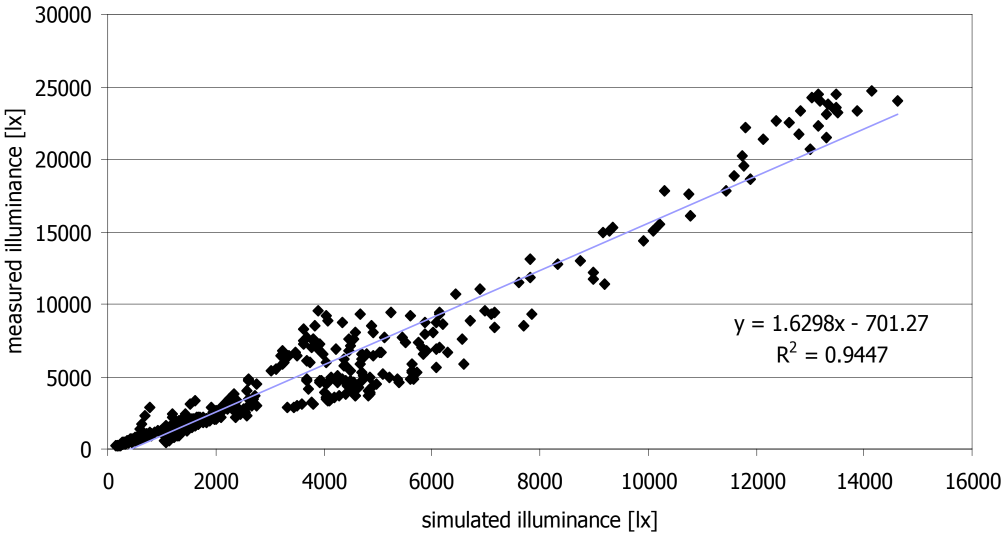

Figure 46 Simulated versus measured indoor illuminance values for P3_south (sky luminance data based on CIE Standard Skies)

3.2.3 Perez All-Weather sky model

The Perez All-Weather sky model was selected as the currently most reliable model and the same simulations were conducted based on it. Figure 47 illustrates the relationship between the simulated illuminance values based on the Perez All-weather sky model (horizontal axis) and the measured indoor illuminance values (vertical axis). The correlation coefficient of this linear regression is 0.89.

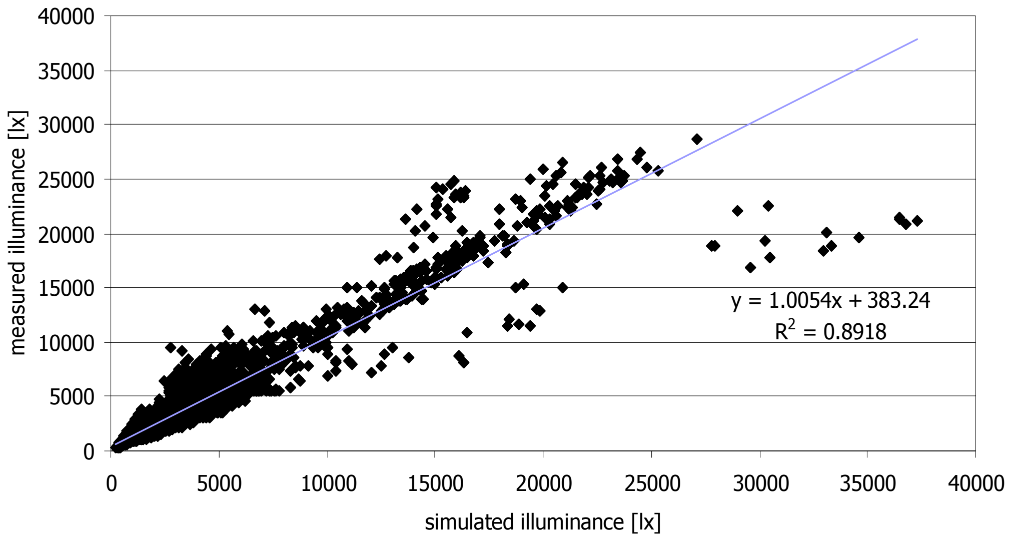

Figure 47 Simulated versus measured indoor illuminance values (sky luminance data based on Perez All-Weather sky model)

The corresponding results from the two sets of simulations are illustrated in the following figures (48-55):

a. The model faces north

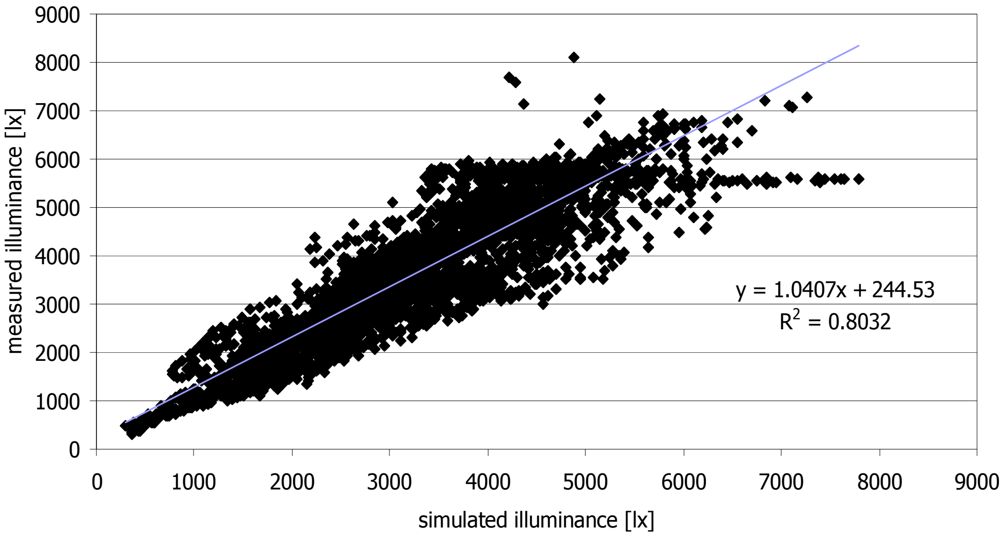

Figure 48 Simulated versus measured indoor illuminance values when the model faces north (sky luminance data based on Perez All-Weather sky model)

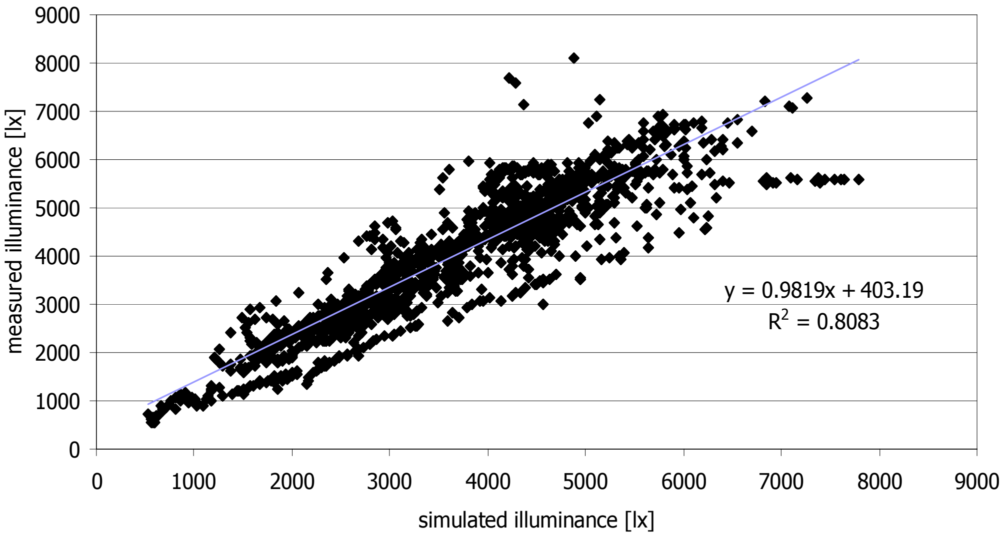

Figure 49 Simulated versus measured indoor illuminance values for P1_north (sky luminance data based on Perez All-Weather sky model)

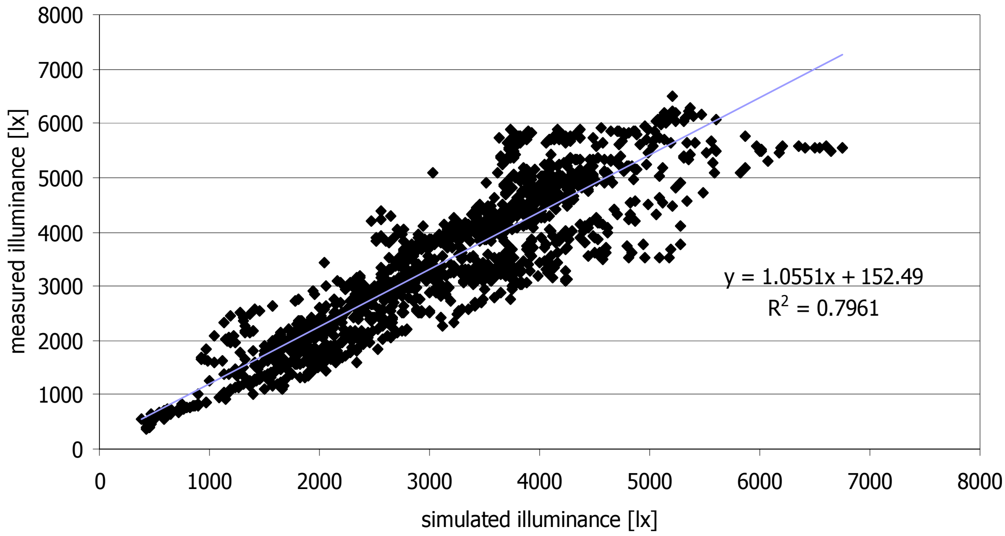

Figure 50 Simulated versus measured indoor illuminance values for P2_north (sky luminance data based on Perez All-Weather sky model)

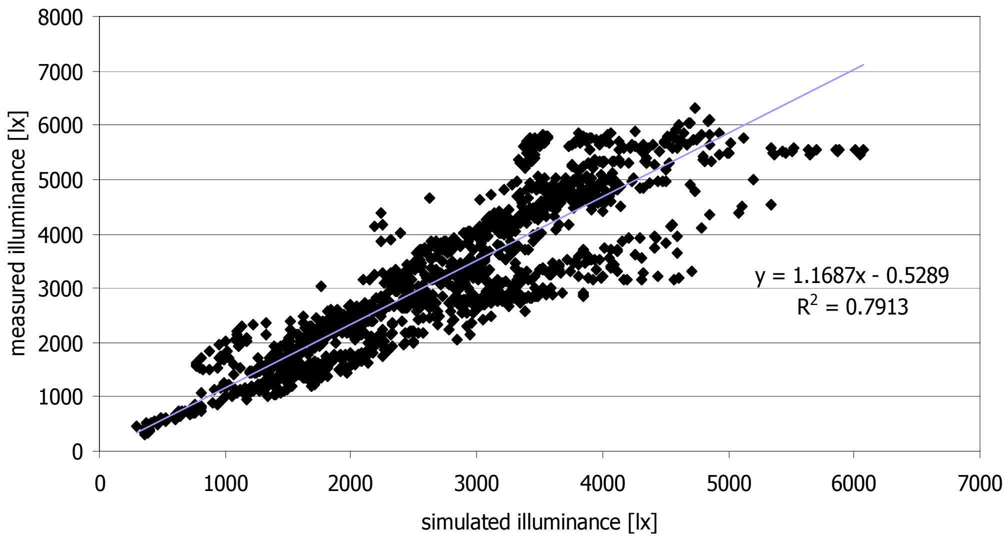

Figure 51 Simulated versus measured indoor illuminance values for P3_north (sky luminance data based on Perez All-Weather sky model)

b. The model faces south

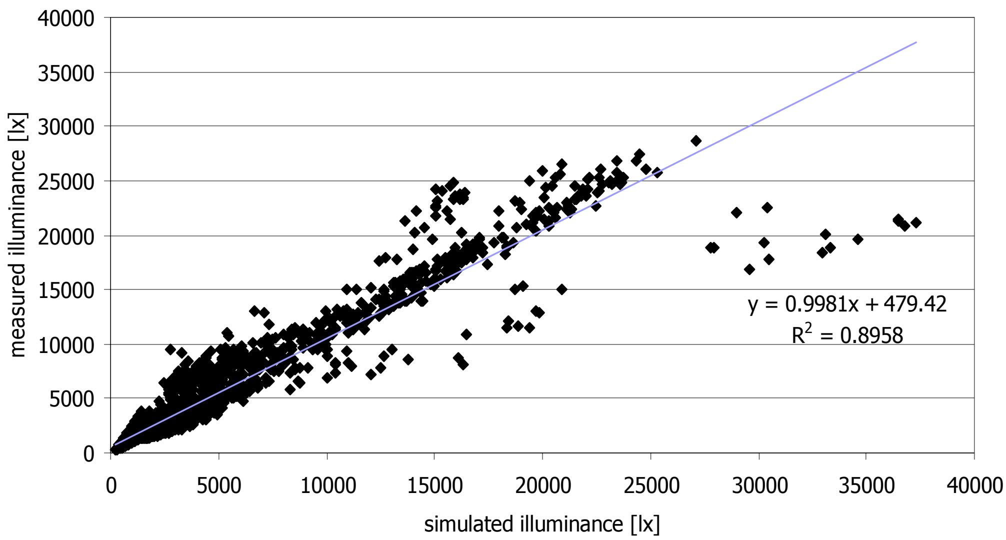

Figure 52 Simulated versus measured indoor illuminance values when the model faces south (sky luminance data based on Perez All-Weather sky model)

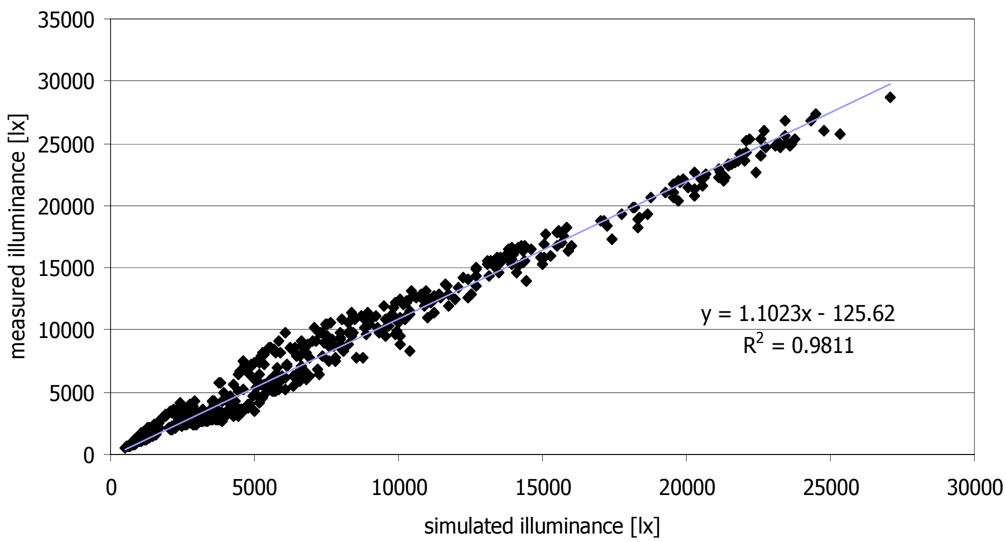

Figure 53 Simulated versus measured indoor illuminance values for P1_south (sky luminance data based on Perez All-Weather sky model)

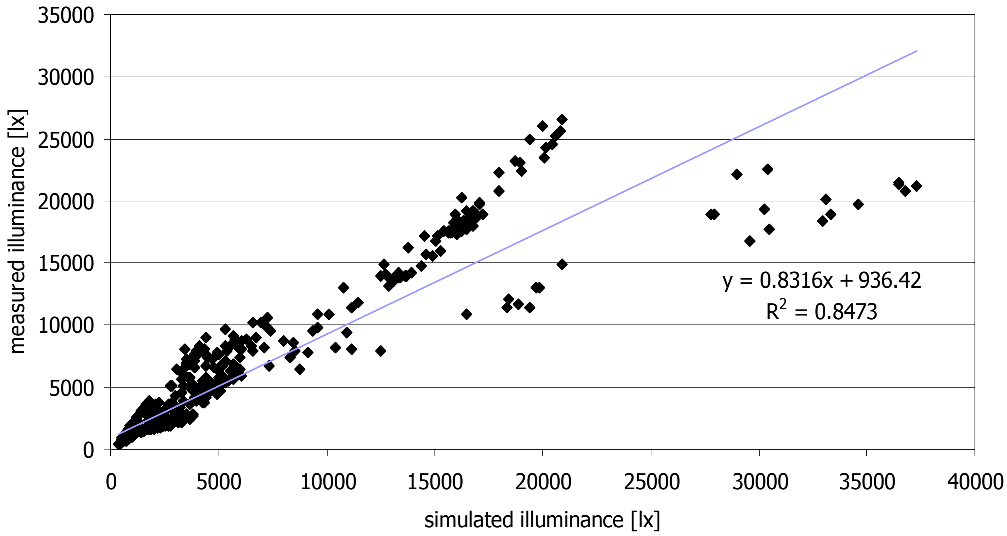

Figure 54 Simulated versus measured indoor illuminance values for P2_south (sky luminance data based on Perez All-Weather sky model)

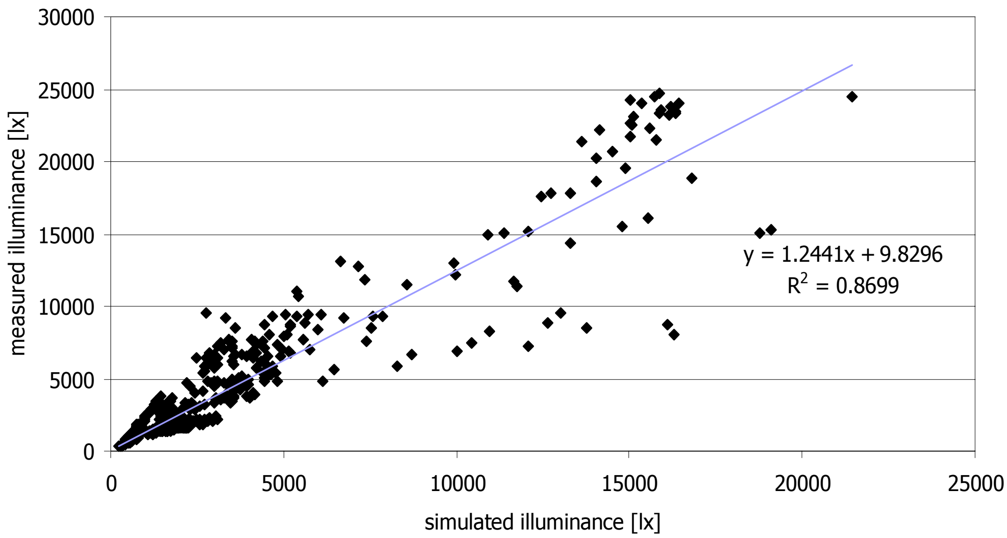

Figure 55 Simulated versus measured indoor illuminance values for P3_south (sky luminance data based on Perez All-Weather sky model)

4. Discussion

4.1 Derivation of sky luminance distribution maps from digital images

In order to explore the potential of using a digital camera with a fish eye converter toward real-time derivation of sky luminance distribution maps, a large number of images were taken in November 2005. Among them, there were images of a great variety of skies; from overcast to completely clear skies.

Sky luminance data derived from those images were compared to the corresponding photometric measurements. The correlation coefficient of the linear regression between the camera-based values and the photometrically measured values is 0.17. As it is shown in Figure 22, the camera-based values are closer to the measured ones when the horizontal illuminance is lower. The difference is greater when the measured values are higher. This means that the error of the camera-based values is greater when the sky is brighter. So a correction is necessary in order to derive reliable sky luminance distribution maps.

Figure 56 illustrates the relationship between the camera-based global illuminance on horizontal plane as it was calculated in RADIANCE (horizontal axis) and the measured global illuminance (vertical axis). This comparison leads to the same observation. There are occasions in which the camera overestimates the luminance of the sky dome, but the great problem is that it underestimates the luminance of the brighter skies.

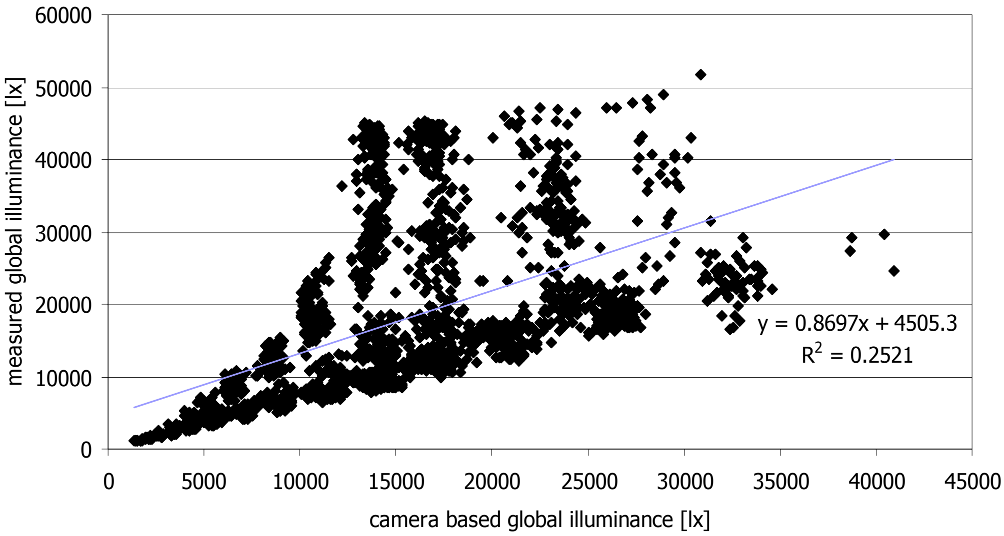

Figure 56 Measured global illuminance versus calculated global illuminance based on digital imaging

As aforementioned, various factors can affect the accuracy of the camera-based horizontal illuminance. There is a need to calibrate the process and the correction methods tested led to the selection of the best sky model derived from the images. So the correction method applied is the "100% to 5 sky patches" (100_5).

When the correction factor of an image for uniform correction is less than 1.1, uniform correction is still followed. This correction factor gives actually an idea of the sky type captured in the image. Figure 57 shows in parallel the global measured value corresponding to each image and the correction factor for uniform correction. It is obvious that in most cases when the correction factor is greater than 1.1, the global illuminance is high. So the sky is intermediate or clear. While when the correction factor is less than 1.1 the sky is mostly cloudy. So in those occasions there is no direct component on the sky dome. When the correction factor is less than 1, in most cases the sky is cloudy too and the camera overestimates its luminance. So we decrease the luminance of the sky patches uniformly.

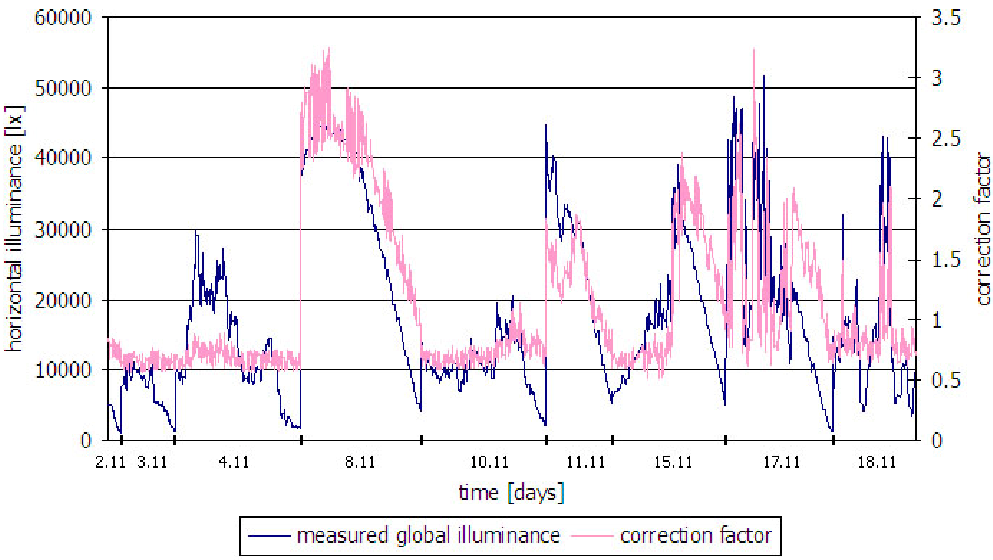

Figure 57 Measured global illuminance and the corresponding correction factor for uniform correction

When the correction factor is more than 1.1, the energy difference between the measured and the calculated global illuminance is distributed to the 5 brighter sky patches. This method of correction is suggested after analysis of the calculated values in RADIANCE. Figure 58 shows that there is a high correlation between the maximum measured value given by the sky monitoring device and the correction factors of the images. So, one can understand that correction is needed when the sky is brighter, but also that the maximum of the 12 values has to be taken into account. In most of these cases, there is direct component in the sky and the sensor that measured the maximum value received light from this brighter part of the sky. This was not detected correctly by the camera. It has to be mentioned that the maximum camera-based value did not exceed 9000 Lux (Figure 22).

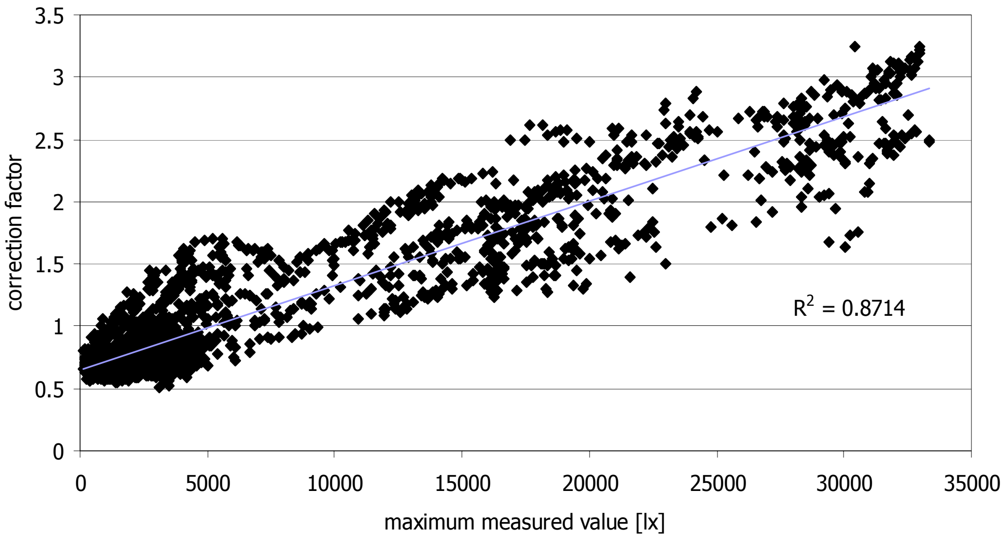

Figure 58 Maximum measured illuminance versus the corresponding correction factor for uniform correction

Figure 59 shows the relationship between:

a. the difference of maximum measured illuminance minus the corresponding calculated illuminance based on digital imaging (horizontal axis)
b. the difference of measured global illuminance minus the calculated global illuminance based on digital imaging (vertical axis)

for all the occasions in which the correction factor for uniform correction is greater than 1.1.

The correlation coefficient of this linear regression is 0.92. Therefore, the luminance that has to be added to the extracted values from the digital images is in most cases almost equal to the difference that has to be added to the illuminance that corresponds to the maximum value. This maximum measured value is due to the luminance of the brightest part of the sky dome. So this is why it is suggested -at the beginning- to increase just the luminance of the brightest sky patch.

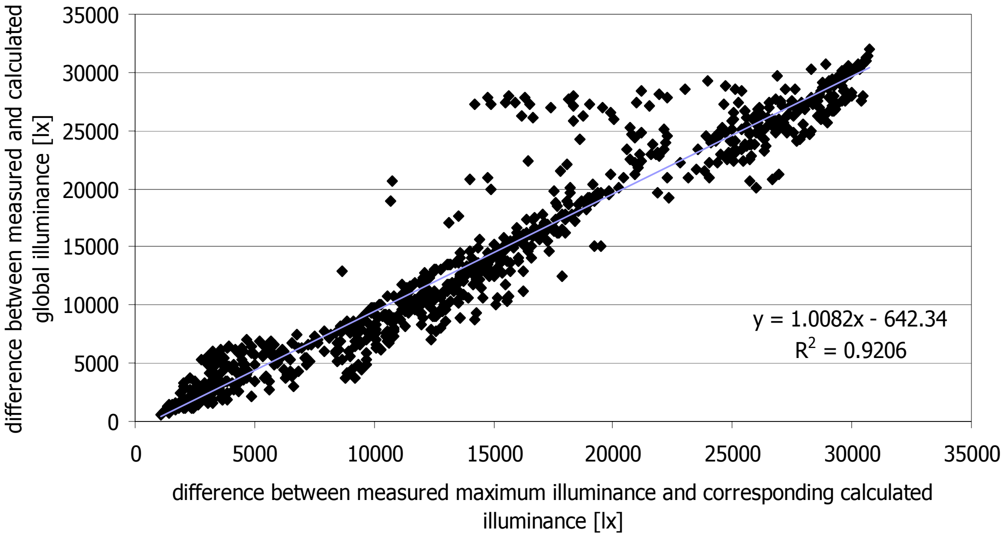

Figure 59 Difference that has to be added to the calculated global illuminance versus the difference that has to added to the illuminance that corresponds to the maximum measured illuminance

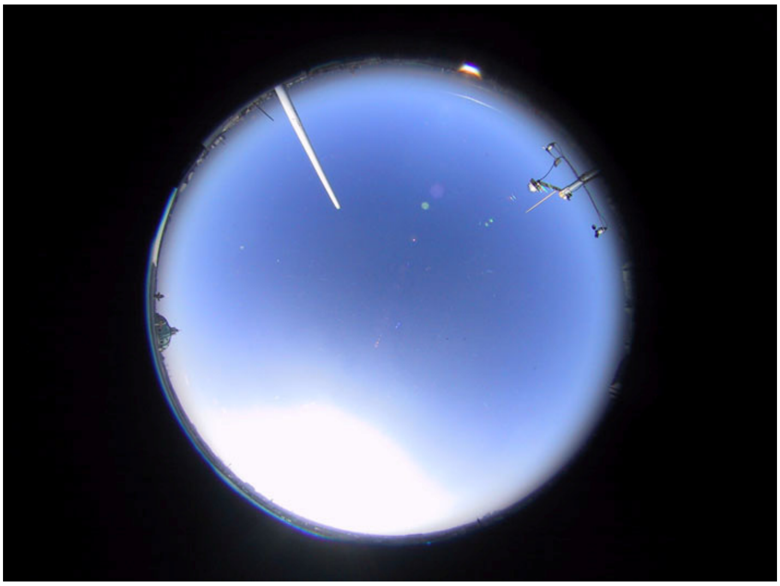

Figure 60 Image of clear sky

Figure 60 is one of the images captured that show a clear sky. Most of the images that have a correction factor greater than 1.1 are similar to this one. As it can be seen, the circumsolar region is rather large and this is the reason why finally it is suggested to increase the luminance values of 5 sky patches.

Figure 61 illustrates the relationship between the maximum measured illuminance and the corresponding camera-based value after "100% to 5 sky patches" correction. The correlation coefficient is 0.96 which is high and shows that the correction method selected gives reliable results.

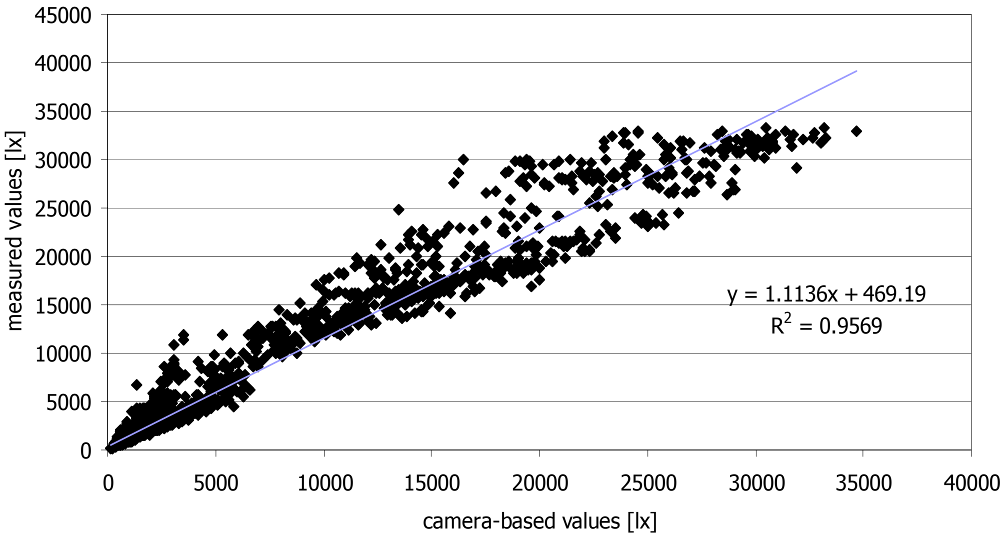

Figure 61 Maximum measured illuminance versus corresponding calculated illuminance after correction

Also, the summary of the results from each correction method shows that this is the most reliable method. Figure 62 illustrates the correlation coefficients of the linear regression between the measured values and the camera-based values for each one of the 12 sensors in the sky monitoring device.

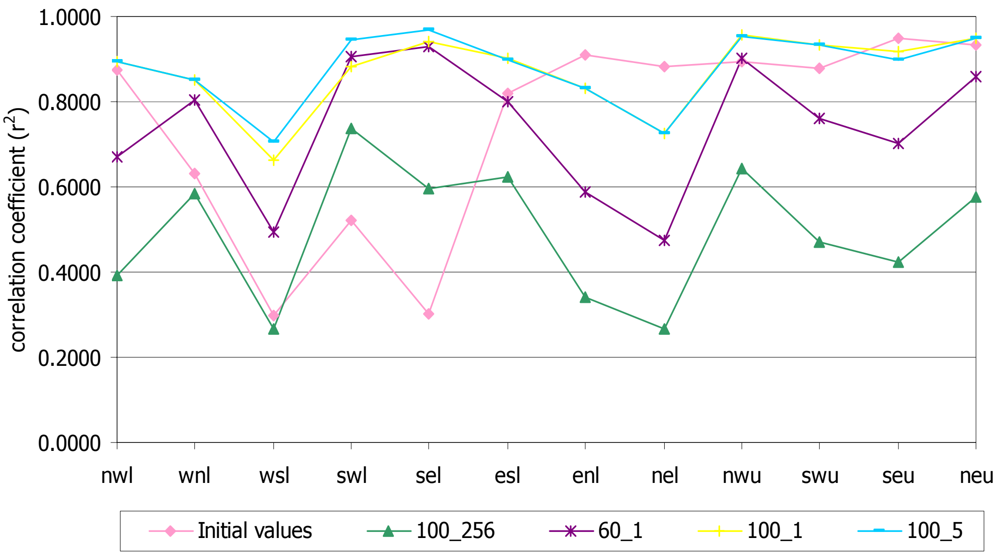

Figure 62 Summary of the results from the correction methods

4.2 Comparison of indoor values for daylight calculated by RADIANCE

Digital images combined with parallel photometric calibration appear to provide a valuable means for a real-time generation of sky luminance maps. This kind of maps can be used as input for lighting simulation programs. They can assist the prediction of indoor light levels for building design and control purposes. To validate the efficiency of this approach, a comparison has been done between the results for indoor daylighting with the use of three different sky models. As test space, the scale model described in the approach was used.

The discussion of the results must be seen in the context of the following limitation: the scale model represents an architectural space. The case studied does not have the exact characteristics of an indoor space. The opening of the model is not a representation of a real window as long as there is no glass. The illuminance levels in a real room are influenced by the material of the windows and its characteristics. However, the comparison between the three models is done under the same conditions and the results can be indicative.

The results that are obtained with the use of sky luminance data based on digital imaging show that this sky model generated can adequately represent efficiently the sky types and predict with high accuracy the indoor illuminance. This sky model performs correctly in both orientations of the scale model. As it can be seen from the comparison of the figures 31-33 and 35-37, this approach performs better for the middle point in the scale model. It overestimates the illuminance levels for the point close to the window while it underestimates the illuminance levels for the point far from the window.

4.2.1 Comparison between digital images and CIE Standard Skies

The sky luminance distribution maps appear to give better results than the CIE Standard Skies. The correlation coefficient of the linear regression between the simulated illuminance values and the measured ones is 0.96 when the sky luminance was based on the digital imaging (Figure 29). The corresponding correlation coefficient for the CIE Standard Skies is 0.74 (Figure 38).

The indoor predictions based on CIE Standard Skies are more reliable when the model faces to the south. These sky models overestimate the indoor illuminance when the model faces north, especially when the sky is clear. This is illustrated in Figure 63, where the measured illuminance levels for the 11th of November and the corresponding values as they were predicted with the use of the two sky models - camera-based and CIE

Standard Skies - are shown. This was a sunny day with clear sky. The comparison shows that the sky luminance maps derived from digital imaging provide results that are closer to the photometrically obtained illuminance levels.

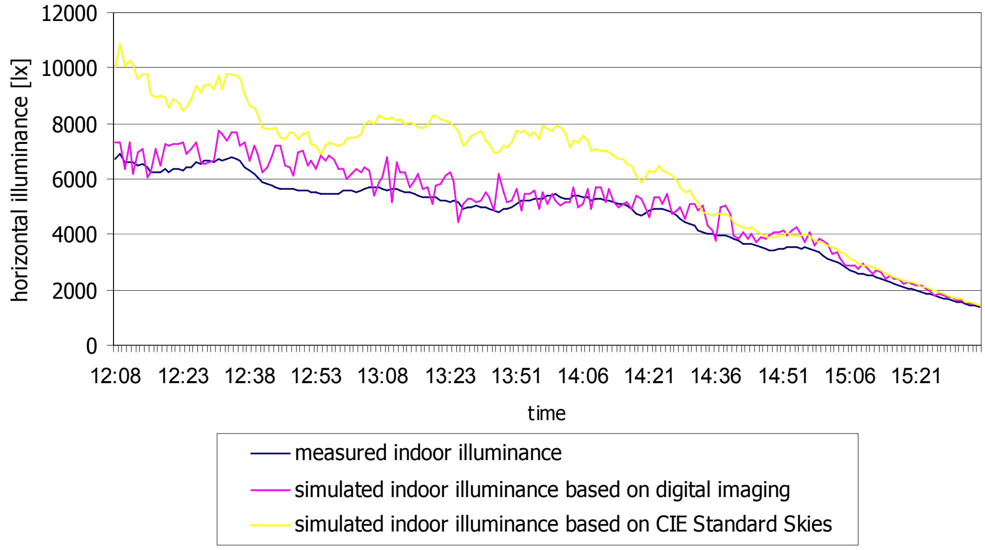

Figure 63 Comparison of the results for the point close to the window on the 11th of November when the model faced to the north

The CIE sky is generated in RADIANCE according to the type of the sky and the global horizontal illuminance given as input. In the overcast sky, the sky brightness increases gradually with altitude from the horizon to the zenith, but it does not vary with azimuth. In the clear sky, one part of the illuminance is distributed as luminance to the circumsolar region and the other part to the rest of the sky. It is a description of a completely clear sky. These two sky models are representations of two extreme sky types. The intermediate sky model describes sky conditions that have greater turbidity than the CIE sky model. For each instance, the most appropriate sky model was selected based on visual inspection of the corresponding image.

The problem is that these three CIE skies available cannot represent a wide range of sky conditions. It is not possible that each one of the above sky models can represent all of the naturally occurring sky brightness distributions. Figures 64-66 show two images shot that have been characterized as intermediate. The luminance distribution is different in those, but this change cannot be detected in the CIE Intermediate Sky. The sky model based on the digital imaging imitates more correctly the real sky and follows the changes of the luminance distribution that occur.

Figure 64   Two images of intermediate sky shot on the 10th of November

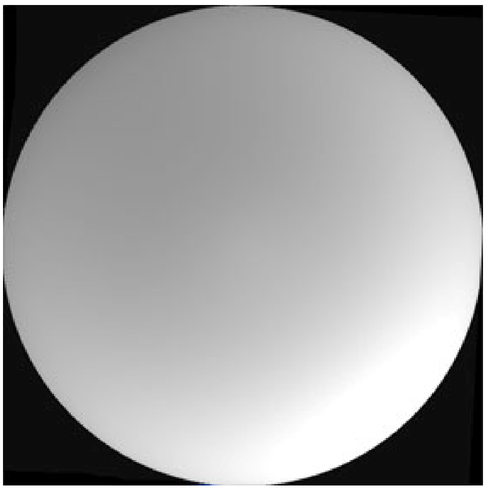

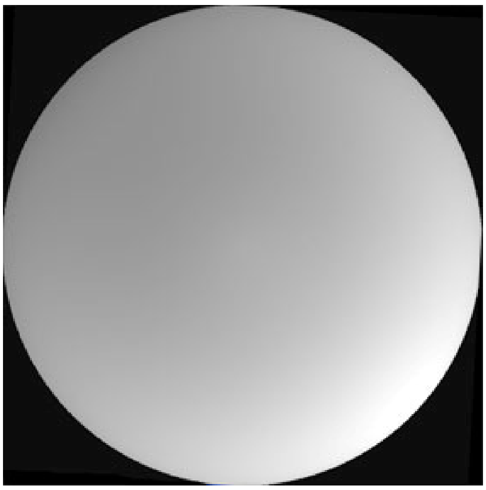

Figure 65   The corresponding CIE Intermediate skies

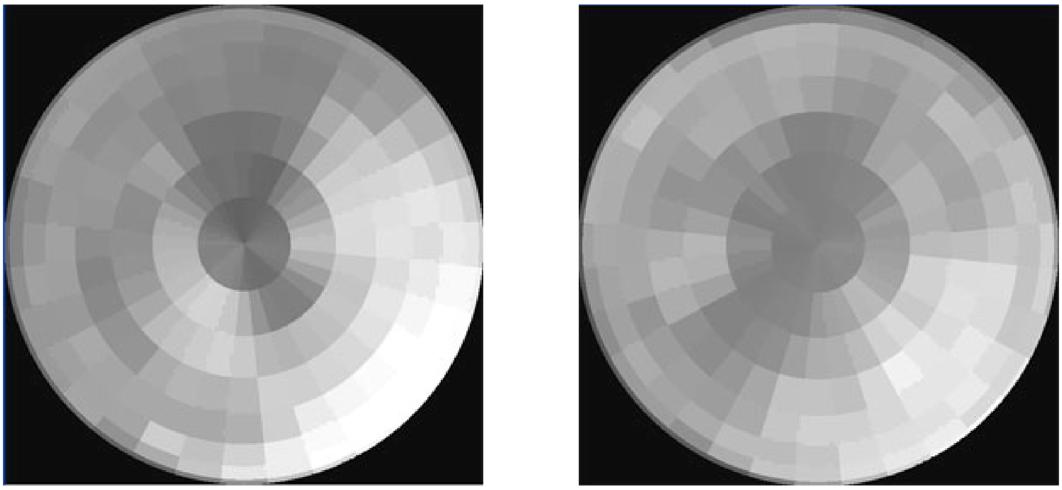

Figure 66 The corresponding calibrated camera-based luminance distribution maps

When the model faces to the north, the sensors measure the illuminance that reaches them from the part of the sky with no direct component. But the values simulated are higher than the measured ones. On the other hand, when the model faces to the south, the simulated values are higher than the measured ones for the point close to the window, but they are significantly lower for the other two points. This means that the sky generated according to the CIE Clear Sky has different distribution of luminance than the real one.

4.2.2 Comparison between digital images and Perez All-weather sky

Definitely, Perez All-weather sky model performs better than the CIE Standard Skies. But the sky model based on digital imaging is still proved to be more reliable. The correlation coefficient of the linear regression between the simulated illuminance values and the measured ones is 0.96 when the sky luminance was based on the digital imaging (Figure 29). The corresponding correlation coefficient for the Perez All-weather sky is 0.89 (Figure 47).

The Perez All-weather sky model can give quite reliable results for both orientations of the model. The major problem can be observed in occasions of sunny skies and it is the overestimation of the illuminance levels at the middle point and the point far from the window in the scale model when it faces to the south. This can be interpreted by the way the sky is generated in RADIANCE. All the direct luminance is added to the sun source which is represented as a disk. So the source is very bright while the circumsolar region is not modeled as it really is. During the period of the measurements, the sun altitude was low (up to 23^{o}). This means that the bright source generated can easily increase the illuminance reaching those two points while in the reality this was not the case.

Figure 67 shows in comparison the measured illuminance levels and the simulated ones for the middle point in the scale model on the 17th of November when it was facing to the south.

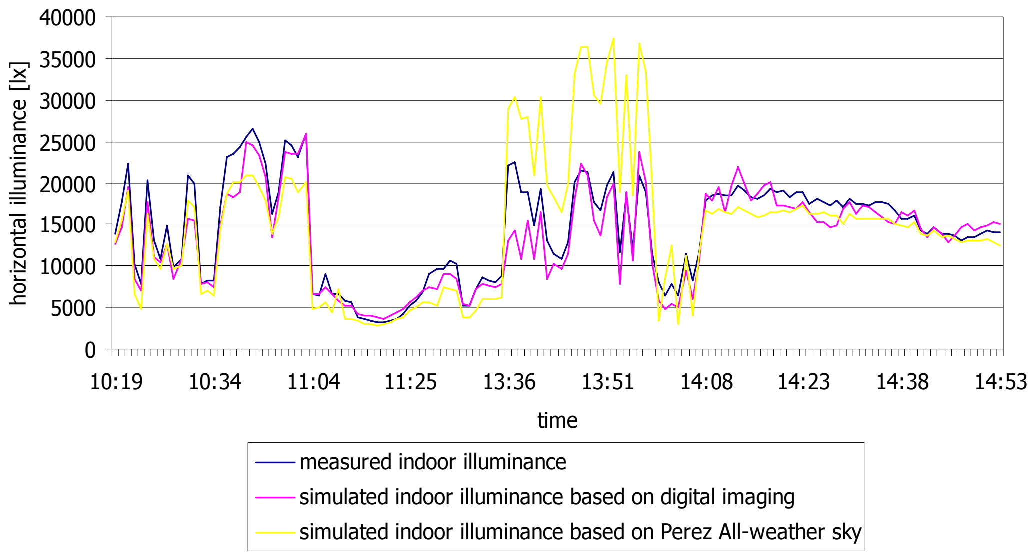

Figure 67 Comparison of the results for the middle point on the 17th of November when the model faced to the south

Figure 68 shows one of the images shot on this day and Figures 69-70 show the corresponding skies generated by RADIANCE based on digital imaging and the Perez All-weather sky. The difference between the luminance distribution is illustrated; how the Perez All-weather sky model adds the whole direct luminance to the sun source and the circumsolar region is darker.

Figure 68 An image of clear sky shot on the 17th of November

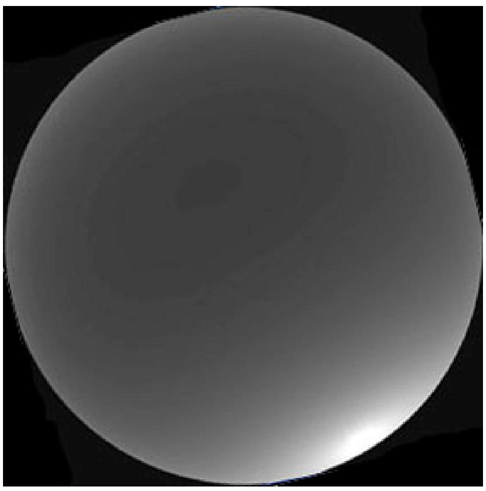

Figure 69 The corresponding sky generated based on Perez All-weather sky

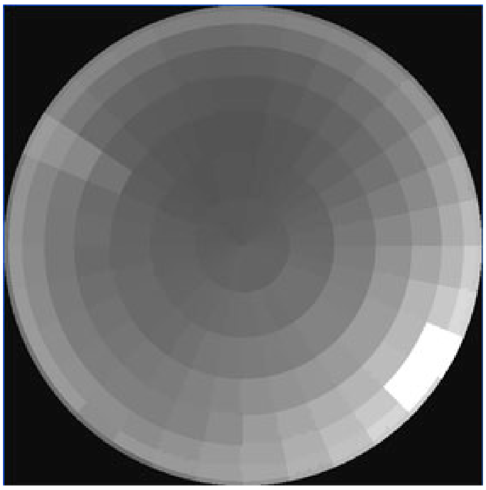

Figure 70 The corresponding camera-based luminance distribution map

4.2.3 Comparative results of the three sky models

Figures 71-73 illustrate comparative results for three sky types - overcast, intermediate and completely clear - when the model was facing to the north. Figures 74-76 show comparative results for the same sky types, when the model was facing to the south. All the results refer to the illuminance that reaches the point close to the window (P1).

a. Model facing to the north

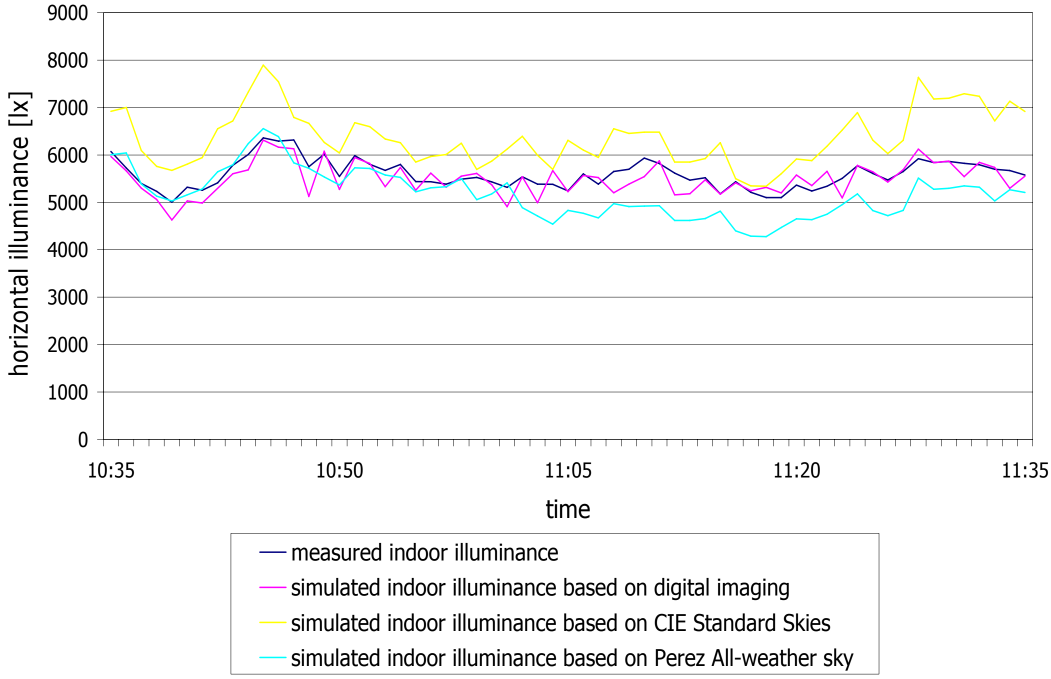

Figure 71 Comparison of the results for overcast sky (north)

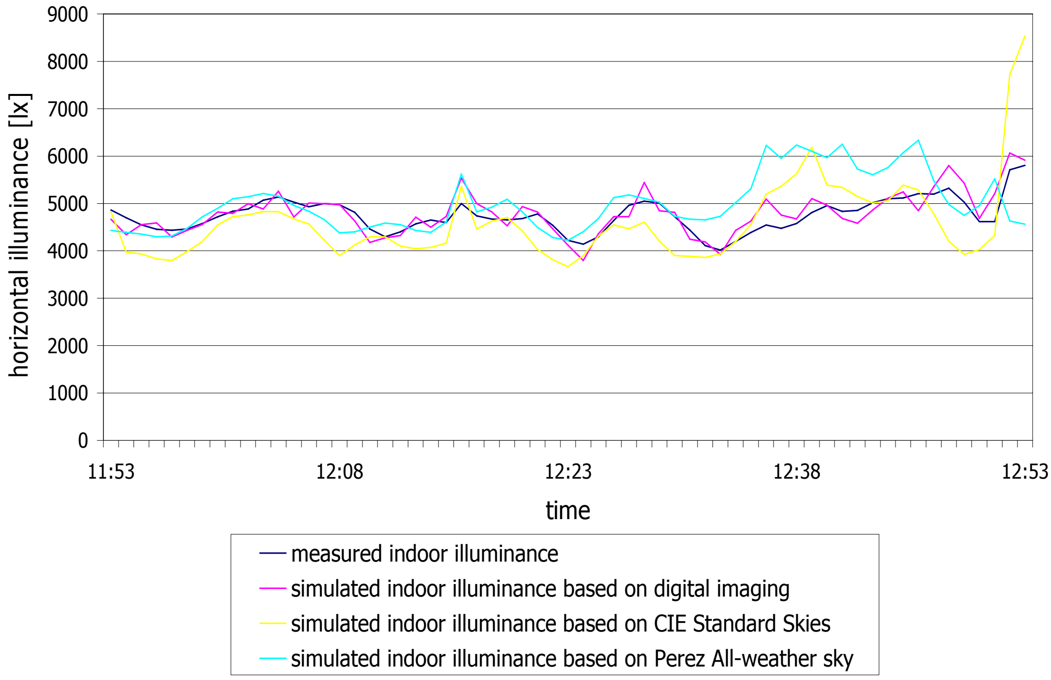

Figure 72 Comparison of the results for intermediate sky (north)

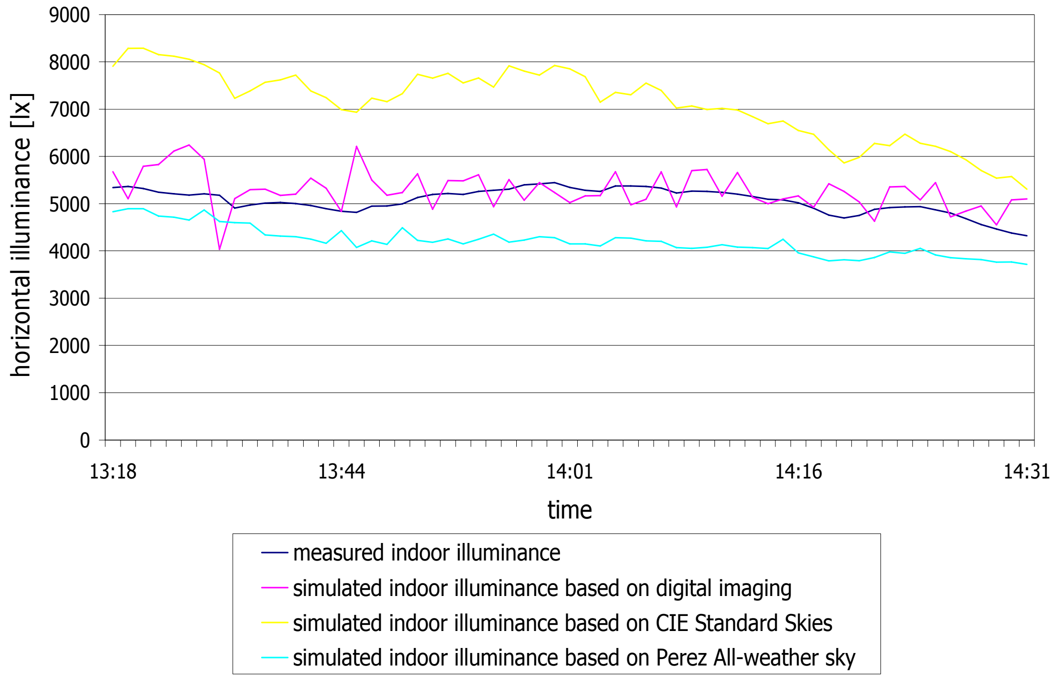

Figure 73 Comparison of the results for clear sky (north)

The results show that the camera-based sky model performs in all the occasions better than the other sky models. This is more obvious for the sunny skies.

b. Model facing to the south

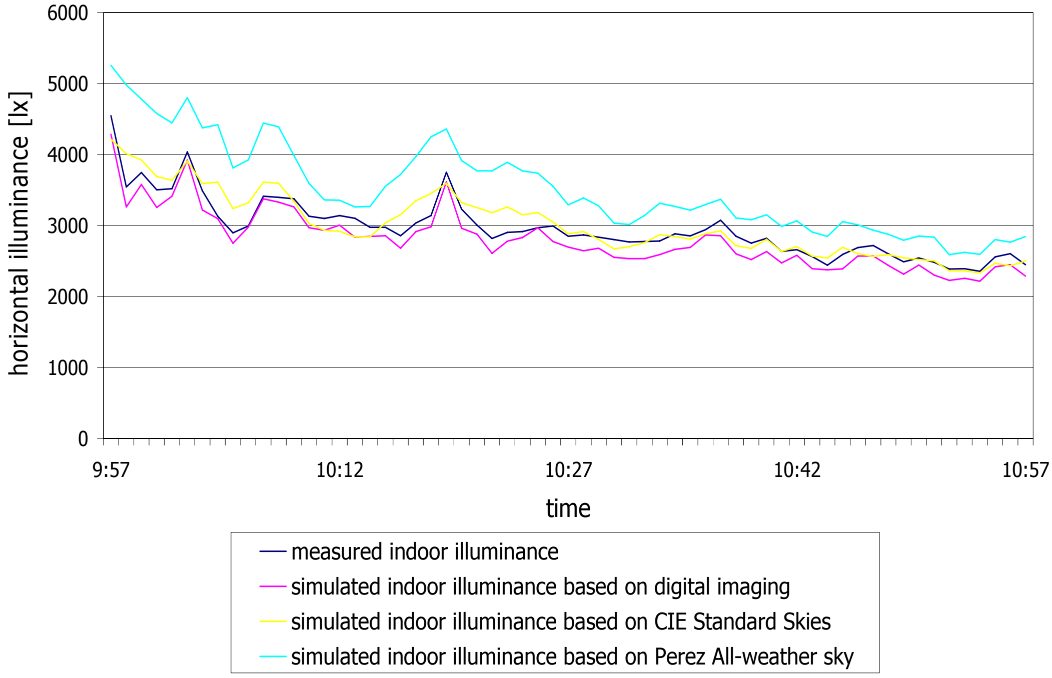

Figure 74 Comparison of the results for overcast sky (south)

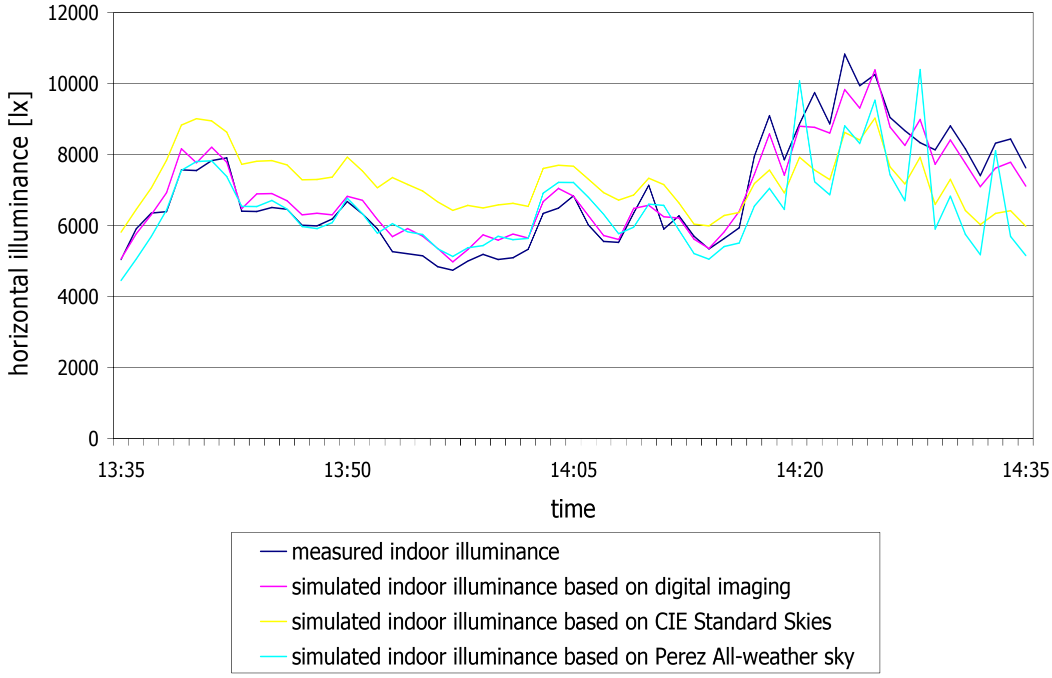

Figure 75 Comparison of the results for intermediate sky (south)

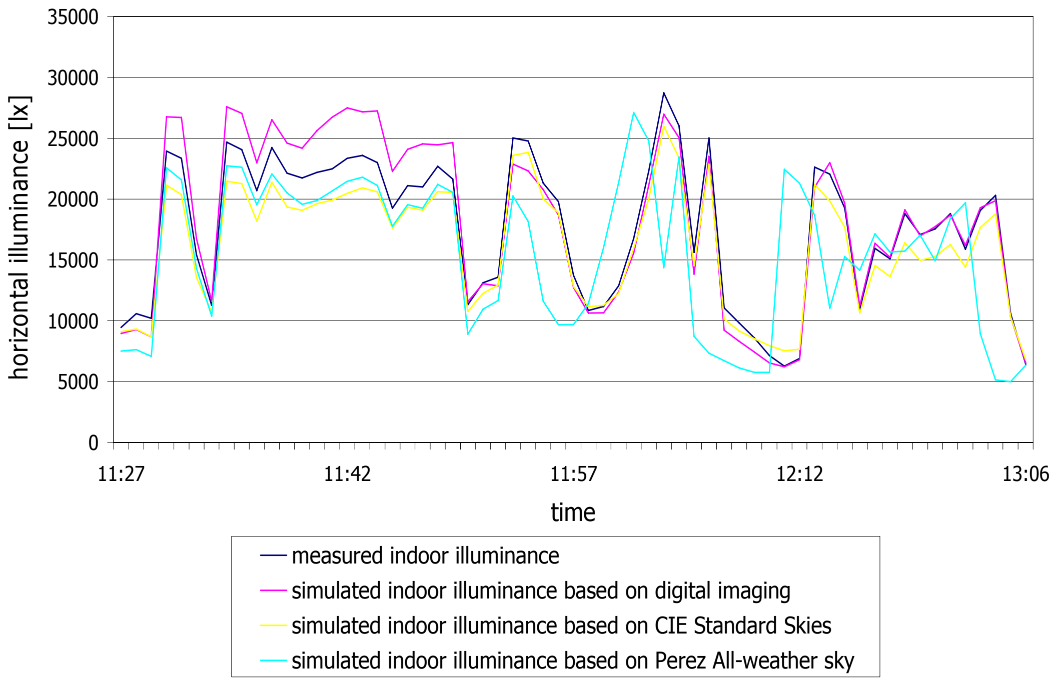

Figure 76 Comparison of the results for clear sky (south)

The results show again that the camera-based sky model predicts more accurately the indoor illuminance levels under all sky conditions. Only in the occasions of very bright skies, the values are overestimated while the values from the other two sky models are underestimated.

Figures 77-79 illustrate the percentage of the values according to the relative error for each one of the sky models. Figure 77 corresponds to the camera-based sky model, Figure 78 to the CIE Standard Skies and Figure 79 to the Perez All-weather sky. The relative error is calculated according to the following formula:

$$RE = \frac{|E_{sim} - E_{meas}|}{E_{meas}} \qquad \text{Eq.17}$$

where:

E_{sim} simulated indoor illuminance based on a sky model

E_{meas} measured indoor illuminance

One can see that about 90% of the illuminance values predicted with the camera-based sky model have a relative error up to 20%. This demonstrates the potential of this approach. With the use of CIE Standard Skies, only 58% of the results have a relative error up to 20%, while the 90% of the results have a relative error up to 70%. With the use of the Perez All-weather sky, 67% of the results have a relative error up to 20% and 90% of the results have up to 35% relative error.

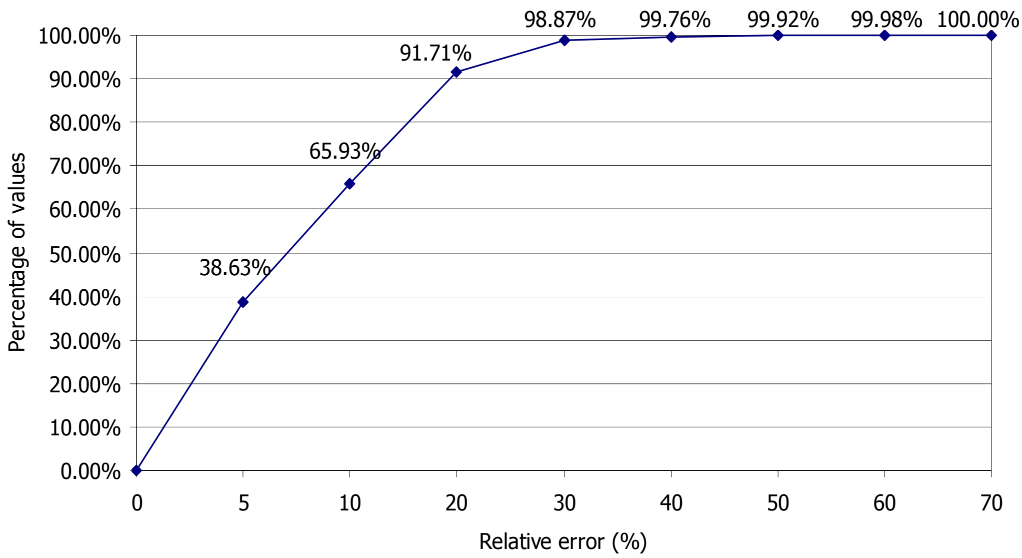

Figure 77 Relative errors and distribution of the values for the camera-based sky model

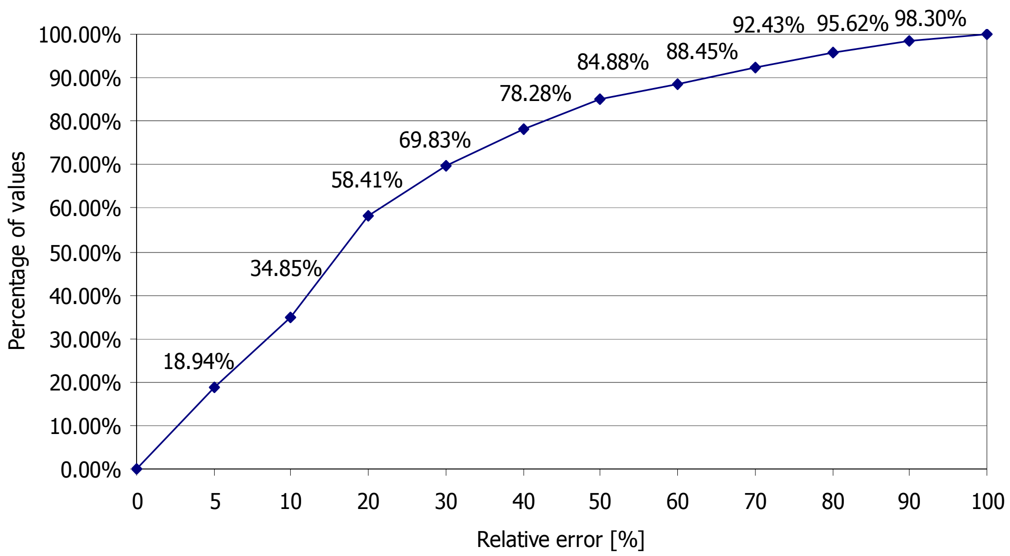

Figure 78 Relative errors and distribution of the values for the CIE Standard Skies

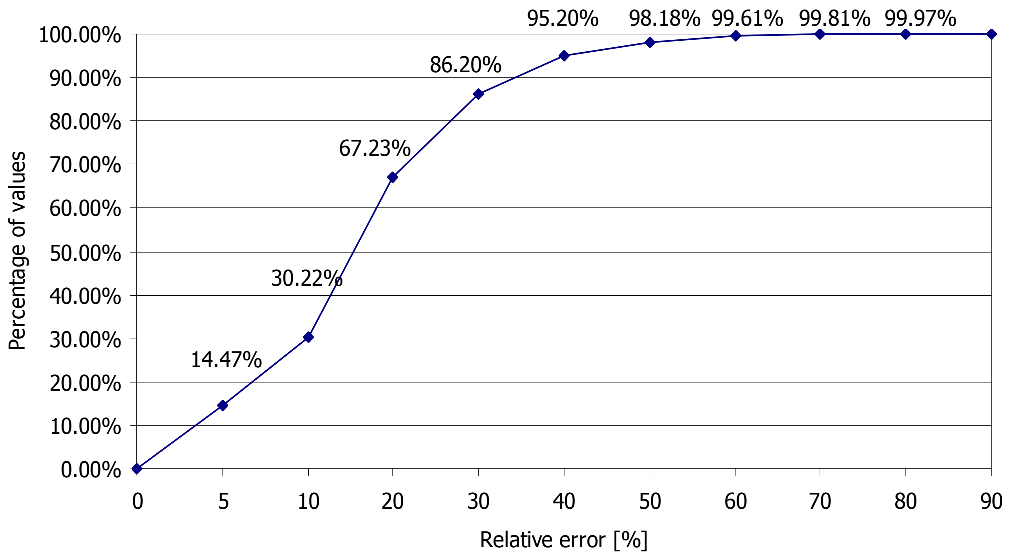

Figure 79 Relative errors and distribution of the values for the Perez All-weather sky

Figure 80 shows in comparison the relative errors and the distribution of the simulated values obtained with the use of the three sky models. It is demonstrated that the camera-based sky model gives more reliable results. Almost all the values have a relative error that does not exceeds 30% while this is not the case with the other two sky models. Digital imaging can be adequately used for the prediction of indoor illuminance levels.

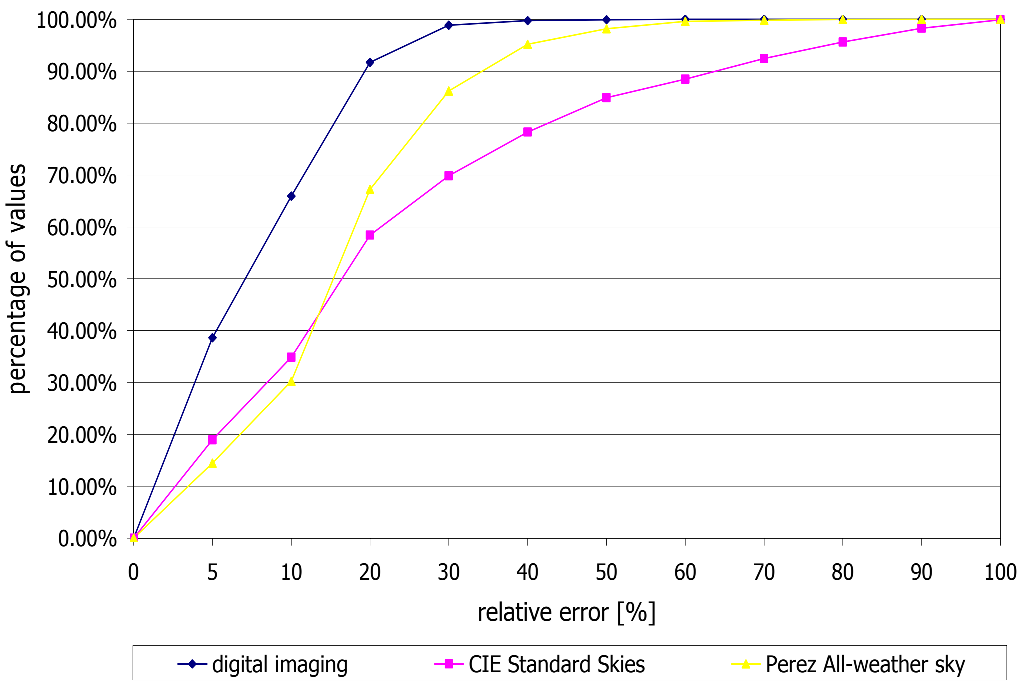

Figure 80 Comparison of the relative errors and distribution of the values for the three sky models used

5. Conclusion

5.1 Contribution

The results of this research demonstrate that digital imaging calibrated with parallel photometric measurements of overall horizontal illuminance levels can provide an efficient basis for the generation of detailed sky luminance models. A procedure is described here for real-time derivation of those maps that can be completed in a short time and with relatively low cost.

These sky luminance models can be used as input in lighting simulation programs. The application of such models can increase the predictive accuracy of the computational prediction tools.

Accurate simulation of the quantity and distribution of daylight in an architectural space is a great concern during the design phase. The collection of images over a statistically representative period of time can provide sky models that can be stored for long term use.

Moreover, such luminance maps can increase the reliability of daylight simulation toward supporting the design and operation of daylighting systems in sentient buildings (Mahdavi 2005). To make effective use of the advances of information technology for building automation applications, high quality models of buildings are needed. Such models must consider that apart from the building’s components and systems, also its environment goes through multiple changes throughout its life-cycle. In this context, real-time recording of the sky conditions is necessary. The changes of daylight availability can determine the control of the lighting systems, but also the control of the blinds and generally can define the indoor climate conditions in combination with other data.

5.2 Future research

An attempt to derive luminance information from digital imaging has been done. The research has shown that those images need correction with the aid of parallel measurements of horizontal illuminance levels. In future, the same procedure could be followed with the objective to capture images that will provide more accurate luminance values. Towards this end, a pattern with more sky patches could be introduced.

In addition, the sky monitoring device that was used can be changed. The sky dome can be divided in more sectors and more sensors can be used for the measurement of the horizontal illuminance levels. So the calibration of the camera-based values can be done with more accuracy.

It is also very important to repeat the same measurements during other months of the year to detect the potential of this approach with different sky conditions. The data collected during this research concerned autumn skies with low global horizontal illuminance level and low solar altitude. The sky models derived and calibrated can provide accurate predictions of daylighting. However, the initial camera-based values demonstrated that the correction was essential especially for sunny skies. It is thus necessary to test if this approach is still fully valid when the luminance of the sky is much higher.

If this research is repeated during other months and over a longer period of time, information can be stored about the general sky conditions in

Vienna, Austria and this database can be used for several purposes concerning architectural design and building simulations.

6. References

Chromaticity Diagrams. 2006. http://www.efg2.com/Lab/Graphics/Colors/Chromaticity.htm. May 2006.

CIE colorspace. 2006. http://en.wikipedia.org/wiki/CIE_1931_color_space (last visited May 2006).

Clear. 2006. http://www.learn.londonmet.ac.uk/packages/clear/visual/. March 2006.

Darula S. and Kittler R. 2002. *CIE Sky Standard defining luminance distributions*. Proceedings of eSim, September 2002.

Davis, G.B., Griggs, D.J., Sullivan, G.D. 1992. *Automatic Estimation of Cloud Amount Using Computer Vision.* Journal of Atmospheric and Oceanic Technology, Vol. 9, February: pp. 81-85.

Digital Cameras. 2006. http://www.digicamhelp.com/advanced-digital-camera-settings. May 2006.

Digital Imaging. 2006. http://swehscpharmacy.arizona.edu/exppath/micro/digimageintro.html. May 2006.

Fisheye. 2006. http://en.wikipedia.org/wiki/Fisheye_lens (last visited May 2006).

Janak, M. 1997. *Coupling building energy and lighting simulation.* Proceedings of the 5th International IBPSA Conference. Prague. September 1997: pp. 313-319.

Igawa, N., Nakamura, H., Matsuura, K. 1999. *Sky luminance distribution model for simulation of daylit environment.* Proceedings of IBPSA Conference. Volume 2: pp.969-975.

LabView. 2006. http://en.wikipedia.org/wiki/LabView (last visited May 2006).

Lam, K.P., Mahdavi, A., Ullah, M.B., Ng, E., Pal, V. 1997. *The implications of sky model selection for the prediction of daylight distribution in architectural spaces.* 5th International IBPSA Conference. Prague. September 1997. Vol. I: pp. 339-345.

Larson, G. W., and Shakespeare, R. 1998. *Rendering with Radiance.* Morgan Kaufmann, California.

Littlefair, P. J. 1994. *A Comparison of Sky Luminance Models with Measured Data from Garston, United Kingdom.* Solar Energy, Vol.53, No.4, 1994: pp 315-322.

Mahdavi A. 2005. *Space, Time, Mind: Toward an Architecture of Sentient Buildings.* Computer Aided Architectural Design Futures 2005. Proceedings of the 10th International Conference on Computer Aided Architectural Design Futures. ISBN 1-4020-3460-1. Vienna, Austria. 20–22 June 2005: pp. 23-40.

Mahdavi, A., Chang, S., Pal, V. 1999. *Simulation based integration of contextual forces into building systems control.* Proceedings of 6th International IBPSA Conference. Kyoto, Japan. Vol. I. ISBN 4-931416-01-2. pp. 193 – 199.

Pal, V., Mahdavi, A. 1999. *A comprehensive approach to modeling and evaluating the visual environment in buildings*. Proceedings of 6th International IBPSA Conference. Kyoto, Japan. Vol. II. ISBN 4-931416-02-0. pp. 579 – 586.

Perez, R., Seals, R., Michalsky, J. 1993. *An all-weather model for sky luminance distribution –preliminary configuration and validation.* Solar Energy, Vol.50, No. 3: pp. 235-245.

Radiance. 2006. *The RADIANCE 3.5 Syhthetic Imaging System.* http://radsite.lbl.gov/radiance/refer.ray.html. (last visited May 2006)

Radiance rendering. 2006. *Rendering with RADIANCE: A Practical Tool for Global Illumination.* ACM Siggraph '98 Course #33, Orlando, FL. July 21, 1998. http://radsite.lbl.gov/radiance/refer/598c33.pdf (last visited May 2006)

Roy, G.G., Hayman, S., Julian, W. 1998. *Sky Modeling from Digital Imagery*. Arc Project A89530177, Final Report. The University of Sydney, Murdoch University, Australia.

Roy, G.G., Ruck, N., Reid, G., Winkelmann, F.C., Julian, W. 1995. *The Development of Modelling Strategies for Whole Sky Spectrums under Real*

Conditions for International Use. ARC Project A89131897, Final Report. The University of Sydney, Murdoch University, Australia.

Ruck, N., Roy, G.G., Reid, G. 1993. *Modeling the Sky – A Standard Digital Form.* Proceedings of the 3rd International IBPSA Conference. Adelaide, Australia. August 1993: pp. 525-531.

Shields, J. 1998. *Whole Sky Imager Theoretical Discussion*. http://www-mpl.ucsd.edu/people/jshields/index.html, Marine Physical Laboratory, Scripps Institution of Oceanography, University of California, San Diego.

Spasojevic, B. and Mahdavi, A. 2005. *Sky luminance mapping for the computational daylight modeling.* Proceedings of the 9th International IBPSA Conference. Montreal, Canada. August 2005. I. Beausoleil-Morrison, M. Bernier (Hrg.); International Conference: IBPSA, 2005, S. 1163 - 1169.
Vartiainen E. 2000. "A new approach to estimating the diffuse irradiance on inclined surfaces". Renewable Energy. Vol. 20: pp. 45-64.

Vartiainen E. 2000. *Daylight modelling with the simulation tool DeLight.* Helsinki University of Technology, Department of Engineering Physics and Mathematics. Report TKK-F-A799, 2000.

Ward, Gregory J. 1994. *The RADIANCE Simulation and Rendering System.* Computer Graphics (Proceedings of '94 SIGGRAPH conference). July 1994: pp. 459-72.

Appendix

Appendix A: Projection of 12 sky sectors on a fisheye image

The distortion, occurring in the fisheye images, is caused by the equidistant transformation within the fisheye lens: the ratio of the angular distance of a point on the sky dome from the zenith to the altitude of the zenith (90^o) corresponds to the ratio of the radial distance of the point's horizontal projection from the centre of the fisheye image to the image radius:

$$\frac{Z}{90^\circ} = \frac{l}{r} \qquad \text{Eq. A1}$$

where:

Z angular distance of a point on the sky dome from the zenith
l radial distance of the point's horizontal projection from the center of the fisheye image
r image radius

Using this basic principle, the twelve sectors of the sky hemisphere, which affect the respective illuminance sensors within the sky monitoring device, can be mapped onto the corresponding sectors in the JPG images (Figures A.1 and A.2).

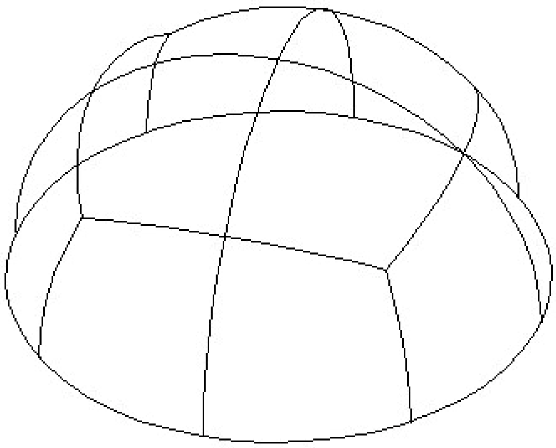

Figure A.1 The twelve sectors of the sky dome

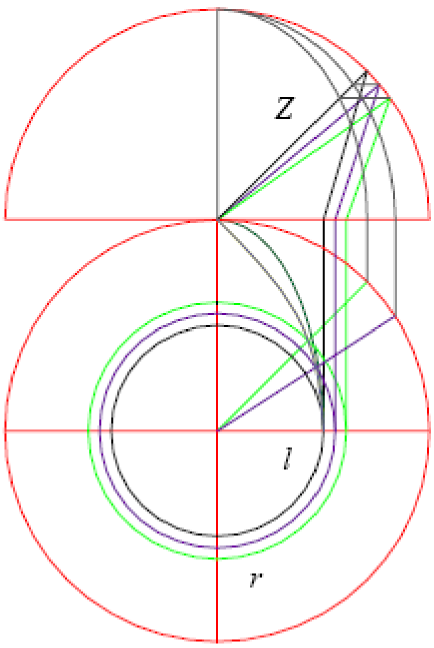

Figure A.2 Equidistant transformation

Appendix B: RADIANCE

RADIANCE was developed as a research tool for predicting the distribution of visible radiation in illuminated spaces. It takes as input a three-dimensional geometric model of the physical environment and produces realistic images from a simple description. RADIANCE has a wide range of applications in graphic arts, lighting design, computer-aided engineering and architecture (Radiance 2006).

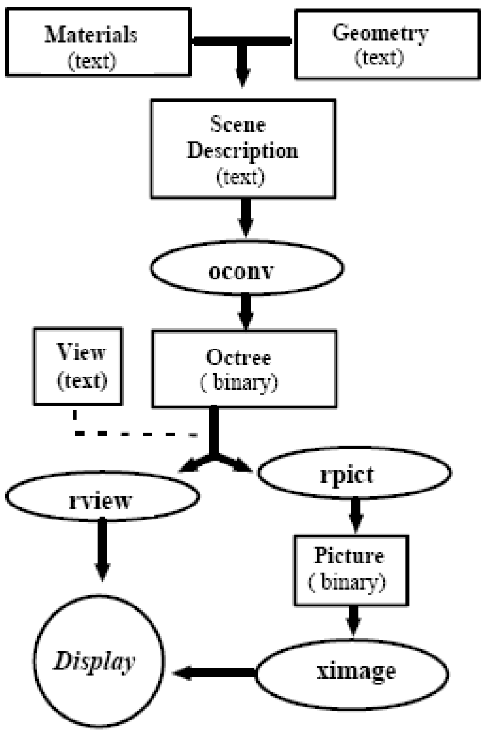

Figure B.1 Flow between programs (ellipses) and data (ovals)
(Radiance Rendering 2006)

RADIANCE consists of over 50 programs, many of which cannot be found anywhere else and have a lot of possibilities. In Figure B.1, the flow between the programs and data is demonstrated during the procedure of the image making. The ellipses represent a few of the programs that are part of the RADIANCE suite. The process begins by defining the materials and the geometry which are then assembled into a scene. The oconv program compiles the scene data into an octree. In general practice, rview is used to interactively view a low quality picture or rpict is used to render a higher quality image which is stored as a RADIANCE picture. Ximage enables the viewing of such pictures (Radiance rendering 2006).

B.1 Scene description

Scene geometry within the rendering programs is modeled using boundary representation of three basic surface classes. These are: polygon (an n-sided planar polygon), sphere and cone. Each surface primitive is independent in the sense that there is no sharing of vertices or other geometric information between primitives.

Materials have to be assigned to the objects of the scene. A material defines the way light interacts with a surface. The basic types are given in the table B.1. Most of them are described by their RGB reflectance. One of the basic materials is plastic. It is used for most of the surfaces in a scene. It is a two-sided material and is also defined by its fraction of specularity and its roughness value. Some of the materials are used for the description of the light sources in the scene (Radiance rendering 2006).

Table B.1 Basic types of materials in RADIANCE

Type of material	Type of representation
plastic	Material with uncolored highlights
metal	Surfaces similar to plastic but modify the color of highlights
light	Self-luminous surfaces (i.e. light sources)

Table B.1 (continued) Basic types of materials in RADIANCE

Type of material	Type of representation
illum	Secondary light sources with broad distributions
glow	Self-luminous surfaces, but limited in their effect
spotlight	Self-luminous surfaces with directed output
mirror	Planar surfaces that produce secondary source reflections
glass	Transparent material that refracts light as well as reflects it. Optimized for thin glass surfaces
trans	Translucent material similar to plastic

Apart from the light sources, a sky description completes the scene. The gensky program generates a description of a clear, intermediate, overcast or uniform sky (CIE skies). Gendaylit is the program that generates a sky according to the Perez All-weather sky model.

B.2 Daylight simulation

The primary goal of daylighting analysis is the reliable evaluation of the potential of a design to provide useful levels of natural illumination. The rtrace program is used for the calculation of horizontal illuminance levels. The only light source used for the daylight simulation is the sky. The basic components that influence the daylight prediction are the values of global and diffuse irradiance (Figure B.2).

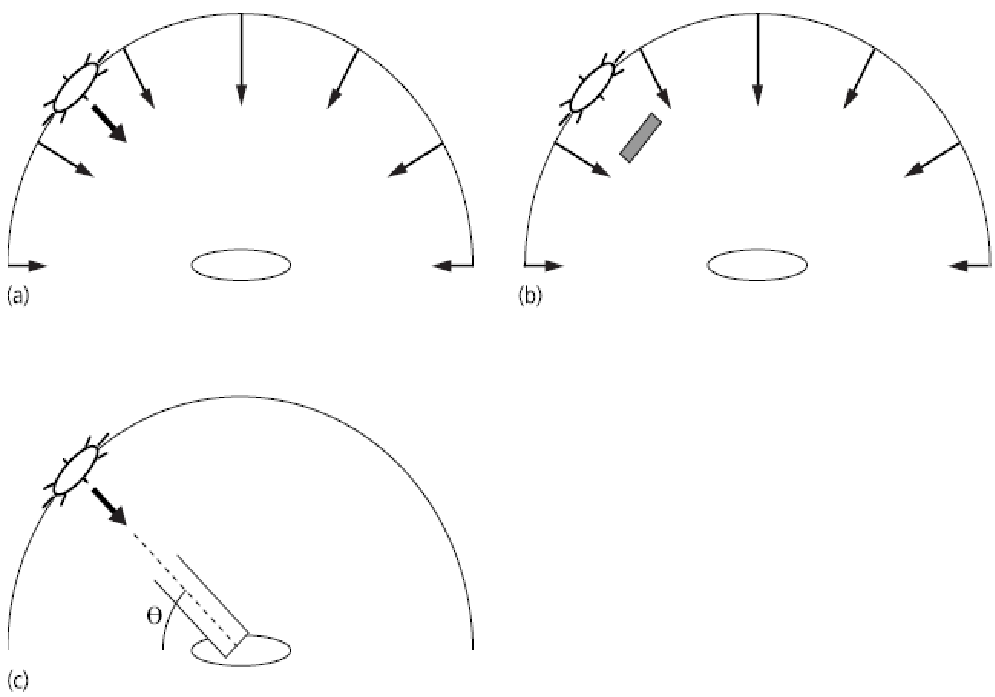

Figure B.2 Basic daylight components: (a) global horizontal (sky and sun), (b) diffuse horizontal (sky only), (c) direct normal (sun only).
(Larson and Shakespeare 1998)

Illuminance levels are calculated based on a ray-tracing method. Figure B.3 shows the way that the rays are produced from the point of interest. Those rays are generated and sent to the environment in a random way. According to the parts of the scene and the sky they hit, the horizontal illuminance is calculated (Larson and Shakespeare 1998). Several parameters have to be defined in order to create the desired ambient and produce the most preferable rays for the simulations (Table B.2).

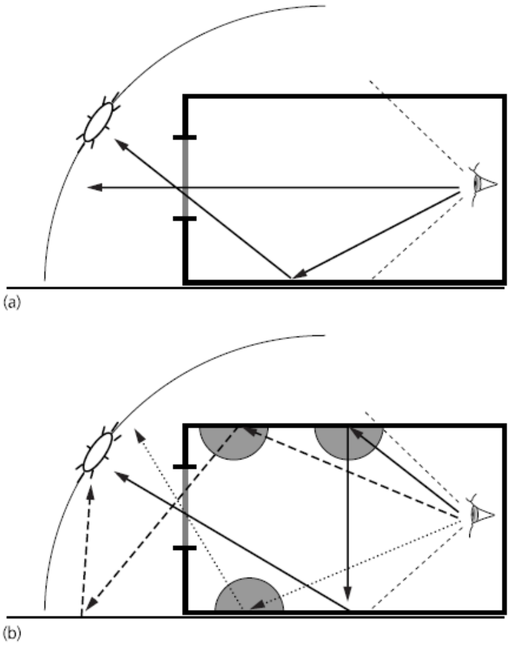

Figure B.3 Possible light transfers for ambient bounces equal to (a) 0, (b) multiple *(Larson and Shakespeare 1998)*

Table B.2 Basic parameters defined at the rtrace program

parameter	**function**
ad – ambient divisions	Captures the potential sources of indirect illumination
as – ambient super-samples	Same function as ad. Usually set to about one half or one quarter of this value
ar – ambient resolution	Determines the maximum density of ambient values used in interpolation
aa – ambient accuracy	Equals the error from indirect illuminance interpolation
ab – ambient bounces	Number of the bounces for the rays produced

Appendix C: The comparison of the illuminance levels corresponding to each sky sector

C.1 Initial values

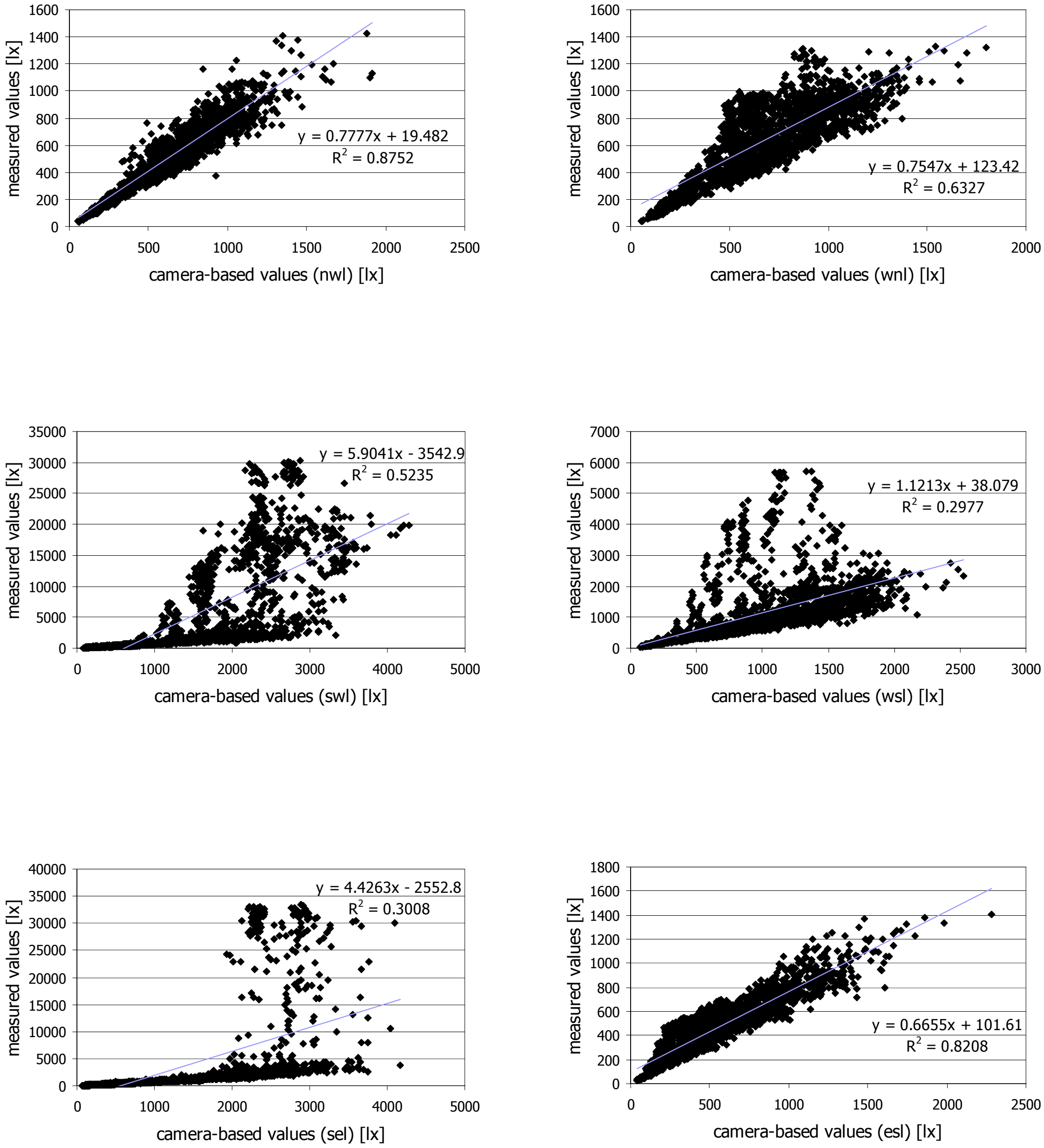

Figure C.1 Measured versus initial camera-based values

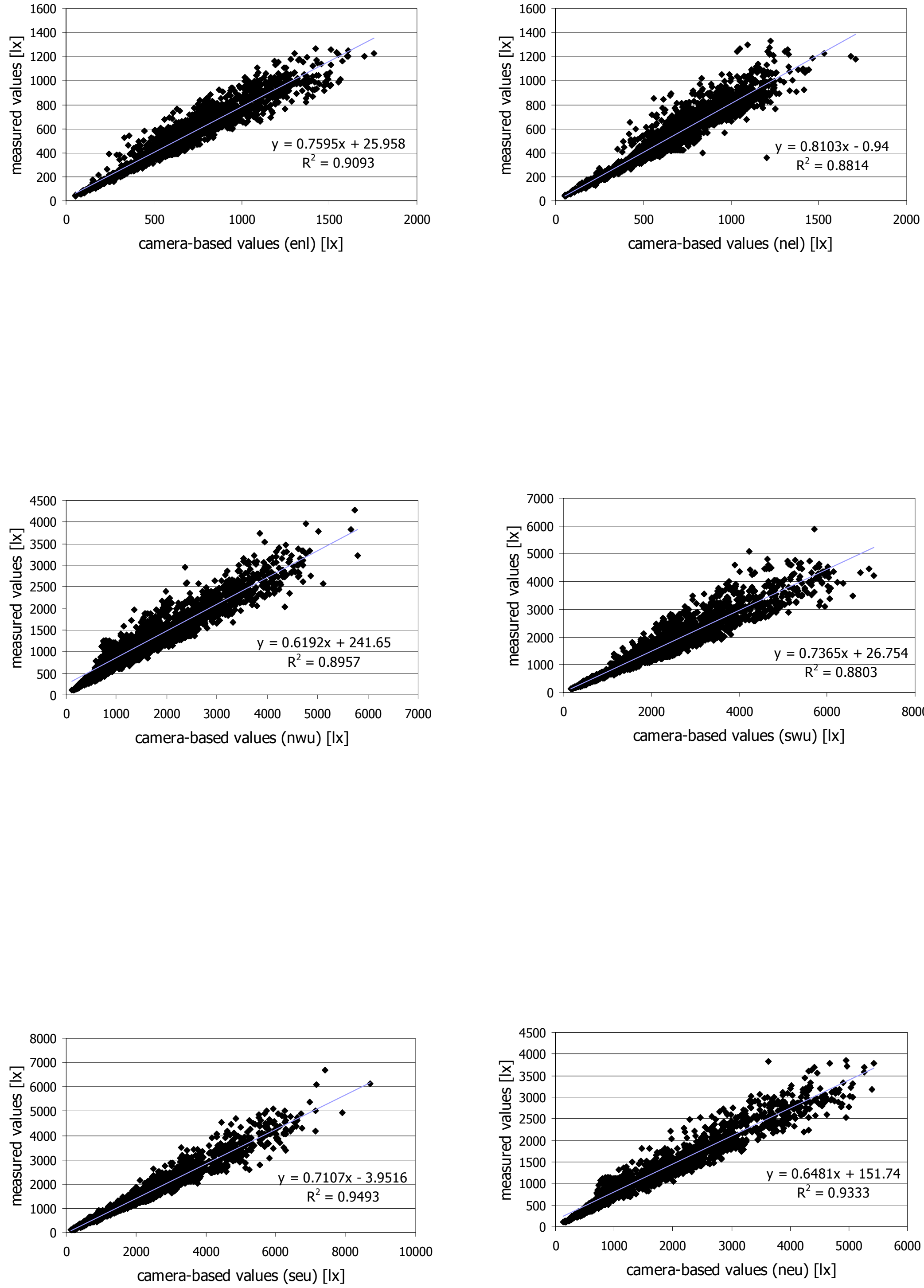

Figure C.2 Measured versus initial camera-based values

C2. Uniform correction (100_256)

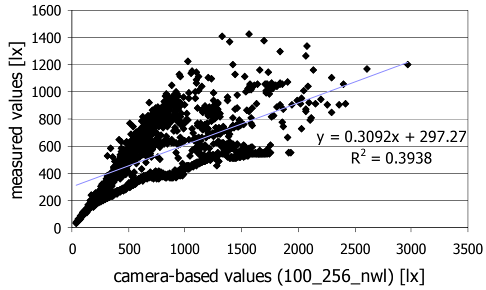

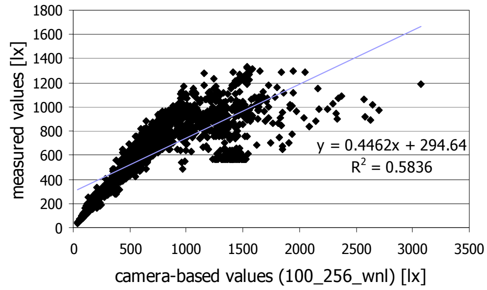

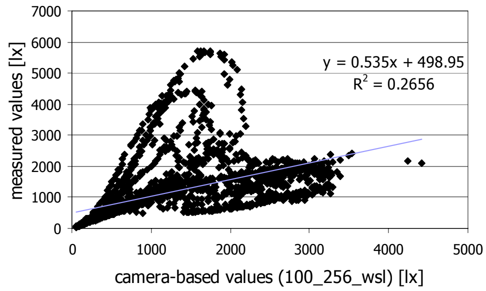

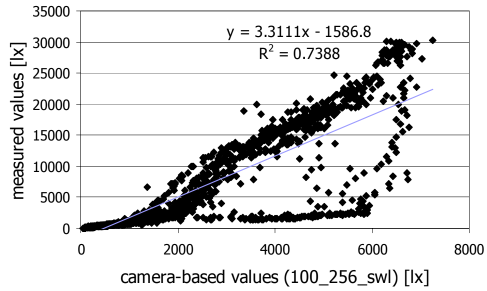

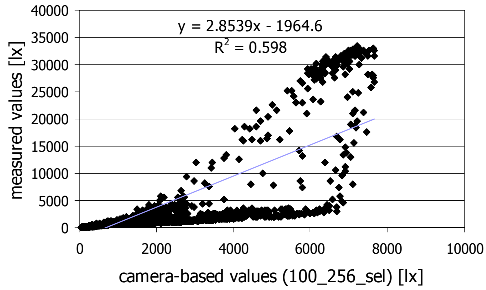

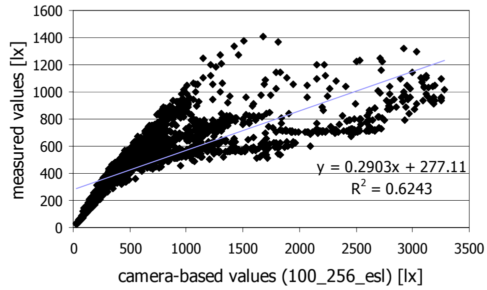

Figure C.3 Measured versus calibrated camera-based values (100_256)

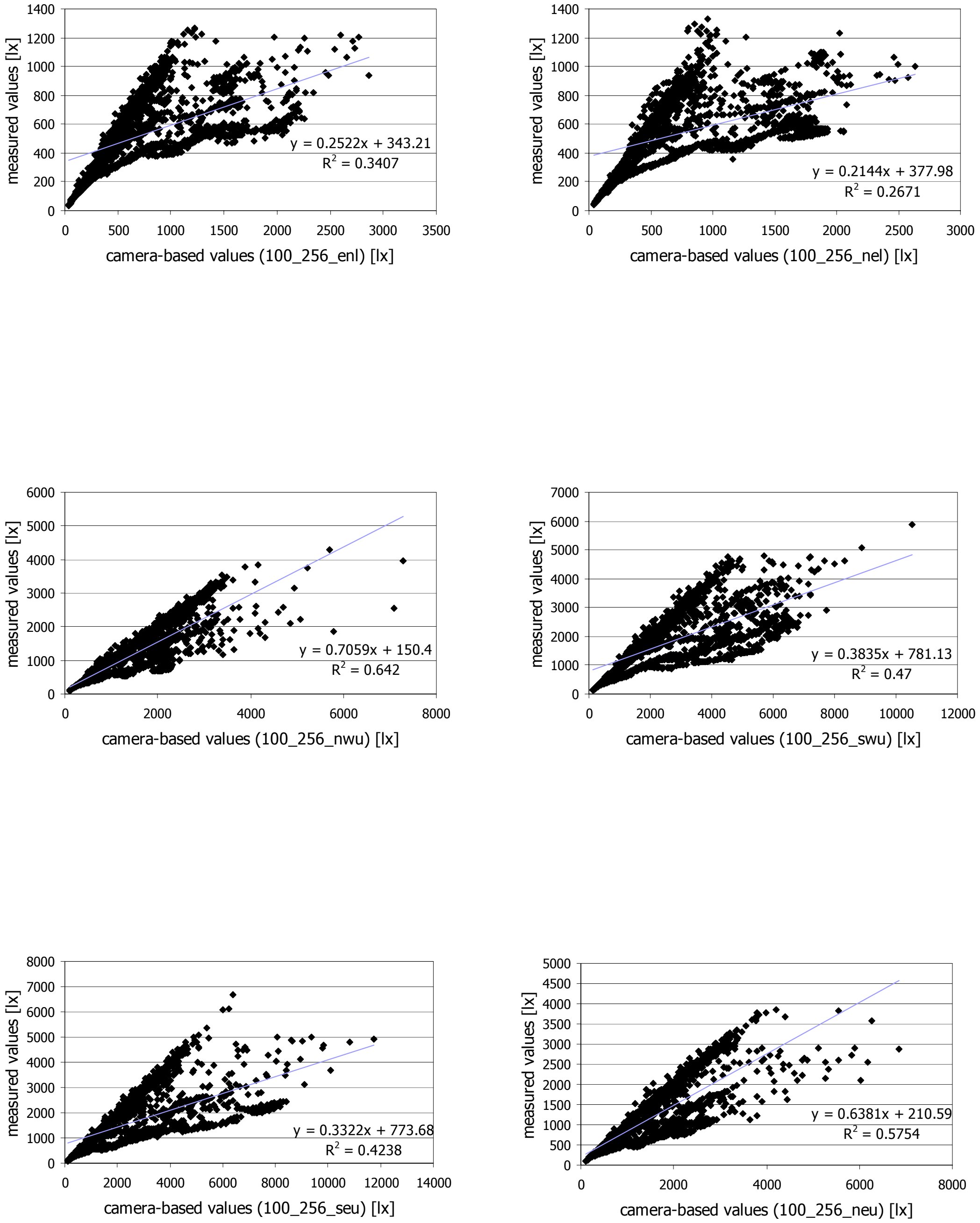

Figure C.4 Measured versus calibrated camera-based values (100_256)

C.3 60% - 40% correction (60_1)

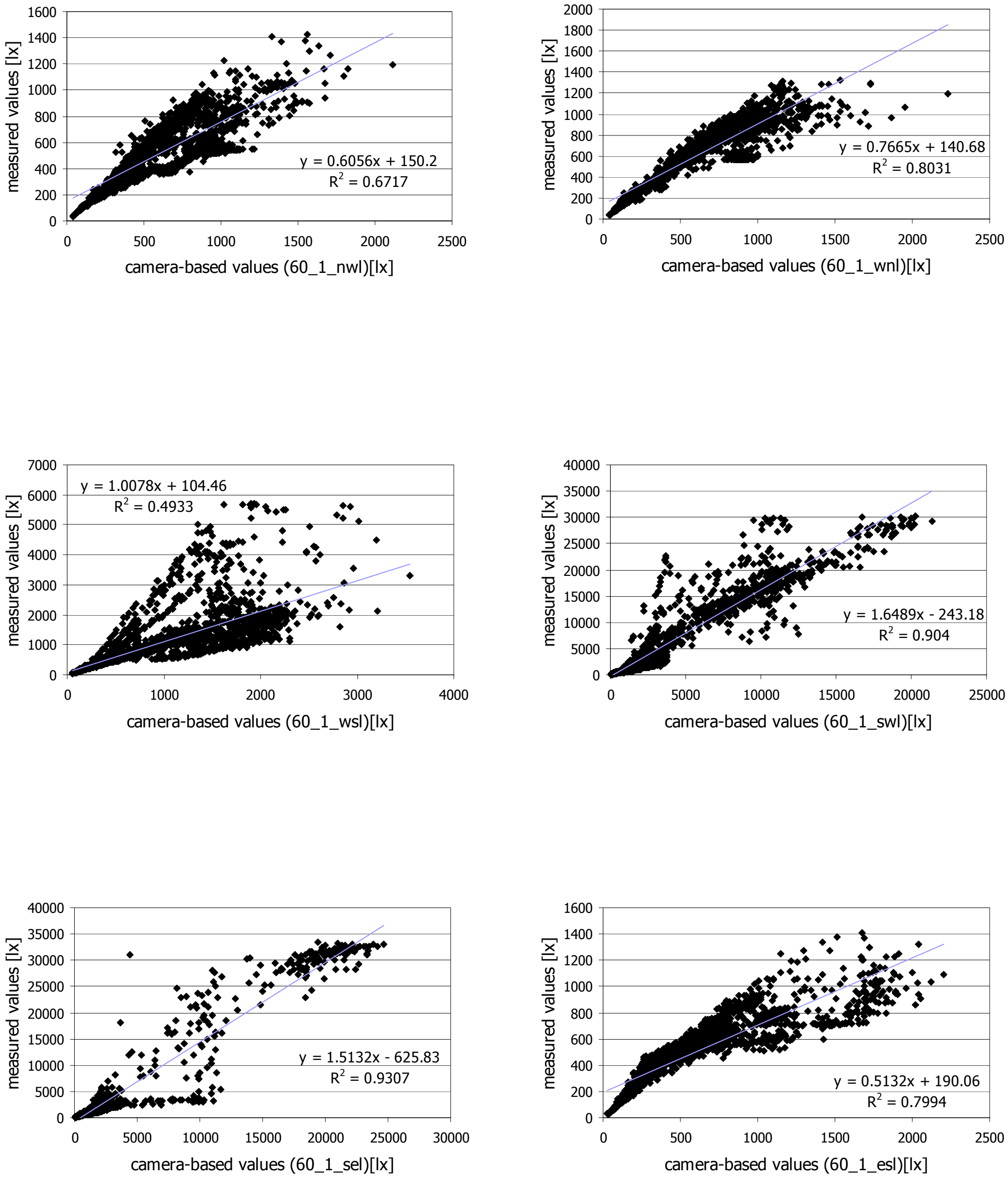

Figure C.5 Measured versus calibrated camera-based values (60_1)

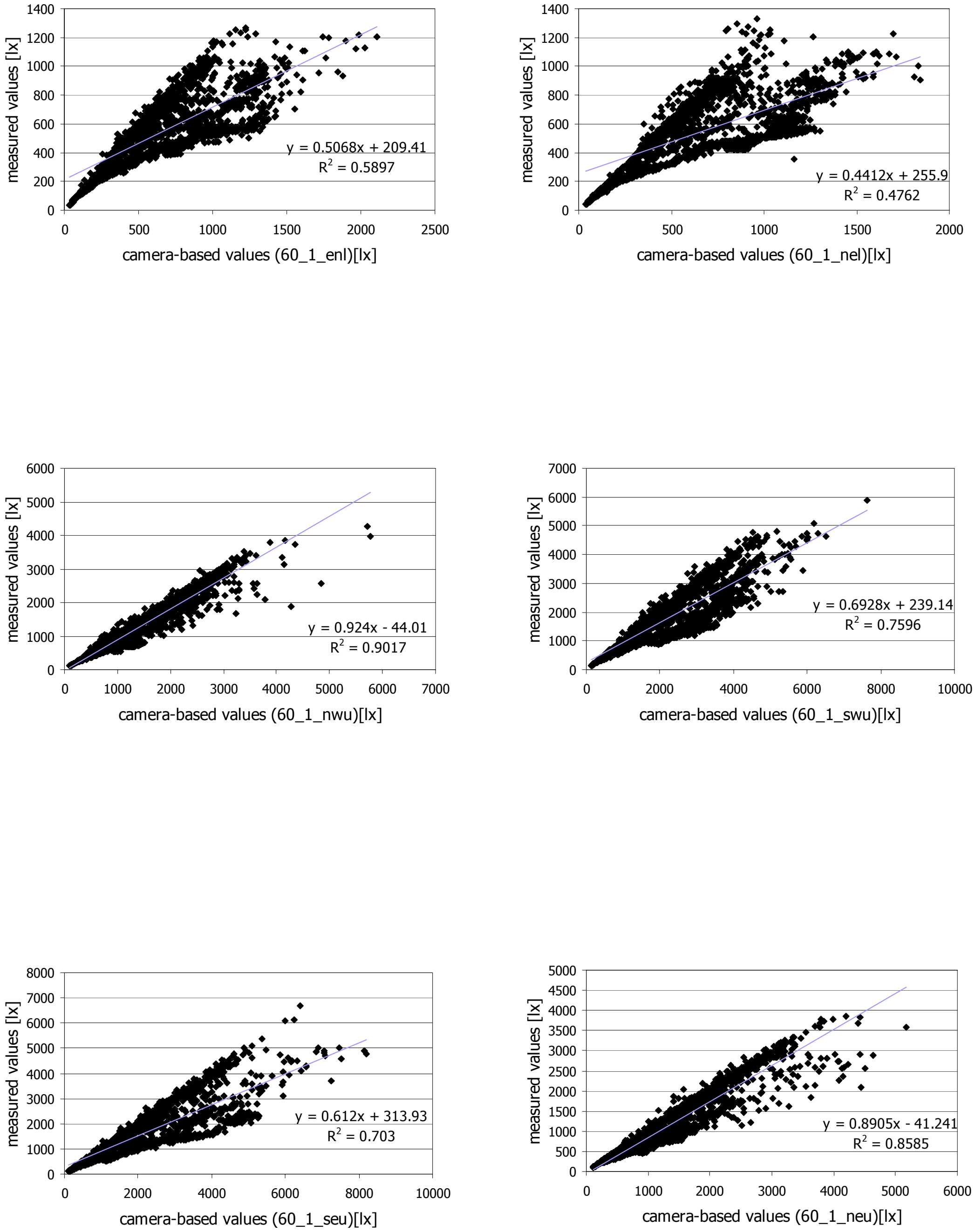

Figure C.6 Measured versus calibrated camera-based values (60_1)

C.4 100% to one sky patch correction (100_1)

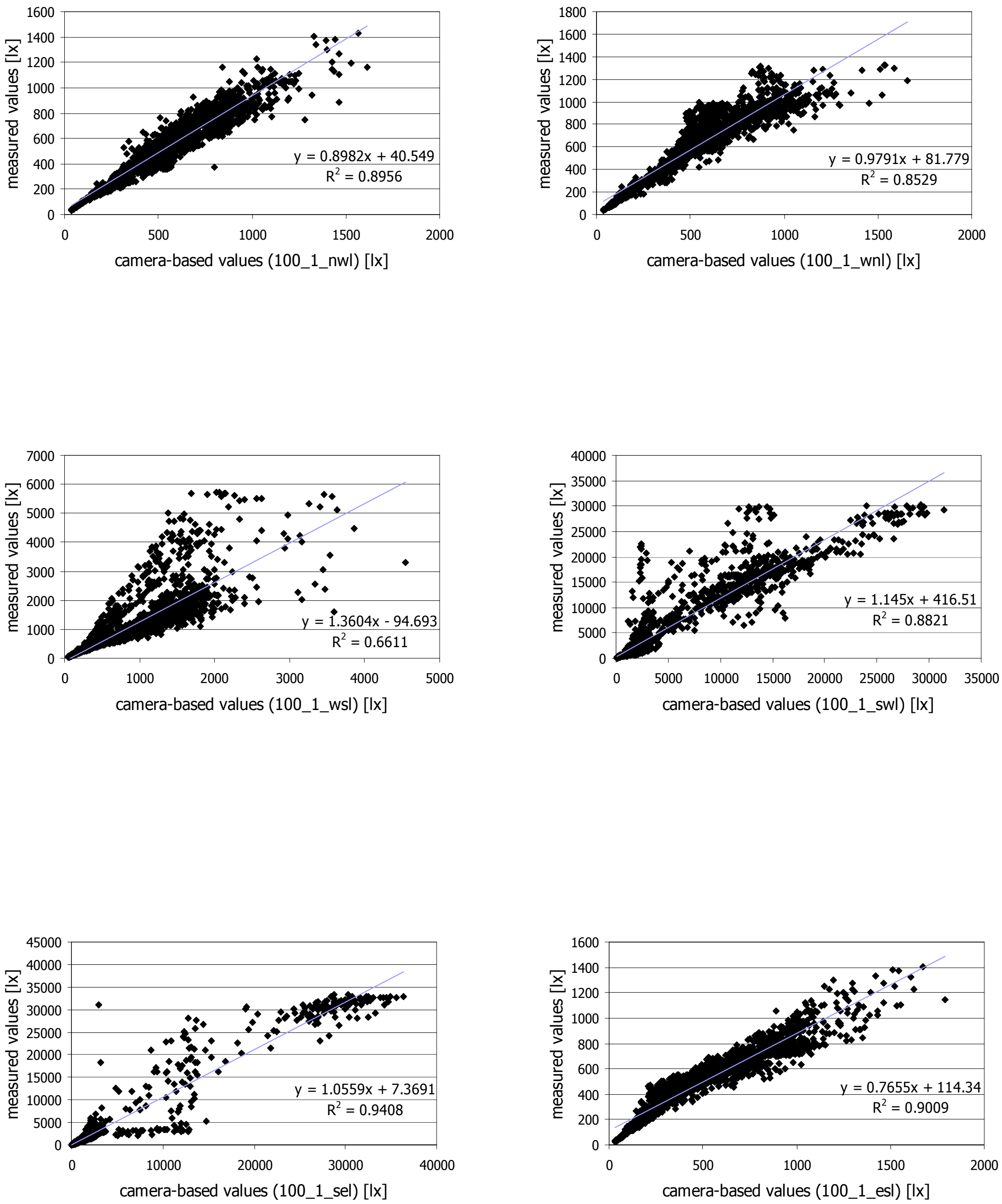

Figure C.7 Measured versus calibrated camera-based values (100_1)

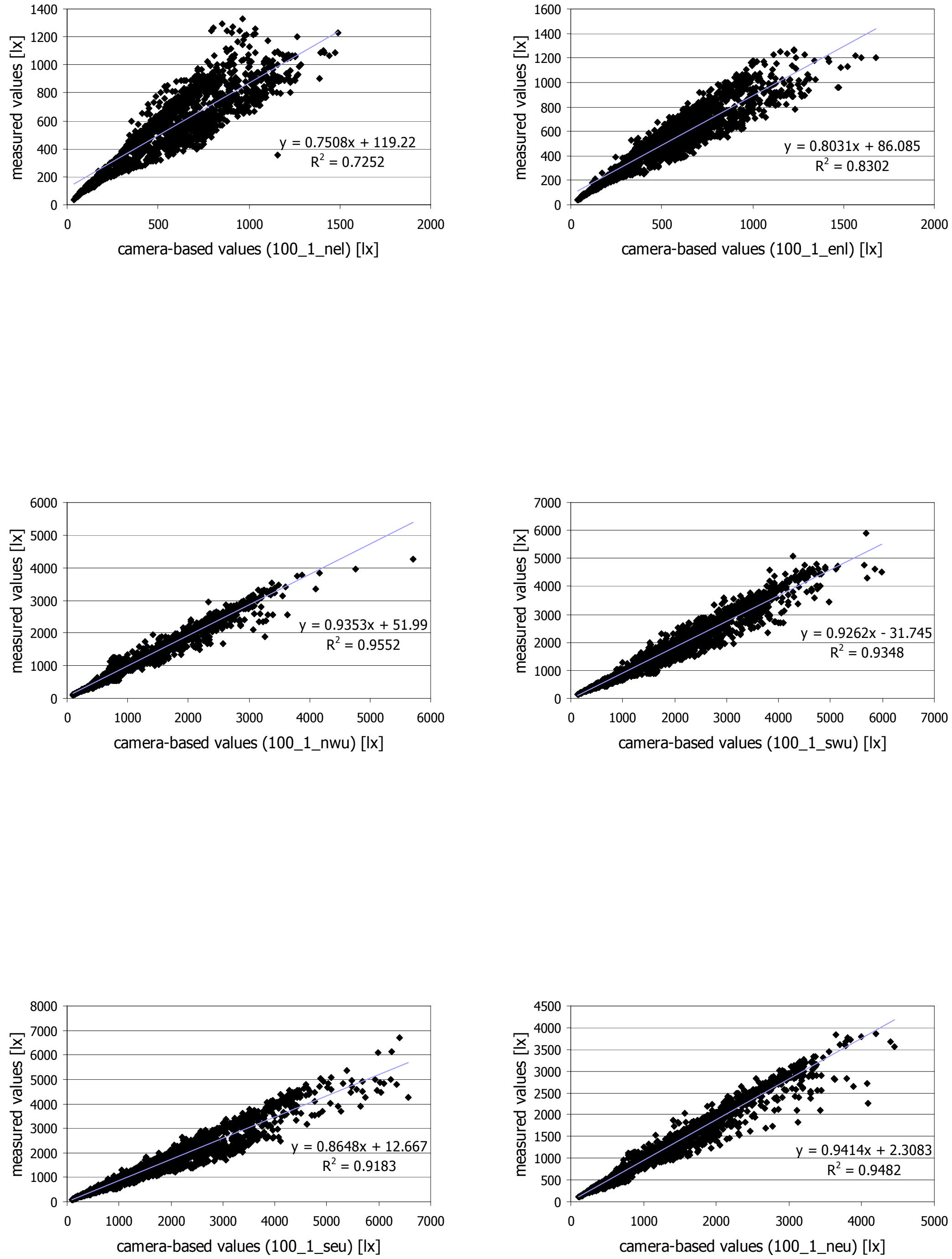

Figure C.8 Measured versus calibrated camera-based values (100_1)

C.5 100% to 5 sky patches correction (100_5)

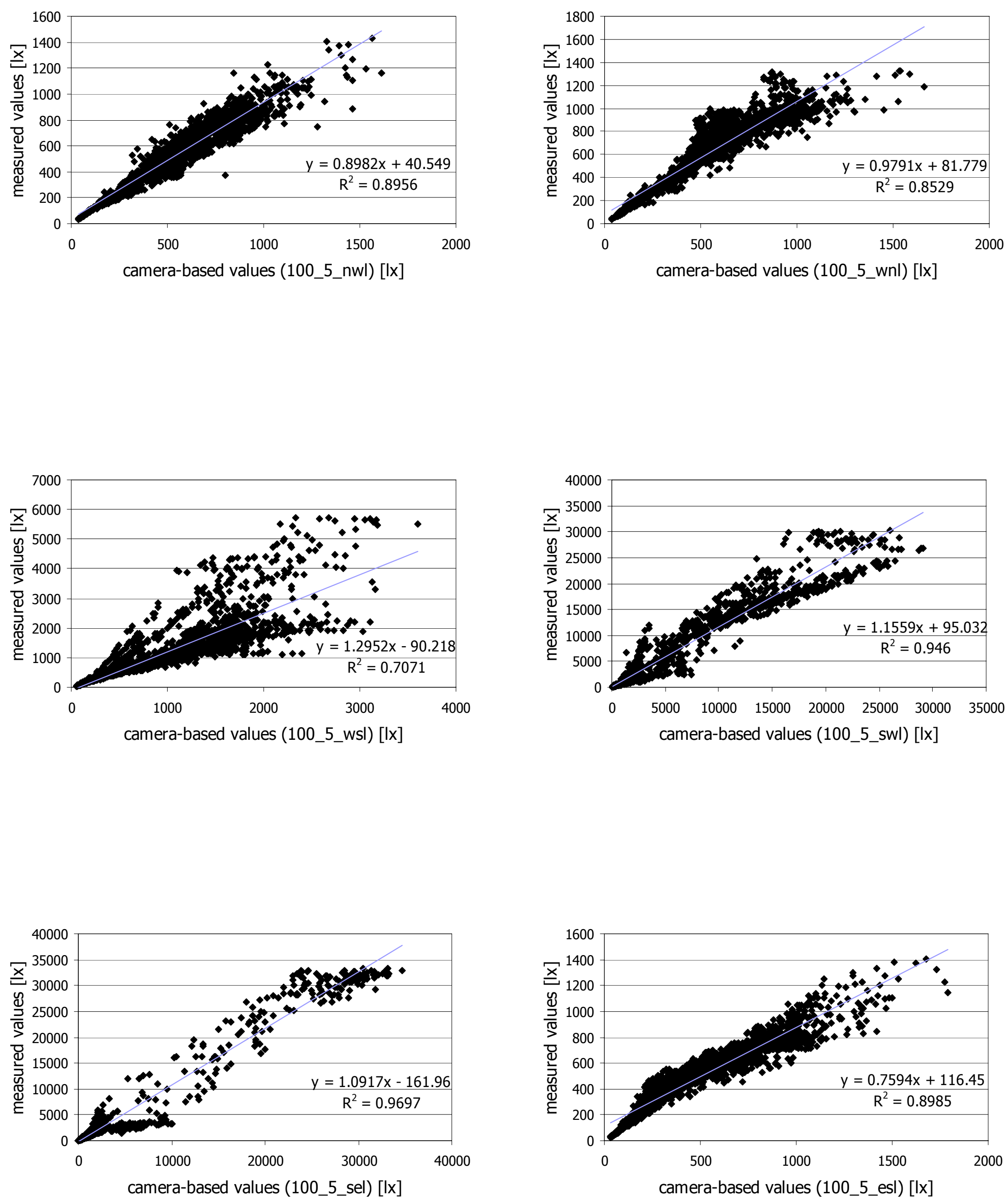

Figure C.9 Measured versus calibrated camera-based values (100_5)

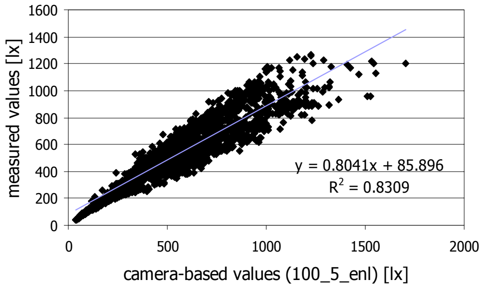

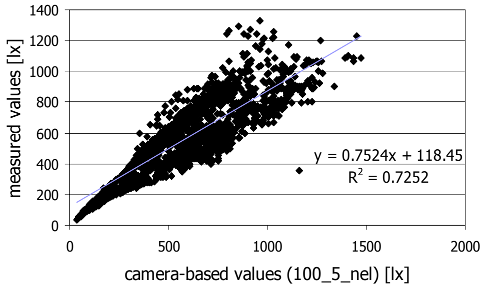

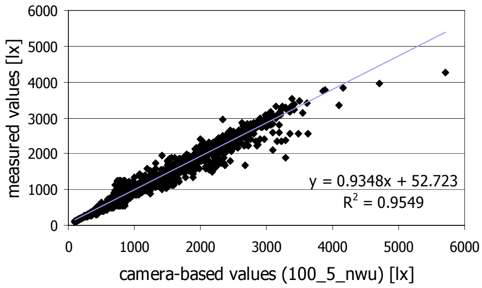

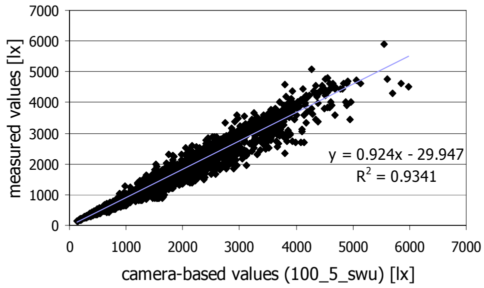

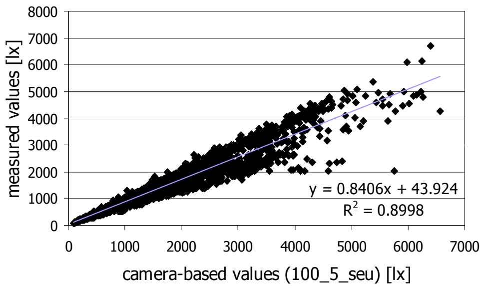

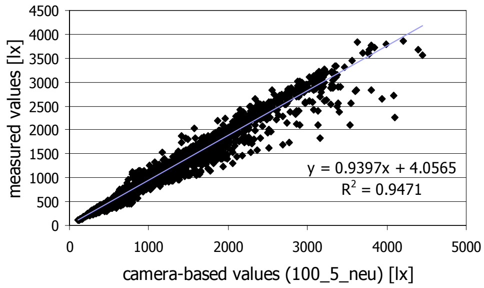

Figure C.10 Measured versus calibrated camera-based values (100_5)